Fundamental Aspects of the Self-Assembly Behavior and Electronic Properties of Corannulenes

---

Dissertation
zur
Erlangung der naturwissenschaftlichen Doktorwürde
(Dr. sc. nat.)

vorgelegt der
Mathematisch-naturwissenschaftlichen Fakultät
der
Universität Zürich

von

Tobias E. Bauert

von
Wetzikon ZH

Promotionskomitee

Prof. Dr. K.-H. Ernst (Vorsitz)
Prof. Dr. J. S. Siegel
Prof. Dr. K. Baldridge
Prof. Dr. S. Seeger

Zürich, 2011

Für meine Eltern.

Quidquid agis prudenter agas et respice finem.

Contents

Abstract

Surface modifications with functionalized molecules are a key feature for electronic applications with organic molecules. The self-assembly behavior of these molecules is of fundamental interest regarding the driving forces and processes involved.

Corannulene (COR) and pentamethyl substituated COR (Me_5COR) on Cu(111) were investigated with X-Ray photoelectron spectroscopy (XPS), ultraviolet photoelectron spectroscopy (UPS), low-energy electron diffraction (LEED), scanning tunneling microscopy (STM) and temperature programmed desorption (TPD).

Me_5COR exhibits a C_5 symmetry, which is incompatible with periodic tessellations of the plane. Combined LEED and STM studies show, that the fivefold symmetric molecules adapt two packing motifs known from macroscopic pentagons, while COR assembles in a hexagonal lattice at room temperature. Other phases of Me_5COR are identified, including a high temperature phase, which forms through surface chemistry.

The previously reported enantiotropic phase transition of COR is confirmed with LEED and influenced by filling free space around a high density phase, thus blocking a phase transition. Putting chiral molecules on top of the room temperature phase leads to suppression of mirror domains of the next phase during phase transition. Self-assembly of D- and L- tartaric acid (TA) as well as the racemic mixture were investigated with LEED.

UPS measurements on COR and Me_5COR on Cu(111) reveal the electronic structure of the adsorbates, as well as confirmation of the COR HOMO participating in surface binding. From work function change measurements the interfacial dipole moment of COR /Cu(111) and Me_5COR/Cu(111) is determined and found to be unusually high at over 8 debye. The maximum work function change is in the order of $-1.5\,\mathrm{eV}$.

Finally the effect of Cs doping on the two molecules was investigated with UPS. Both molecules show occupation of the LUMO and thick films of Cs/COR and Cs/Me_5COR proved to be very stable far beyond room temperature. XPS studies of Cs/COR indicate coordination of four Cs atoms per COR molecule.

Zusammenfassung

Modifikation von Oberflächen mit Hilfe funktionalisierter Moleküle ist ein zentraler Punkt für elektronische Anwendungen mit organischen Molekülen. Das Verhalten bei Selbstorganisationsprozessen dieser Moleküle ist von grundlegendem Interesse hinsichtlich der treibenden Kräfte und Prozesse, die involviert sind. Corannulene (COR) und Pentamethyl-Corannulene (Me_5COR) auf einer Cu(111) Oberfläche sind mit den folgenden Methoden untersucht worden: Röntgen-Photoelektronen Spektroskopie (XPS), Ultraviolett Photoelectrons Spektroskopie (UPS), Beugung langsamer Elektronen (LEED), Rastertunnelmikroskopie (STM) und Temperatur-Programmierte Desorption (TPD).

Me_5COR hat eine C_5 Symmetrie, welche mit flächenfüllenden Anordnungen in zwei Dimensionen inkompatibel ist. Kombinierte LEED und STM Studien zeigen, dass diese fünffach symmetrischen Moleküle zwei Packungsmotive übernehmen, die durch Experimente mit makroskopischen, harten Fünfecken bekannt sind. COR im Gegensatz organisiert sich in einer hexagonalen Struktur bei Raumtemperatur. Weitere Phasen von Me_5COR werden identifiziert, darunter eine Hochtemperatur-Phase, die durch Oberflächenchemie entsteht.

Der vorgängig publizierte enantiotrope Phasenübergang von COR wird mit LEED Messungen bestätigt und mittels Auffüllen von frei werdenden Flächen um die dichte Phase beeinflusst. Dies führt zur Blockierung des Phasenübergangs. Das Abscheiden von chiralen Molekülen auf die Raumtemperatur-Phase führt zur Unterdrückung von Spiegeldomänen der nächsten Phase beim Phasenübergang. Die Selbstorganisation von D- und L-Weinsäure und des racemischen Gemisches wird mit LEED untersucht.

UPS Messungen von COR und Me_5COR auf Cu(111) zeigen die elektronische Struktur der Adsorbate auf und bestätigen die Partizipierung des COR HOMO bei der Bindung zum Substrat. Mittels Austrittsarbeitsmessungen wird das System-Dipolmoment von COR/Cu(111) und Me_5COR/Cu(111) bestimmt. Es zeigt sich, dass ungewöhnlich hohe Werte über 8 debye erreicht werden. Der Maximalwert der Austrittsarbeitsänderung ist in der Grössenordnung von $-1.5\,\text{eV}$.

Der Effekt von Cs Dotierung auf die beiden Moleküle wird mittels UPS analysiert. Bei beiden Molekülen wird festgestellt, dass der LUMO besetzt wird und dicke Filme von Cs/COR und Cs/Me_5COR sind sehr stabil bis zu Temperaturen weit über Raumtemperatur. XPS Untersuchungen von Cs/COR deuten darauf hin, dass vier Cs Atome pro COR Molekül koordinieren.

Chapter 1

Introduction

Surface modification with functionalized organic molecules has become of special interest in surface science in the last twenty years. Organic molecules have changed their applicability from pure structural applications in form of polymers or "plastics" and surface modifications in terms of wettability, reactivity and general chemical and physical surface activity for alternative electrically conductive materials. Since the discovery of electrical conductivity in organic molecules by Shirakawa, Heeger and MacDiarmid in 1977 [1] the field of conductive molecules has experienced a boom [2]. Apart from conductivity, organic molecules that are intrinsically insulating or semi-conducting and reach metallic conductivity upon doping, received special attention [3].
Applications that are already established are mainly based on the simple conductivity of polymers for instance as antistatic coatings. In recent years the semiconducting behavior became of much greater interest and organic molecules are now found in mass-produced electronics like organic light emitting diodes (OLED) [4–7]. Other promising fields of application – although by far not as developed as OLED's – are organic field emitters [8] and organic solar cells [9]. Fullerenes are by now the most promising candidates that are intensely studied to provide an organic acceptor material for mass production of organic solar cells.

Although organic molecules have found their way into electronic applications, there is a need for improvement in charge carrier mobility and durability, and a better understanding of the intermolecular interaction as well as the interaction with the electrode surface. In particular, processes at the organic-inorganic interface, like charge-carrier injection, are of crucial importance.

Due to the complexity of these material systems, physical vapor deposition of organic molecules on metal single crystals in ultra-high vacuum provides an ideal model system in order to study the growth and structures of molecular thin films regarding their two-dimensional ordering, the chemical and physical bondings involved and the electronic properties of the assembled system. Together with powerful theoretical modeling, molecular surface science is able to answer more fundamental questions.

1.1 Corannulene

1.1.1 Basic Properties

Corannulene was chosen for investigation due to three particularly interesting properties.

- Its fivefold symmetry is of special interest due to its incompatibility with tessellations of the plane and crystal growth [10].
- Its bowl-shape besides its aromaticity is a rare combination making the molecule an intriguing system both due to its intrinsic geometry and the electronic properties.
- Corannulene is the smallest bowl-shaped C_{60}-fullerene fragment and is expected (as shown in here) to exhibit similar properties in self-assembly behavior or as an electron acceptor. This close relation to the buckyball, paired with a much better solubility in most common solvents, is the reason for the general interest in the performance of corannulene.

Corannulene was first synthesized in 1966 by Wayne Barth and Richard Lawton as Dibenzo[ghi, mno]fluoranthene [11]. They proposed the name "corannulene" based on the fact, that the molecule can be seen as a "core" within an "annulene". They suggested that a polar resonance form is likely, highlighting the core-annulene idea. When the molecule is polarized (see Figure 1.1) it becomes clear, that it can be seen as consisting of two charged concentric, conjugated systems.

A note on the aromaticity of corannulene: Barth and Lawton attested the molecule aromatic character based on their theory of two concentric conjugated rings. In 1967 G. J. Gleicher did self-consistent field molecular orbital calculations on the corannulene system and not only correctly predicted the non-planar form,

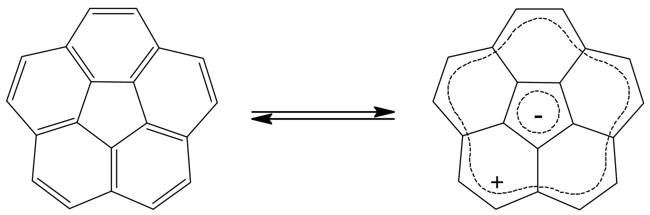

Fig. 1.1 Corannulene (left) and its polarized form (right). The electrons participating in the two conjugated subsystems in the polarized form account for $5 + 1 = 6\,\mathrm{e}^-$ for the inner ring and $15 - 1 = 14\,\mathrm{e}^-$ for the outer ring, both complying with Hückel's rule [11].

but also found that ”in summary, corannulene appears to have sufficient resonance energy to exhibit aromatic character” [12]. Hanson and Nordman confirmed Gleicher's calculations in 1976 [13].

In the end Barth and Lawton had it right from the beginning, corannulene is fully aromatic. Hückel's rule does neither apply for non-planar molecules, nor for certain polycyclic molecules. In theory the $4\,n+2$ rule can only be justified for monocyclic systems [14]. Hückel's rule can neither explain aromaticity in coronene nor in some fullerenes [15]. The aromaticity of corannulene is based on two aromats that share the same central symmetry point.

The distorted geometry of corannulene was of special interest in the early stage of its research. Barth and Lawton already predicted [11], that the strain in the C-C bondings of the molecule is expected to distort the molecule from the planar form into a bowl shape. J. C. Hanson and C. E. Nordman published the crystal and molecular structure of corannulene in 1976, presenting data for all bond angles and the bowl depth of 0.87 Å [13].

The early discovery of this hydrocarbon molecule is quite astonishing in hindsight, if one considers that the discovery of C_{60} in 1985 by the group of R. E. Smalley [16] gave rise to an enormous boost in research on pure carbon based systems. Concerning the symmetry and conformation, corannulene may be seen as a fragment of the C_{60} molecule: When the fullerene is mentally cut in thirds, the three parts consist of two dehydrogenated corannulenes (with fairly increased bowl depths) and a carbon belt.

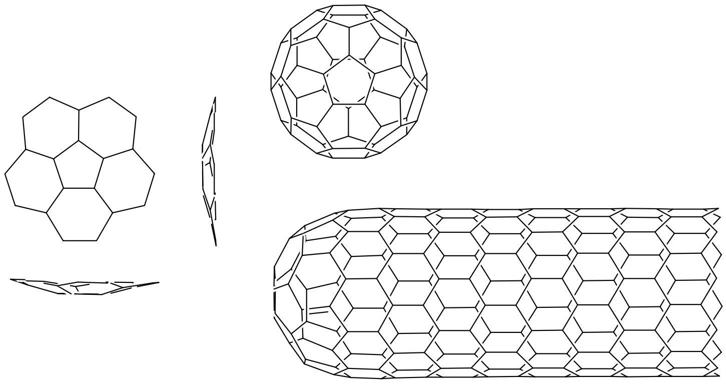

Fig. 1.2 Schematic drawings of corannulene, the buckminster fullerene and a single-walled carbon nanotube (SWNT). It should be noted, that the corannulene molecule is not related to SWNTs, but there exist similarities in the symmetry and curvature of the end-caps of certain nanotubes.

Corannulene will be compared to C_{60} concerning the self-assembly behavior and the electronic adsorbate structure in this thesis. Therefore a very short overview on the fullerene properties will be given here.
C_{60} self-assembles into a close packed (4x4) adlayer structure on Cu(111) [17]. It was found that the fullerene binds to a threefold hollow site on the substrate in presence of a significant charge transfer [18]. It was also confirmed, that the C_{60} chemisorbs with a six-membered ring parallel to the Cu(111) surface [19] as was found for benzene on Cu(111) [20].

In the C_{60}/Cu(111) system two Fermi level near states at $-0.15\,\mathrm{eV}$ and $-0.9\,\mathrm{eV}$ are of great importance due to their participation in hybridization of molecular orbitals and electronic states of the metal substrate. This hybridization due to charge transfer is a possible explanation for self-doping effects that are proposed for molecular systems on metal substrates [22, 23]. These two Fermi level near states do not show up in corannulene adlayers, as will be shown later on, indicating, that no charge transfer occurs in the COR/Cu(111) system.
The partial filling of the LUMO of an individual molecule is also thought to have the effect of overlapping with the same parts of neighboring molecules. The overlap forms bands, which disperse across the Fermi level. This introduces metallic behavior to the two-dimensional molecular film, replacing van der Walls forces as

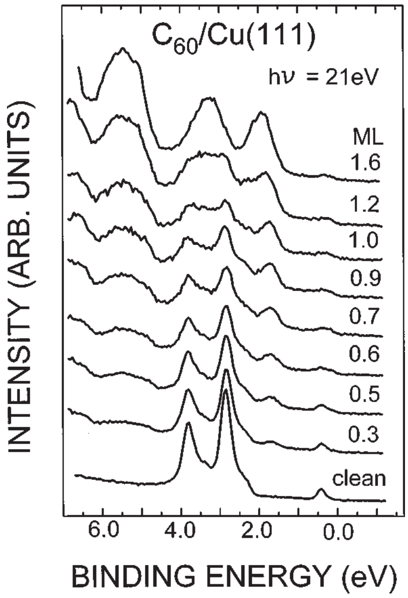

Fig. 1.3 Coverage dependence of normal-emission photoelectron spectra of C_{60} on Cu(111) deposited at room temperature. The photon energy was 21 eV, and the incident angle was 45 °. These spectra are normalized to the intensity above the Fermi energy. Reprinted with permission from [21]. Copyright (1997) by the American Physical Society.

the dominant intermolecular interaction [21].

Figure 1.3 shows the coverage dependant molecular orbitals as found by UPS measurement in [21]. The gradual disappearance of the Cu *d* peaks is accompanied by the growth of the HOMO between the Cu *d* band and the Fermi level. The HOMO shifts to higher binding energy upon growth of the second layer. The Cu surface state just below the Fermi level diminishes with growth of the monolayer. The growth of the interface states with hybrid character between the HOMO and the Fermi level can not be seen at this resolution. The self-doping of C_{60} on metal surfaces is still under thorough investigation in various groups [24].
It was found that the deposition of C_{60} on Cu(111) leads to a drop in work function of 0.08 eV for a full monolayer, a rather insignificant change, considering an estimated charge transfer of 1.5 to 2 e^- per molecule from the substrate.
C_{60} exhibits also superconducting behavior [25–29], which is of no importance in this thesis.

1.1.2 Chemical and Physical Properties

The chemical formula of corannulene is $C_{20}H_{10}$ with a molecular mass of 250.29 g/mol. The many steps of the original synthesis [11] started from bromination of methyl-4,5-methylenephenanthrene-3-carboxylate to a bromo ester, followed by different steps forming tetraester and diacid diester and cyclization to a keto acid diester. More steps over more ester lead to final ring closing and several reductive steps freed the corannulene core of its substituents.

The first synthesis with medium yield was flash vacuum pyrolysis by Scott and coworkers [30–32]. Yield was still very low at 20 %. The small scale approaches to synthesize corannulene in solution were first published by Peter Rabideaus group in 1991 and 1992 [33, 34]. They used McMurry coupling as an alternative to vacuum pyrolysis with low-valent titanium or vanadium resulting in over 70% yield. The following scheme in Figure 1.4 gives an overview over different approaches to the small scale synthesis, as it was used in the beginning of this project.

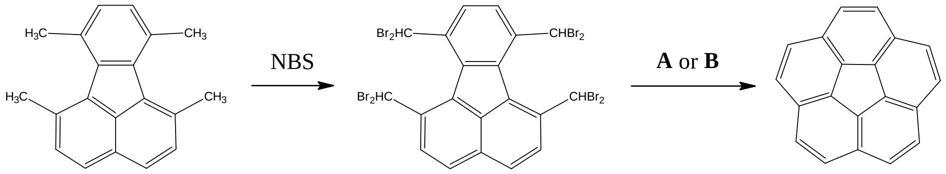

route **A**: $TiCl_4$, Zn/Cu, DME
or VCl_4, $LiAlH_4$, DME
route **B**: 1) NaOH, dioxane, H_20
2) Zn, NaI, EtOH or DMF

Fig. 1.4 Non-pyrolytic synthesis of corannulene as described in [33, 34]. Tetramethylfluoranthene is brominated with N-Bromosuccinimide under forcing condition to produce octabromide. In route A ring closure occurs with reducing agents in anhydrous condition. Route B uses sodium hydroxide to produce tetrabromocorannulene, which reacts under treatment with zinc and potassium iodide to COR.

The synthesis of corannulene was subject to intensive research over the last decade and a large scale synthesis has been established and is on the verge of being published by Siegels group (publication in progress [35]). The detailed synthesis of corannulene with all its difficulties is beyond the scope of this thesis. The reader is referred to the literature [11, 30–34, 36], which was reviewed by Yao-Ting Wu and Jay Siegel [37].

Table 1.1 shows predicted physical properties of corannulene.

Physical property	value
refraction index	2.154
molar volume	170.604 cm^3
polarizability	$37.073 \cdot 10^{-24}\mathrm{cm}^3$
density	1.467 $\mathrm{g/cm}^3$
vaporization enthalpy	66.791 kJ/mol
melting point	432.4 K
boiling point	711.15 K at 760 mmHg
Water Solubility at 25 °C	0.05271 mg/l

Table 1.1 Selected predicted physical properties of corannulene. All values were calculated with ACDLabs Physicochemical Prediction, except water solubility (EPISuite). Source: ChemSpider.com.

1.1.3 Symmetry Aspects

There are only 17 irreducible space groups that can form tessellations of the plane [10], none of which shows five- or sevenfold symmetry. Fivefold symmetry is incompatible with plane filling packing motifs without overlaps or gaps between the tiles. Geometers like Johannes Kepler, Albrecht Dürer and Sir Roger Penrose proposed clever solutions for the tiling problem with five-fold symmetric objects [38], but all resulted in inhomogeneous tile types, aperiodicity, or lower lattice symmetry [39]. The Aa tiling of Kepler and the famous Penrose tiling are very well known and appear every so often in art, architecture and design. In these tessellations as well, the pentagons can not cover the surface without overlaps or gaps, but additional tiles are introduced to fill the regularly formed gas. This problem is not only of interest for mathematical and geometric reasons, but has an interested group of followers from architecture and the packing and shipping industry to surface scientists, which are bound to the same 17 two-dimensional space groups [40, 41]. Tessellations with organic molecules are of special interest due to the fact, that close-covered ultrathin films are crucial for electronic properties, especially in molecular electronics and photovoltaics.

To address the fivefold packing problem macroscopic experiments were conducted by different techniques: densification of hard pentagons on shaking [42] or blowing tables [43] and computer assisted simluations [44]. Independently of each other these techniques came to the same packing motifs for pentagon tessellations. Schilling and coworkers investigated the packing problem with Monte-Carlo simulations [44]. Under the central question of how the phase transition from liquid to solid occurs, when the geometry of the particles conflicts with the symmetry of the crystal, they studied the phase behavior of hard pentagons.
Upon increasing the density (or pressure) of the tiles, the isotropic quasi-liquid phase transformed to quasi-hexagonal phase with random azimuthal orientation of the pentagons, named the rotator phase. This phase (Figure 1.5) corresponds directly to the low density phase found on the air table by Duparcmeur et al.

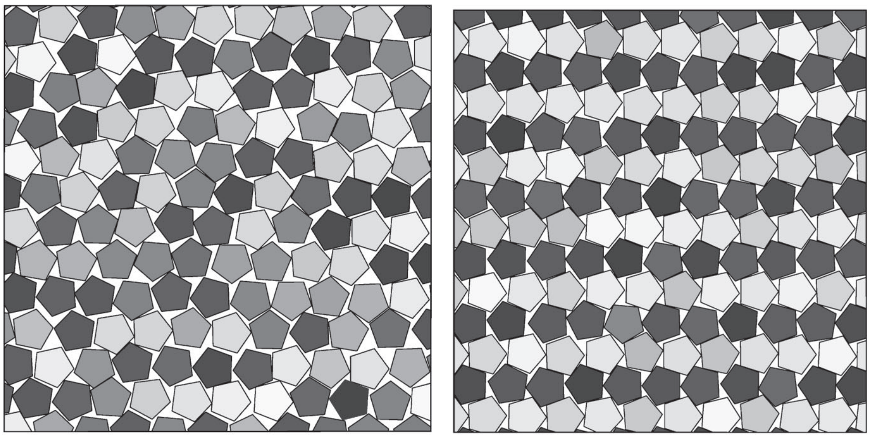

Fig. 1.5 Pentagon ordering regimes. The rotator phase (left) corresponds to less density and more disorder, whereas the striped phase (right) corresponds to higher packing density and increased ordering. Reprinted with permission from [44]. Copyright (2005) by the American Physical Society.

When the pressure is further increased the rotator phase undergoes a weak first order transition to the striped phase, composed of alternating rows of oppositely oriented tiles, Figure 1.5 right. Whereas the rotator phase shows packing densities between 0.7 and 0.82, the striped phase reaches 0.88[a]. A very similar striped phase was found for rigid heptagons as well, under the same conditions, showing basically the same properties.

[a] The packing density is calculated by dividing the area covered by the tiles by the total area of the substrate.

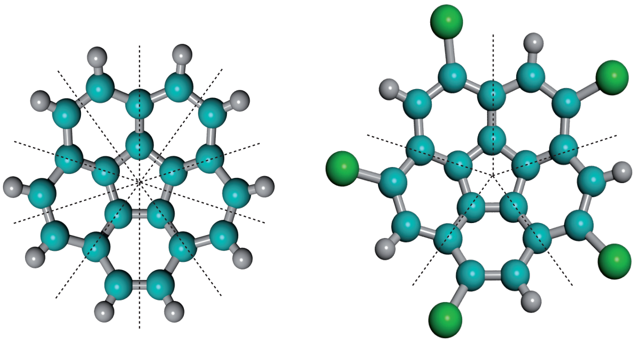

C_{5v} C_5

Fig. 1.6 The symmetry elements of corannulene and pentachloro-corannulene. Corannulene on the left shows a C_{5v} symmetry. The molecule is achiral. Pentachloro-corannulene shows only a C_5 symmetry. Due to the substitution of every other hydrogen the mirror symmetry is destroyed and the molecule becomes chiral.

Figure 1.6 shows the C_{5v} symmetry of the corannulene molecule with its five-fold rotational symmetry and the mirror plane. All ten hydrogens on the rim are identical. Penta-substituated corannulenes may have every other hydrogen substituted with a functional group. This makes the two groups on every sixfold ring different from each other and the mirror symmetry is lost. Therefore penta-substituated corannulene derivatives exhibit not only a reduced symmetry (C_5), but the molecules are also inherently chiral. In gas phase at sufficient temperature this is of no importance, due to the high frequency bowl inversion [45], which transforms one enantiomer into the other. Adsorbed on a substrate, the bowl inversion is inhibited and two enantiomers should be found. It is, however, interesting to see, whether the small difference in shape of the two enantiomers is expressed at the level of self-assembled 2D crystals.

1.1.4 Previous Work on Corannulene

M. Parschau and coworkers investigated the self-assembly of corannulene on Cu(110) with STM [46]. They discovered spontaneous symmetry breaking by formation of enantiomorphous lattice structures. Two mirror domains of quasi-hexagonal structures were found with the transformation matrices $\begin{pmatrix} 3 & 2 \\ -4 & 1 \end{pmatrix}$ and $\begin{pmatrix} 4 & 1 \\ -3 & 2 \end{pmatrix}$[b], see Figure

---

[b] The master matrix being $\begin{pmatrix} 3 & -2 \\ 1 & 3 \end{pmatrix}$, see appendix for matrix notation.

1.7. High resolution STM images clearly showed a distinct "doughnut" shape of the STM representation of the molecules. By simulating STM images (Figure 1.7 right) it was confirmed that this experimental STM appearance stands for a "bowl-opening-pointing-up" geometry. However, the STM image also shows a small asymmetry. Synchrotron-based X-Ray Photoelectron Diffraction (XPD) showed a tilt angle of the molecule of 6 °.

This corannulene structure was investigated towards its suitability as a template for hosting C_{60} [47]. It was shown before in gas phase and solution, that corannulene and C_{60} are suited for complexation [48, 49].

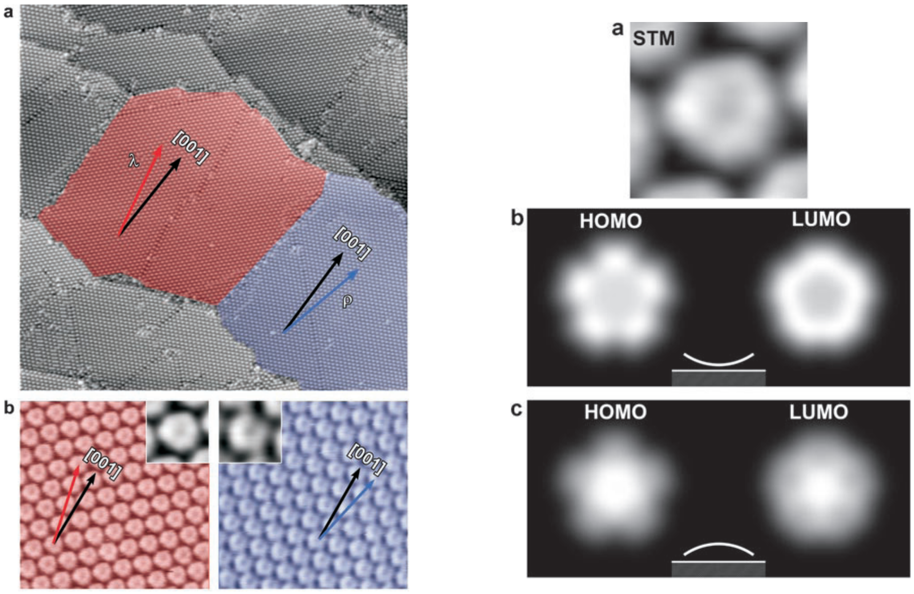

Fig. 1.7 Left: STM images of corannulene on Cu(110) showing the two mirror domains (b). Right: Comparison of a high resolution STM image of a single molecule (a) with simulated STM images by Extended Hückel Theory calculations of corannulene with the bowl-opening facing the substrate (c) and away from it (b). Reprinted from [46], copyright Wiley-VCH Verlag GmbH & Co. KGaA.

Corannulene on Cu(111) is a unique model system for the studies of phase transitions, since it features an enantiotropic phase transition in the 2D adlayer structures. Upon deposition at room temperature the molecules self-assemble in a (4x4) adlayer (Figure 1.8, like C_{60}). High resolution STM measurements in combination with DFT calculations showed that the molecule is also situated over a threefold hollow site and is aligned with a six-membered ring parallel to the surface. For the bowl-shaped corannulene, this means a tilting of the bowl [50, 51] was observed in high resolution STM (Figure 1.8).

Upon cooling the sample under 250 K a phase transition occurs involving a 14 % density increase, see Figure 1.8. The new adlayer structure that forms is stable in the temperature range between 250 and 200 K and shows a large hysteresis in the temperature of the formation. The structure is described with the adlayer matrix $\left(\begin{smallmatrix} 4 & 0 \\ 3 & 7 \end{smallmatrix}\right)$.
Further cooling of the sample to liquid nitrogen temperature (77 K) induces the second phase transition from phase II to phase III. This transition is not accompanied by a density change. Phase III displays a stripe like appearance induced by an asymmetric central molecule in the unit cell as well as two different azimuthal orientations, see Figure 1.8. This phase transition is completely reversible. Figure 1.9 shows the cycle through the three phases.
Apart from the structures forming the three phases, there is a disordered low density phases, accompanying phases II and III and a variety of structures that form only small islands within the low density areas. The nature of this disordered phase and the small ordered areas within are discussed in reference [52].

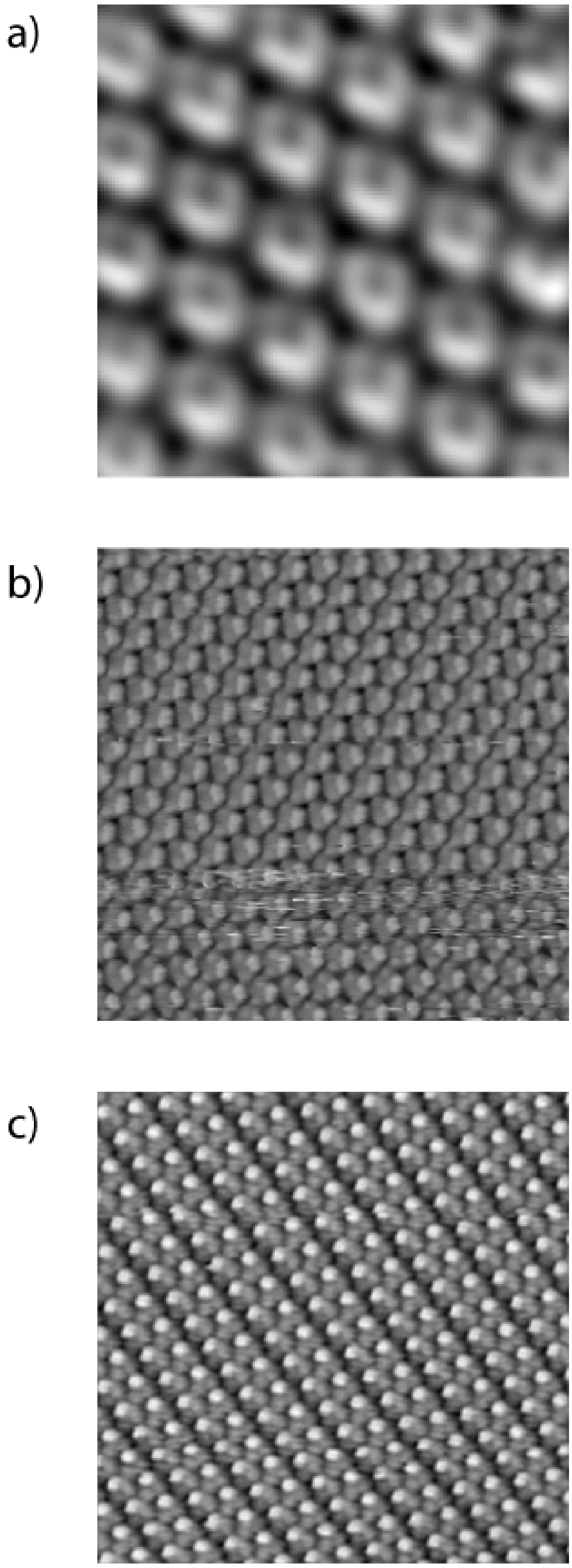

Fig. 1.8 High resolution STM images of the COR / Cu(111) phases. a) (4x4) at RT (5 nm x 5 nm, −0.710 V, 50 pA) b) (4 0, 3 7) at 220 K (15 nm x 15 nm, −2.000 V, 1000 pA) c) (4 2, 0 7) at 50 K (15 nm x 15 nm, −1.800 V, 80 pA). Images courtesy of L. Merz.

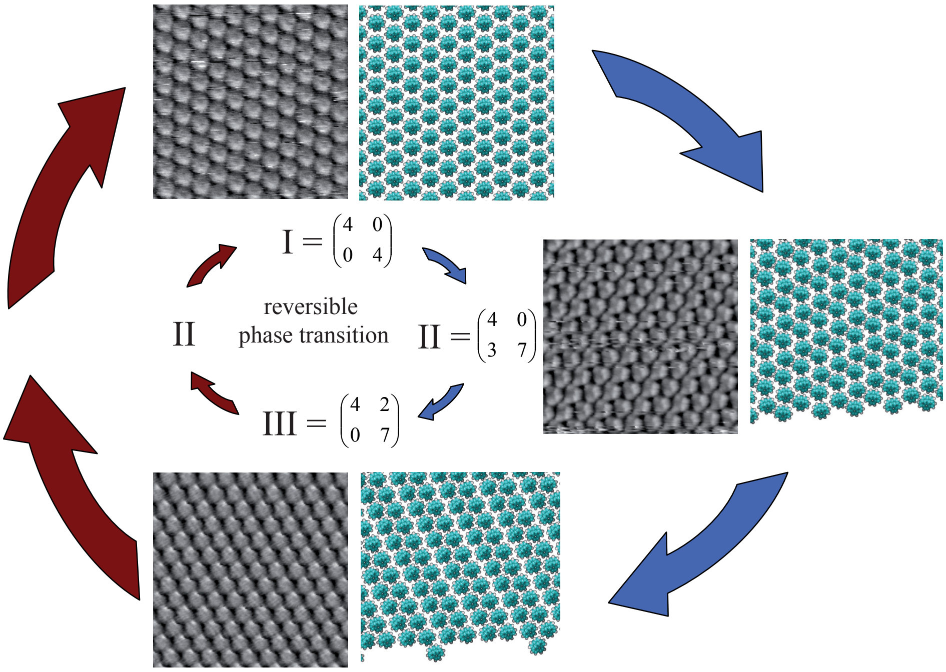

Fig. 1.9 Overview on the corannulene phase transition. When cooling down from the room temperature phase I, phase II forms around 250 K by compressing phase I by 14 %. Upon further cooling phase III is rearranged from phase II (same density). This phase transition is completely reversible with temperature, e.g. phase I will reestablish when the sample is brought back to room temperature [50].

Other Fields of Research on Corannulene

The following listing gives an overview on some of the fields where corannulene plays a role.

- Organometallic chemistry has developed of bowl-shaped polynuclear aromatic hydrocarbons [37, 53–55]. Of special interest are the transition metal complexes for catalytic purposes.
- Due to their relation to the fullerene family, some effort has been made to synthesize C_{60} from bottom up, starting from corannulene derivatives [56,57]. This is of particular interest, since fullerenes can be produced in large scale today, but a goal unachieved so far is still the ”easy” inclusion of ”something” inside the buckyball. These filled buckyballs are called endo-fullerenes [58,59].
- Polyaromatic hydrocarbons are of interest in the identification of the prebiotic matter in the interstellar space [60]. Especially the unusually large dipole moment of corannulene makes it a promising candidate for identification in spectra of interstellar medium [61, 62]
- Fullerenes and carbon nanotubes have been intensely investigated for optical limiters and organic light-emitting diodes. Due to known difficulties in the processing of these molecules, corannulene is thought to be a promising substitute. Blue light emitters have been successfully synthesized from corannulene derivatives in 2007 [63].

1.2 Aim of this Thesis

- The driving forces of self-assembly induce an ordering of adsorbed molecules on metal surfaces. The study of the influence of the inherent molecular fivefold symmetry on the self-assembly process versus the threefold symmetry of the substrate was one topic of this thesis.

- The reversible two-dimensional phase transition described above opens new possibilities to influence polymorphism [50]. The further investigation on this phase transition and the possibility to block phase transition was the second topic motivation.

- Another topic concerns its electronic properties. Due to the expected similar electronic properties with respect to C_{60}, corannulene is thought to be a promising substitution, combining electronic properties with the benefit of much better solubility.

Based on these motivations, the following four question were posed to be answered in the course of this thesis.

1. What is the potential of corannulene in possible electronic applications from a fundamental point of view? Are there indications, that corannulene or its derivatives may be promising alternatives to fullerenes?

2. What is the influence of the inherent fivefold symmetry of corannulenes on their self-assembly behavior?

3. What is the influence of the size of side groups on the self-assembly behavior?

4. Can the two-dimensional reversible phase transition of corannulene be influenced towards one of the polymorphs?

Chapter 2

Experimental

2.1 Methods

All experiments have been conducted in the Molecular Surface Science group of the Swiss Federal Laboratories for Materials Science and Technology - Empa, the Berlin Electron Storage Ring for Synchrotron Radiation (BESSY II) and the Surface Science Group at the Karl-Franzens Universität Graz, Austria.

2.1.1 Ultra High Vacuum - UHV system

The ESCA (Electron Spectroscopy for Chemical Analysis) system at the Molecular Surface Science group was used for most of the experiments concerning photoelectron spectroscopy (PES) of this work. Figure 2.1 shows a scheme of the UHV system with the most important components. The system was pumped with turbo molecular and ion getter pumps to a base pressure below $2 \cdot 10^{-10}$mbar. This ESCA system allowed X-Ray Photoelectron Spectroscopy (XPS), Ultraviolet Photoelectron Spectroscopy (UPS), Low Energy Electron Diffraction (LEED) and Temperature Programmed Desorption (TPD) experiments. The chamber itself was an experimental unit based on a commercial Physical Electronics ESCA system, equipped with a Perkin Elmer dual anode magnesium / aluminium X-Ray source (04-500) and an electron energy analyzer (10-360). The helium discharge lamp (UV source) for UPS was a SPECS UVS 10/35, the mass spectrometer a HIDEN quadrupol HAL 511/3F and the LEED optic was a SpectaLEED unit by Omicron with a LaB_6 filament. The software operating the energy analyzer was AugerScan by RBD Enterprises.

All STM data were acquired with a commercial Omicron variable temperature STM apparatus. The base pressure in this system was around $5 \cdot 10^{-10}$ mbar. It

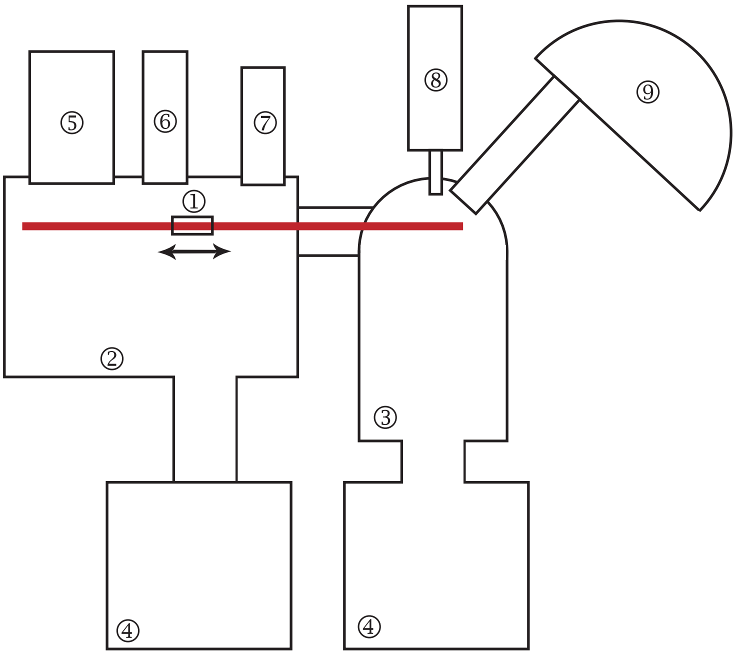

Fig. 2.1 Scheme of the ESCA system: ① sample (moveable with a manipulator); ② preparation chamber; ③ measurement chamber; ④ pumping system; ⑤ LEED optics; ⑥ sputter gun; ⑦ evaporation cell; ⑧ light source; ⑨ electron analyzer

was equipped with the tunneling microscope, a Prisma quadrupol mass spectrometer (QMS200) by Pfeiffer Vacuum and standard sample cleaning facilities.

The angle-resolved UPS (ARUPS, Karl-Franzens University Graz) data and all PES data on Cs doping were acquired on a SCIENTA system with a SES-200 analyzer and with the Toroidal Electron Spectrometer of the University Erlangen-Nürnberg at BESSY II. X-Ray absorption experiments were conducted on the MUSTANG experimental station with a Phoibos 150 analyzer from Specs at the PGM-1 beamline, also at BESSY II. On all systems the same direct current heating, water cooled Knudsen-type sublimation cells were used for deposition of the molecules.

2.1.2 Photoelectron Spectroscopy - XPS and UPS

X-Ray Photoelectron Spectroscopy (XPS) is a widely used surface sensitive spectroscopic technique for quantitative analysis. For a detailed description of the technique we refer to special technical literature [64–66].

The basic principle of XPS is based on the photoelectric effect found by Heinrich

Hertz in 1887. The effect involves electrons being emitted from matter when they are excited above the vacuum level by electromagnetic radiation, bearing enough energy, typically UV light and hard X-Rays. If not performed at a synchrotron, the band of wavelength at hand is usually very restricted. For lab-based XPS the energy is 1253.6 eV for Mg anodes and 1486.6 for Al anodes (Mg anodes used in this work). UPS is typically performed with helium lamps providing UV light with 21.2 eV (helium I) and 40.8 eV (helium II).

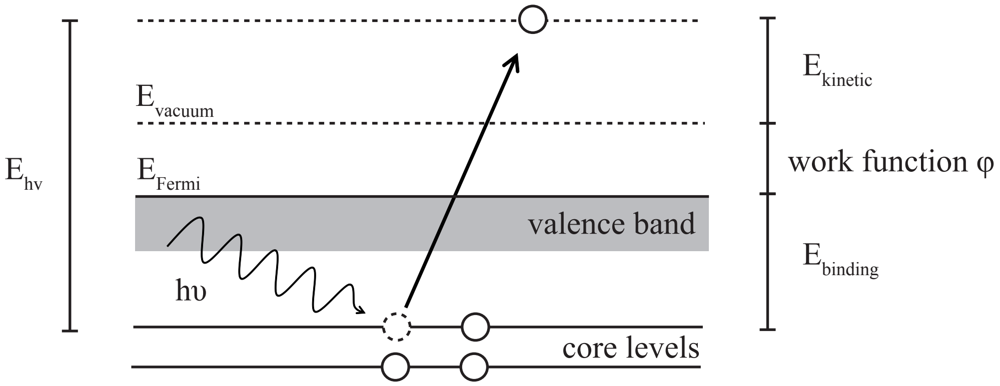

Fig. 2.2 The photoelectric effect: Incoming electromagnetic radiation of the energy $h\nu$ excites an electron. If the excitation is strong enough the electron leaves the solid matter and may be detected in an electron energy analyzer. From the measured kinetic energy, the known photon energy $h\nu$ and the work function ϕ the original binding energy of the electron can be calculated.

An electron of a core level or the valence band is excited above the Fermi energy with a surplus of energy higher than the work function ϕ (Figure 2.2). The energy is provided by the incoming electromagnetic radiation $h\nu$. In UHV the mean free path of the photoelectron is sufficiently large for unscattered electrons to be captured in an energy analyzer. The Einstein equation 2.1 describes the relation of kinetic energy (E_K), binding energy (E_B), photon energy ($h\nu$) and work function (ϕ).

$$E_K = h\nu - E_B - \phi \tag{2.1}$$

The photon energy is well known, since it is specific to the electromagnetic radiation or precisely selected from synchrotron radiation. If the work function of the material is known as well, the binding energy can easily be calculated from the measured kinetic energy. The binding energy can be used to extract information on the chemical species that emitted the electron and the chemical state of the element.

The energy analyzer counts electrons at a certain kinetic energy and the software plots these counts versus the energy (either kinetic or binding). In these plots the counts gather to peaks, representing the density of states in the material. The area under the peaks can be used to determine the qualitative or even quantitative composition of the material.

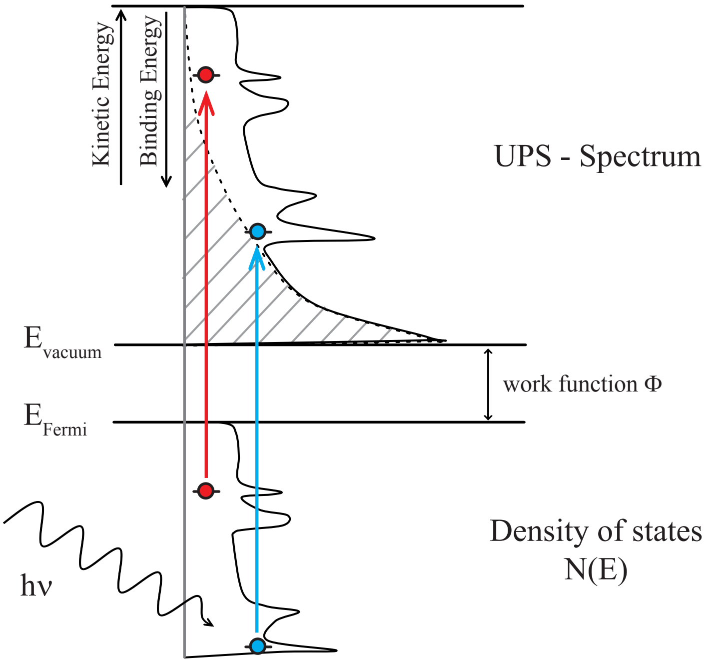

Fig. 2.3 The UPS spectrum is a direct map of the density of states of the electronic structure near the Fermi level. It starts at the Fermi edge and stretches over a kinetic energy range, that is limited by the photon energy minus the work function ϕ of the material. The secondary electron cut-off at $E_K = 0$ can be used to measure the work function of a material. The colored arrows indicate the maximum excitation for any electron from $h\nu$.

While XPS is used to probe electrons of the inner core levels, UPS basically excites electrons of the valence band, including occupied molecular orbitals of adsorbed molecules. In addition, the work function of the material can be determined. Figure 2.3 shows how the UPS spectrum of a material results from the density of states near the fermi level. It consists of the broadened discrete energy states of the electronic system and a number of secondary electrons, which increase in intensity until the cut-off at zero kinetic energy. Electrons that have a higher binding energy than the energy of the UV light minus the work function cannot leave the sample.

2.1.3 Near Edge X-Ray Absorption Fine Structure

Near Edge X-Ray Absorption Fine Structure (NEXAFS) is an electron spectroscopy technique probing the electronic structure of a system from a few eV below to up to 30 eV above an X-ray absorption edge. A detailed introduction to NEXAFS gives reference [67].

While in XPS the photoelectron itself is analyzed regarding its energy, in NEXAFS the fluorescent photon, Auger electrons and inelastically scattered photoelectrons may also be measured. This has the great advantage, that the final state of the photoelectron does not have to be an extended free-electron state, like for XPS, but can be a bound state (like an exciton) since the photoelectron itself need not be detected (Figure 2.4). Briefly, this means that NEXAFS measures the total joint density of states of the initial core level with all final states, consistent with conservation rules [67,68]. The experimental setup used in this thesis was equipped to measure the total electron yield.

The fact, that bound final states contribute to the spectrum as well, makes this technique ideal for probing narrow final states in the solid, such as an exciton. In case of organic thin films on metal surfaces the important states to probe are the unoccupied π^* and σ^* states, by excitation for example of a C 1s level electron into these states.

Because of dipole selection rules, this technique is often used when orientation of adsorbates is of interest. Since the X-ray source for NEXAFS is polarized (synchrotron radiation), the orientation of molecular orbitals and therefore the molecules itself can be directly determined by polar and azimuthal scans.

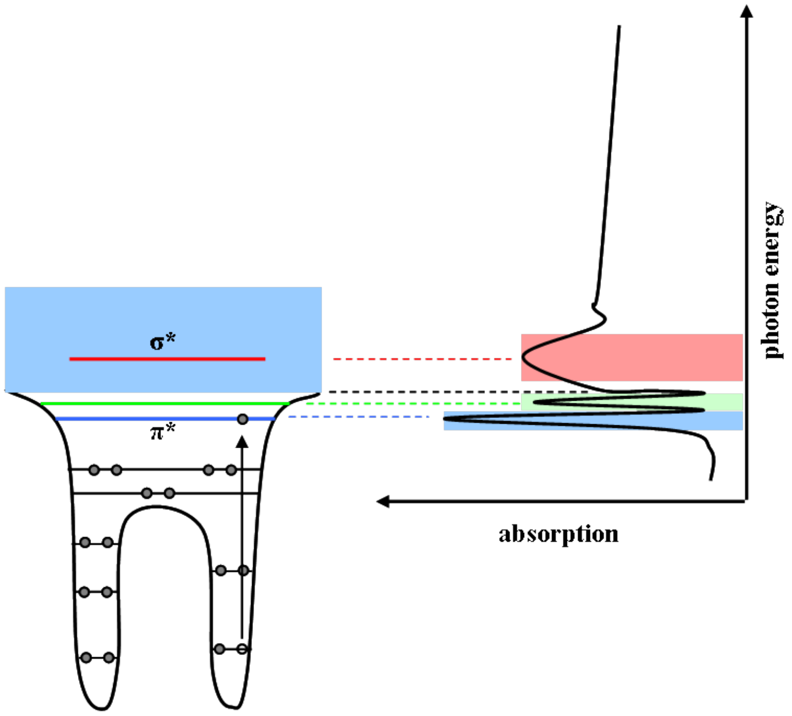

Fig. 2.4 When core electrons are excited into an unoccupied state of the valence band by X-rays, this excitation shows as a peak in the absorption spectrum, excitations into the continuum give the background of the spectrum. Since the final states of the electrons are very narrow, the peaks are relatively sharp and easy to identify.

2.1.4 Low Energy Electron Diffraction - LEED

Low Energy Electron Diffraction is used to analyze two dimensional crystal structures of surfaces. It is of great importance in investigating organic thin films on metal surfaces due to its low destructive influence on the organic films and due to the fact, that the average structure of a wide area (up to 1 mm^2) is analyzed. This includes not just a single terrace or domain, but a wide area with all the rotational and mirror domains within.

Electrons with 15 to 500 eV kinetic energy are directed towards the sample, usually at normal angle incidence. Electron energies between 15 and 100 eV are used to probe organic thin films. The electrons are back-scattered from the substrate lattice as well as the regularly adsorbed layer resulting in a superposition of the substrate and the adlayer structure on a fluorescent screen in the LEED optics. A digital camera is used nowadays to monitor the diffraction pattern on the fluorescent screen. See Figure 2.5 for a schematic drawing of a LEED optic.

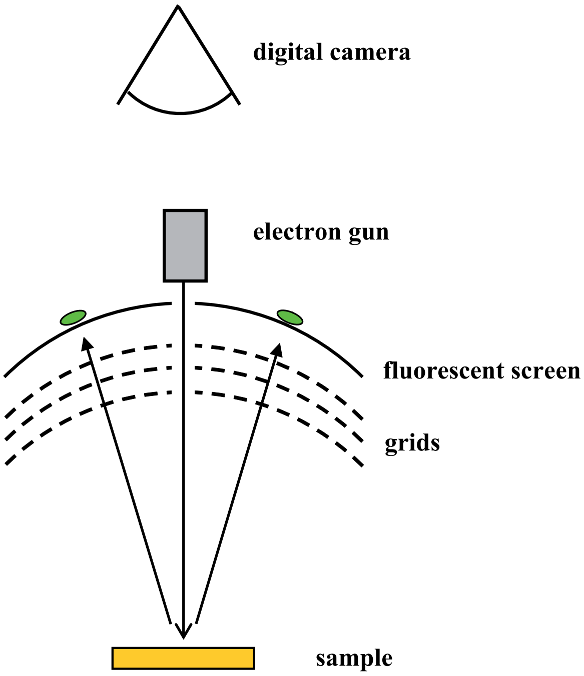

Fig. 2.5 Schematic drawing of a LEED optic. Electrons are generated in the electron gun and accelerated towards the surface. Only elastically back scattered electrons pass by a series of grids and are accelerated onto the fluorescent screen. A digital camera captures the diffraction pattern from behind the screen.

LEED theory evolves around the Bragg condition of diffraction discovered by William Lawrence Bragg and William Henry Bragg in 1913. The Bragg diffraction dictates, that electrons striking a periodical lattice under an incident angle ϕ_0 will be backscattered with constructive interference under the following condition (see Figure 2.6)

$$L_2 - L_1 = a \cdot (sin\phi - sin\phi_0) = n \cdot \lambda,\ n = 0,\ 1,\ 2,\ 3\ldots \tag{2.2}$$

with λ being the De Broglie wavelength of the incident electron.
The Bragg condition can be easily extended to two-dimensional lattices. The linear distance a from equation 2.2 is replaced by the lattice constants symbolized by $d_{[h,k]}$.

The observed LEED pattern on the screen is a scaled representation of the reciprocal lattice which is defined by reciprocal vectors:

$$\vec{a_s^*} \text{ and } \vec{b_s^*} \text{ (substrate)}$$

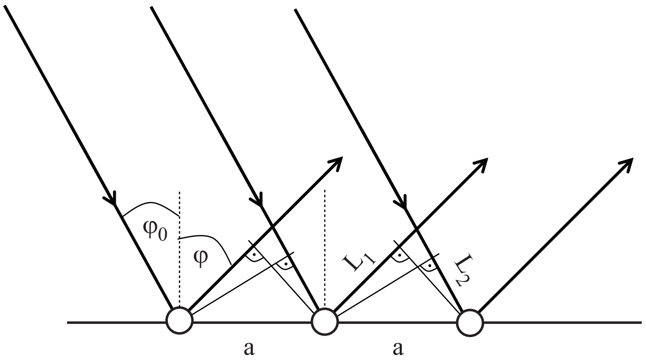

Fig. 2.6 Schematic illustration of the Bragg condition. The periodicity a dictates the lengths L_1 and L_2 together with the incident angle ϕ_0. Only if the difference between L_1 and L_2 is equal to a multiple of the De Broglie wavelength of the electrons, constructive interference can occur, producing a spot on the LEED screen.

$$\vec{a^*} \text{ and } \vec{b^*} \text{ (adlayer)}$$

The scalar product connects the real space unit vectors with the reciprocal vectors (both for substrate and adlayer structures):

$$\vec{a^*} \cdot \vec{a} = \vec{b^*} \cdot \vec{b} = 1$$

The relation of an adlayer and the substrate structure is also transformed into the reciprocal space and can be observed in a LEED pattern. The relation is inverted as well as the following simple example of a (2x2) adlayer structure on a Cu(111) substrate shows (Figure 2.7).

The following sources give a detailed insight in LEED theory in special and in electron diffraction in general [69–71].

To analyze the patterns, the images were enhanced for better visibility with IrfanView 4.25[a]. Enhancement consisted of color inversion, gamma correction and contrast increase, if not otherwise stated.
The LEED pattern simulator LEEDPat 2.0[b] was used to analyze the images and compare the matrices of the superstructures that were determined.

[a] `http://www.irfanview.com/`

[b] `http://www.fhi-berlin.mpg.de/KHsoftware/LEEDpat/`

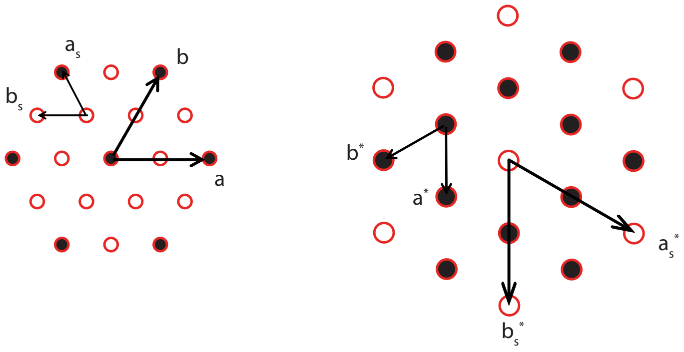

Fig. 2.7 Real space versus reciprocal space. A (2x2) superstructure in the real space (left) is transformed into the reciprocal space (right). All reciprocal vectors are connected to their real space counterparts with the scalar product.

2.1.5 Scanning Tunneling Microscopy - STM

Scanning Tunneling Microscopy was invented in 1982 by Gerd Binnig and Heinrich Rohrer [72–75] and has become one of the most important techniques in surface science. It delivers only results from a very small area of the sample and should be accompanied by averaging techniques such as LEED or electron spectroscopy.

The working principle of STM is based on the tunneling effect used by George Gamow in 1928 to explain alpha decay. However, it was first applied by Friedrich Hund in his quantum mechanical explanation of molecular spectra in 1927. The tunnel effect proposes, that a particle has a finite probability to exist behind a potential barrier, without overcoming it. The probability depends on the height of the barrier. The tunneling probability of electrons (transmission coefficient) is given by the following equation 2.3.

$$T(E) \propto \frac{E}{V_0} \cdot e^{-ka} \tag{2.3}$$

with E being the energy of the electron, V_0 the height of the one-dimensional potential barrier, k the momentum of the electron and a the width of the potential barrier, a.k.a the tunnel distance. The tunneling probability increases with the energy of the electron, which in turn depends on the bias voltage difference between the tip-shaped electrode and the surface. The probability drops drastically with tunnel distance. Therefore it is of great importance to approach the tip very close to the surface. The barrier height V_0 is a reciprocal representation of the conductance of the tunnel gap, which is strongly influenced by the density of states at the surface. Only if there is a state through which charge carriers may travel, the conductivity is high.

The schematic set-up of STM is shown in Figure 2.8. The main parts of the design are the piezo stage moving the tip with high precision and the electronics amplifying the tunnel current and controlling the tip-sample distance.

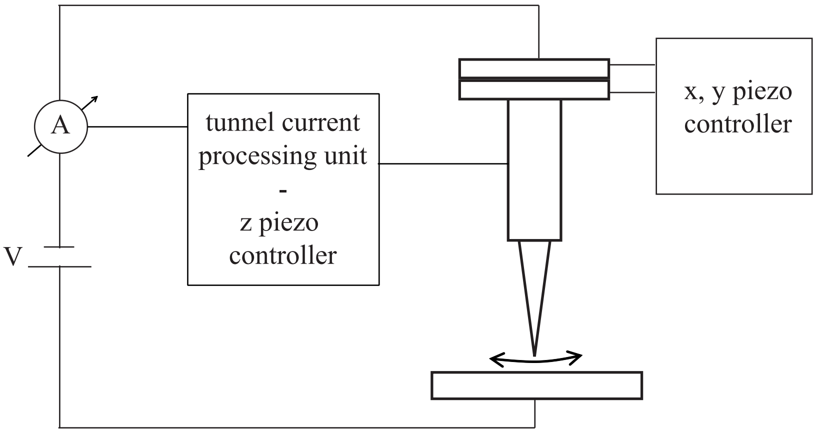

Fig. 2.8 Schematic set-up of STM. A voltage V is applied between the tip an the surface, resulting in a tunnel current, that is amplified and adjusted to a certain value, by adjusting the tunnel distance with the piezo. The scanning pattern is achieved by other piezos, controlling the movement of the tip in x and y direction, i.e. parallel to the surface.

STM images are constructed from line scans over the surface, mapping the control voltage of the distance, which is adjusted on the feedback and the tunnel current. This means that the images are color representations of the topography intermixed with the density of states at the surface.
Although STM has evolved very rapidly in the last three decades, the basic working principle is still the same. More details of this technique are found in references [76, 77], for a good overview on the manyfold applications from a practical point of view, see reference [78].

Data Analysis

All STM images of this thesis are plane subtracted and flattened. If other modifications were made to the raw data image, it is stated in the figure caption. All processing for publishing of the STM images was done in WSxM 3.0[c] [79]. All analyses on unit cells were done through Fourier Transformation in SPIP - The Scanning Probe Image Processor 3.004 by Image Metrology[d].

---

[c] `http://www.nanotec.es/`

[d] `http://www.imagemet.com/`

2.2 Materials

2.2.1 Substrates

Three different Cu(111) crystals (MaTeck[e]) showing a purity $> 99.999\,\%$, a roughness of maximum $0.03\,\mu$m and orientation precision below $0.15\,^{\circ}$ were used in this thesis. Their cleanliness was checked by XPS, UPS, STM and LEED.

Standard cleaning procedures consisted of forty minutes Argon ion sputtering followed by two minutes annealing at 600 °C or two times twenty minutes Ar sputtering, each time followed by two minutes annealing at 600 °C. The cleaning effect was found to be identical with either procedure.

2.2.2 Corannulene - COR

Our collaborators at the Organic Chemistry Institute at the University of Zürich[f] provided corannulene and its derivatives.

Corannulene was additionally purified in the UHV system by outgassing at 90°C for 15 hours. It was deposited onto the substrate by sublimation at 110°C for 15 minutes to achieve one monolayer of molecules on the substrate. These parameters change with time in the UHV system, due to different amount of molecules in the cells. 1 ML coverage was calibrated using UPS and LEED on a regular basis.

---

[e] `http://www.mateck.de`

[f] `http://www.oci.uzh.ch`

2.2.3 Pentamethyl-Corannulene – Me_5COR

Me_5COR ($C_{25}H_{20}$, 320.43 g/mol) is one of the penta-substituated derivatives synthesized from Cl_5COR. It was first synthesized by J. Siegels group in 1999 [36] (Figure 2.9).

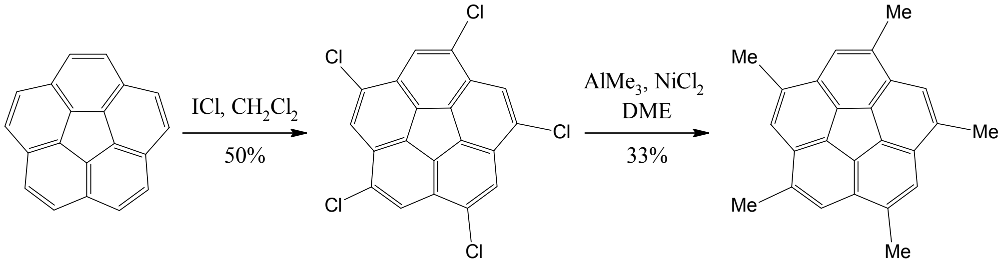

Fig. 2.9 Conversion of Cl_5COR to Me_5COR by a general coupling procedure with alkyl aluminum reagents in the presence of a catalytic amount of nickel. Also the conversion to other derivatives may follow this approach [36].

Me_5COR was further purified in UHV by outgassing at 120°C for 15 hours in a sublimation cell. It was evaporated onto the substrate at 140°C for 15 minutes to achieve one monolayer of molecules.

2.2.4 Tartaric Acid

Tartaric acid was used to stabilize a COR polymorph as a chiral additive of the COR/Cu(111) system. Therefore, tartaric acid on Cu(111) by itself was investigated to check that the LEED patterns that were found for the stabilized COR polymorph were not by chance a tartaric acid structure.

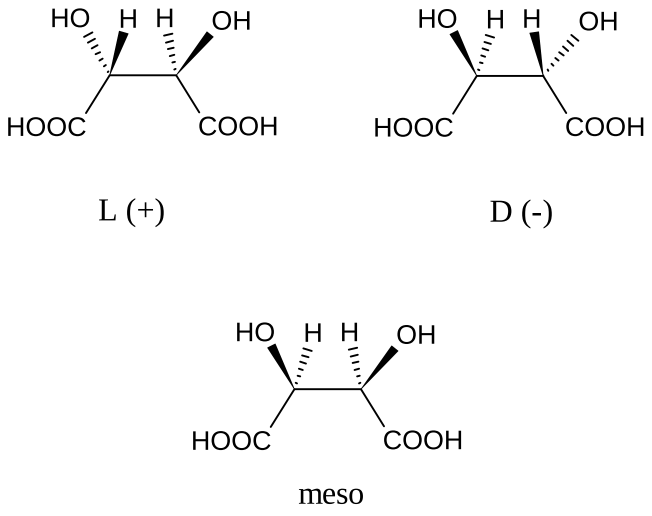

Fig. 2.10 The three types of tartaric acid. In the top row the two chiral enantiomers L- and D-tartaric acid, below the achiral form meso-tartaric acid.

Tartaric acid exists in an intrinsically chiral form (L- and D-tartaric acid) as well as in an achiral form (meso-tartaric acid), see Figure 2.10. Only chiral tartaric acid was used here as chiral additive of the corannulene Cu(111) system.

Tartaric acid was purchased from Sigma-Aldrich[g]. D- and racemic tartaric acid showed both a purity of 99%, L-tartaric acid 99,5%. All three substances were introduced into the UHV system without further purification.

L-, D- and racemic tartaric acid were degassed at 90 °C for 15 hours for further purification in the sublimation cells.

Sublimation parameters for deposition of one monolayer were 110 °C for 15 minutes for L- and D-tartaric Acid and 130 °C for 15 minutes for racemic tartaric acid.

[g] `http://www.sigmaaldrich.com`

Chapter 3

Self-Assembly of Pentamethyl-Corannulene – Me_5COR

The growth of the molecular layer in the substrate was monitored by XPS, UPS and LEED. Figure 3.1 shows the XPS analysis of one monolayer Me_5COR on Cu(111) compared to the freshly cleaned copper substrate, regarding the C 1s and Cu 2p peaks. The full scale spectrum of the copper substrate was used besides UPS, LEED and STM to analyze the cleanliness of the substrate before deposition.

TPD was measured to investigate the desorption of the multilayer and the decomposition of the monolayer (Figure 3.2). The multilayer desorbs at 350 K and the first layer decomposes in two steps at 542 K and 620 K. The two steps might be associated with the release of the different bonded hydrogen from the methyl groups and the rim of the bowl. Non-substituated COR shows only one peak in hydrogen TPD at 570 K. The peak area ratio from simple gaussian peak fitting for Me_5COR is 3 : 1, which supports the hypothesis, that the two peaks may be associated with the different hydrogens. The desorption curve is underlined with the broad baseline peak at 670 K, resulting from hydrogen degassing of the sample holder (compare to corannulene TPD in Figure 4.2).

Two coexisting phases were found for Me_5COR at room temperature and low temperature. Their densities differ by 25 %, identifying one as a low density meta-stable phase and the other as the stable 1 ML phase. Although they were found to coexist at coverages between 0.75 to 0.9 ML, at a coverage of 1 ML only the high density phase is found. The meta-stability of the low-density phase is highlighted by the fact, that it can not be imaged by STM, but rather rearranges into the high-density phase.

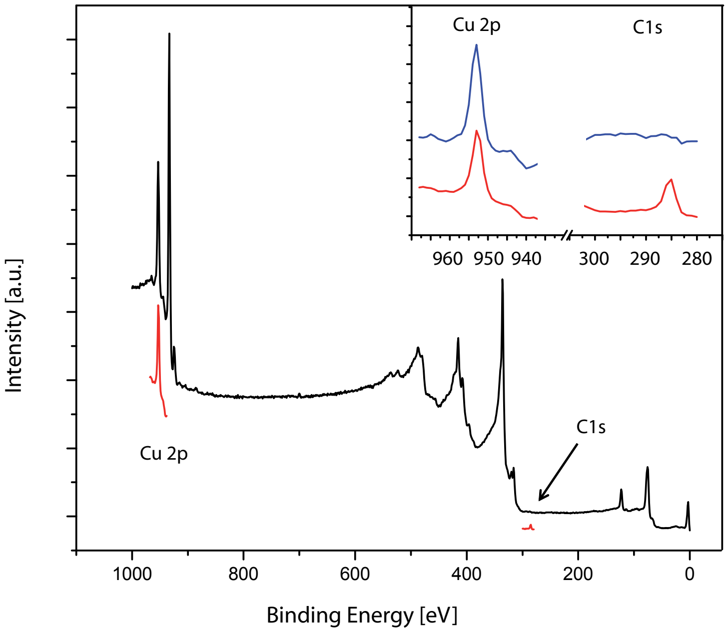

Fig. 3.1 XPS measurement on freshly cleaned Cu(111) (black) and one monolayer of Me$_5$COR (red) with the Cu2p and C1s peak. Inset: Close up of the C 1s and Cu 2p peaks for one monolayer of Me$_5$COR (red) and clean copper (blue).

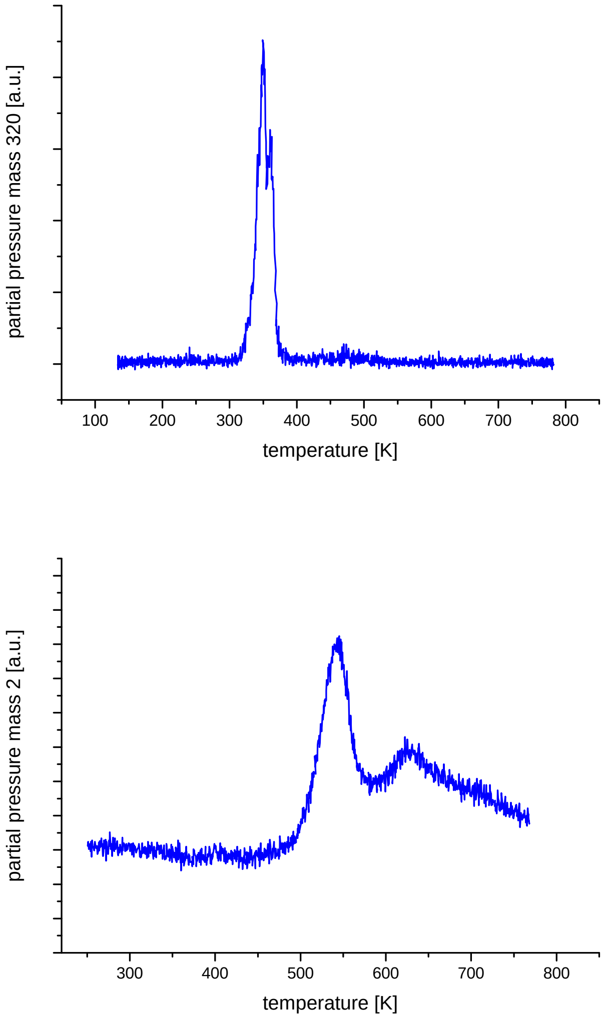

Fig. 3.2 Temperature programmed desorption measurement of Me_5COR at mass 320 (top) and mass 2 (bottom).

3.1 High Density Phase

The adlayer matrix of the full 1 ML coverage structure is $\left(\begin{smallmatrix}10 & 3\\ -3 & 7\end{smallmatrix}\right)$ as determined by LEED and STM. The structure features two mirror domains (Figure 3.3), covering the whole substrate in coexistence.

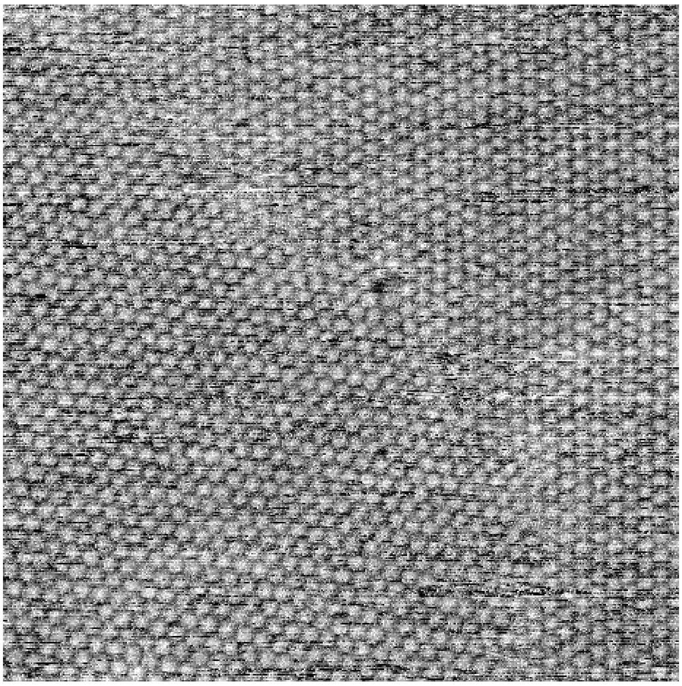

Fig. 3.3 40 nm x 40 nm STM image of the $\left(\begin{smallmatrix}10 & 3\\ -3 & 7\end{smallmatrix}\right)$ and $\left(\begin{smallmatrix}10 & 3\\ 7 & 10\end{smallmatrix}\right)$ mirror domains of Me_5COR on Cu(111). −1.162 V, 97 pA, RT.

At room temperature the structure displays its seemingly long-range ordering over large areas, but the molecules can not be imaged with sub-molecular resolution. They appear only as round entities in a hexagonal lattice (Figure 3.4). To resolve the individual molecular orientation, measurements at low temperatures around 50 K are required.

Figure 3.5 shows two high resolution STM images measured at roughly 50 K. Different than corannulene on Cu(111), the molecules do not appear to be tilted to one side, but to be lying with the central fivefold ring parallel to the surface. This indicates, that the bulky methyl groups on the rim provide steric hinderance with the substrate. These images display the nature of the ordering of the $\left(\begin{smallmatrix}10 & 3\\ -3 & 7\end{smallmatrix}\right)$ structure. The seemingly perfect ordering at room temperature is exposed as a time-averaged effect of the wiggling and rotating molecules, giving each Me_5COR the appearance of sitting in the exact spot, perfecting the layer. At low temperature the monolayer

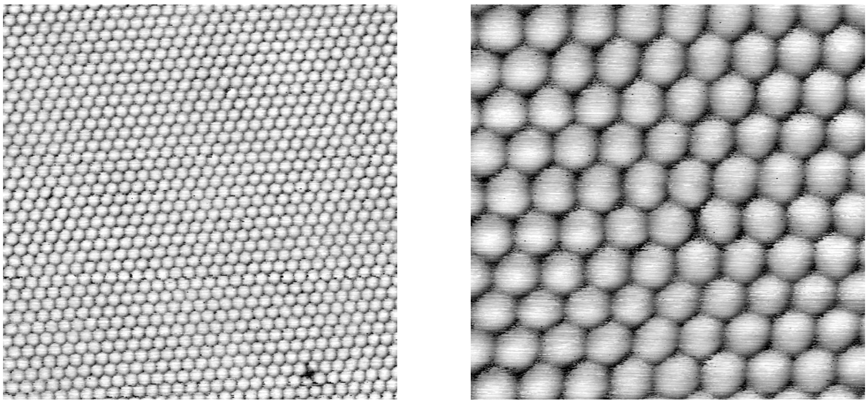

Fig. 3.4 Left: 35 nm x 35 nm STM image of the $\left(\begin{smallmatrix}10 & 3\\ -3 & 7\end{smallmatrix}\right)$ Me_5COR structure. -1.008 V, 238 pA, taken at RT, flattened. Right: 10 nm x 10 nm STM image of the same Me_5COR structure. -1.008 V, 233 pA, taken at RT, flattened.

is revealed by STM to be full of zero-, one- and even two-dimensional defects (i.e. vacancies, line-wise displacement of multiple molecules, random azimuthal orientation over multiple molecules). The long range ordering on average is precise and is responsible for the distinct LEED pattern displayed in Figure 3.8. The short range ordering, however, is only perfect over distances of approximately ten molecules on average. As can be seen clearly in Figure 3.5 left, the row-like ordering is then interrupted by areas of high defect density. The most common defects are azimuthal disorientation of the individual molecule and row-wise displacement. These areas can stretch over a couple of molecules or extend over large areas in rare cases. The nature of this high number of defects in the layer can be explained with a very weak phase transition between the time-averaged room temperature state and the frozen 50 K state. Both phases together show the same LEED pattern and have the same density in average over large areas. Whereas the room temperature state is stabilized over the jiggling motion and rotation of every single molecule, the low temperature state forms actually two phases of slightly different density. They stretch over too small areas to be resolved individually by LEED, and result in the same LEED pattern as the room temperature phase.

Dense fivefold packing is achieved in the same way as seen in macroscopic pentagon systems. Being slightly denser than the RT phase, there exist also areas of lesser density that show up as disordered islands (in the row-like assembly in Figure 3.5). The density is only slightly lower and resembles a pentagon packing that is known as the rotator phase, while the densest areas are analogue to the striped phase (Figure 1.5 in the introduction).[a]

---

[a] Similar applies for Cl_5COR on Au(111), see the appendix.

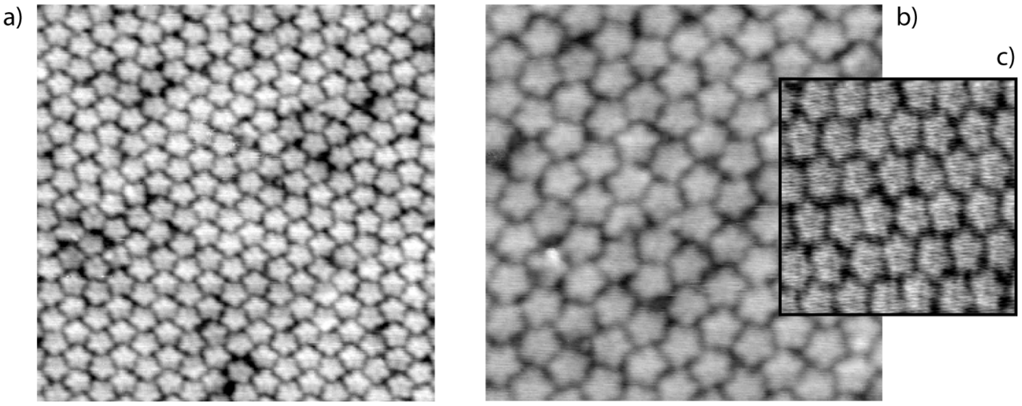

Fig. 3.5 a) 17 nm x 17 nm high resolution STM image of the close packed Me_5COR structure (−1.452 V, 428 pA, 46 K). b) 11 nm x 11 nm high resolution STM image of the same structure (−1.452 V, 428 pA, 46 K, single line corrected). This image shows small patches of the rotator phase and the striped phase. c) Larger area (8 nm x 8 nm) showing the rotator phase only.

Tentative models of the rotator phase and the stripes phase are presented in Figure 3.6. The space group for the striped phase is *p2mg* [80]. However, other interpretations disregard both the glide plane and the twofold rotational symmetry points as no true symmetry elements due to the packing density and assign the space group to *pm* [43]. The matrix for the presented structure is $\begin{pmatrix} 5 & 2 \\ 1 & 8 \end{pmatrix}$ with two molecules per unit cell. This results in a density of 19 copper atoms per molecule. This is an increase of almost 4 % compared to the averaged $\begin{pmatrix} 10 & 3 \\ -3 & 7 \end{pmatrix}$ structure. Beside these high density areas there are the lower density areas formed by the rotator phase.
On the right of Figure 3.6 a tentative model for the rotator phase by itself is given. The random azimuthal orientation of the molecules prohibits any symmetry elements and a space group can not be assigned. The packing density for this phase is slightly smaller than for the striped *p2mg* phase. The matrix for the presented structure is $\begin{pmatrix} 5 & 2 \\ 2 & 5 \end{pmatrix}$, resulting in a density of 21 copper atoms per molecule. This is a decrease of 6.5 % compared to the density of the averaged structure.

A tentative model of the situation, where rotator phase areas interrupt the stripes phase, is presented in Figure 3.7 with pentagons representing the molecules to highlight the azimuthal orientations. The lower model in Figure 3.7 shows the same, illustrated with schematic molecular models.

The averaged structure was confirmed with LEED at room temperature and 50 K. This indicates that the structure in average does not change with temperature. Figure 3.8 gives an overview with the copper spots included at 56 eV electron

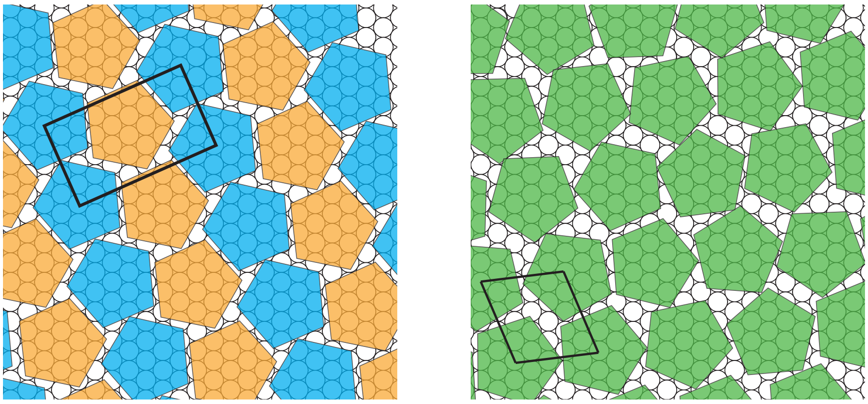

Fig. 3.6 Left: Model for the striped phase on Cu(111). The adlayer without considering the substrate belongs to the two-dimensional space group *p2mg*. From this model the structure matrix (5 2, 1 8) is derived. Right: Model of the rotator phase of the same system. The individual building blocks are randomly rotated around their central axis. The matrix is derived as (5 2, 2 5), resulting in a 10 % lower density than the striped phase.

energy, together with the corresponding LEEDPat simulation, illustrating the superposition of the two mirror domains. A close-up at 14 eV shows the specific feature of this pattern.

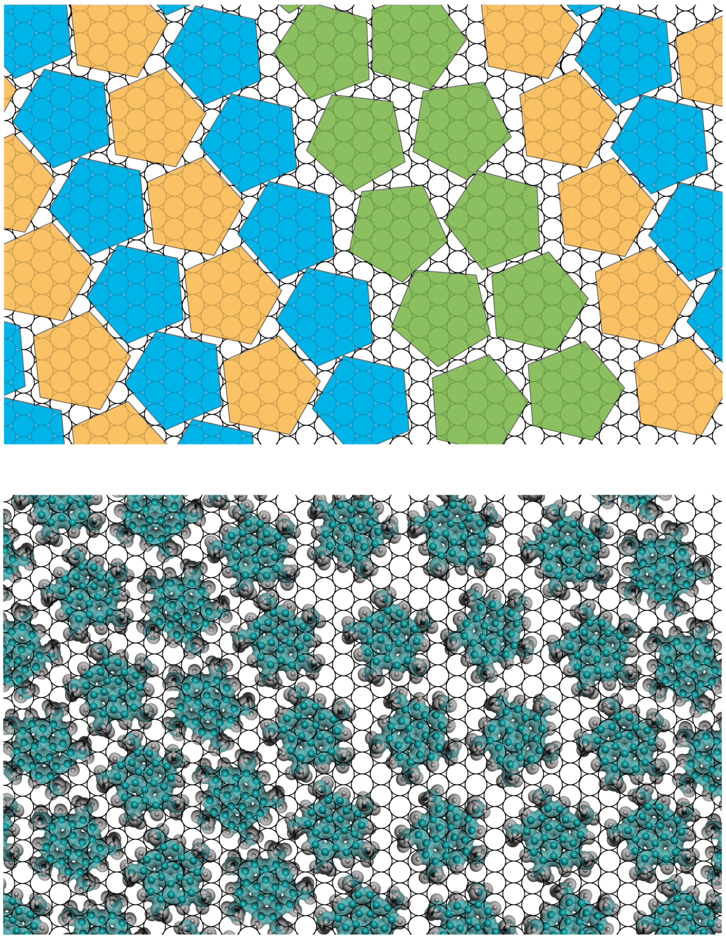

Fig. 3.7 Tentative model of the $\left(\begin{smallmatrix}10 & 3\\ -3 & 7\end{smallmatrix}\right)$ structure. Molecules are represented with colored pentagons (top), to illustrate the azimuthal orientation in the row-like phase (blue / yellow) and the random areas (green). Bottom: The same model with space filling molecules.

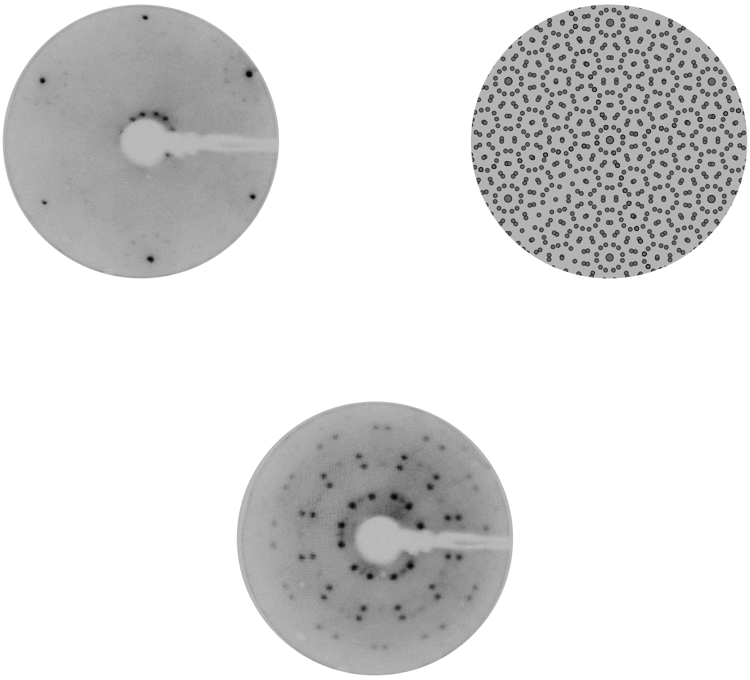

Fig. 3.8 left: LEED pattern of the $\left(\begin{smallmatrix}10 & 3\\ -3 & 7\end{smallmatrix}\right)$ structure, measured at 56 eV. right: LEEDPat simulation of the same structure. Due to the high electron energy the structure can not be resolved in full detail. The dark ring in the center of the LEED image corresponds to the circle of radial doublets in the simulated pattern. The doublets are the characteristic feature of this pattern, as can be seen in the 14 eV sample (bottom).

The two phases found for the high density phase of Me_5COR correspond very well to the calculated [44] and experimentally found [42, 43] packing regimes for macroscopic rigid pentagons, as described in section 1.1.3 of the introduction. The rotator phase and the striped phase differ only little in molecule density per surface area, however both are found for the full monolayer of Me_5COR in coexistence.
Corannulene exhibits fivefold symmetry as well. However, it does not assemble in a pentagon packing motif, but builds a hexagonal lattice. Corannulene tilts to one side in order to align one of the six-membered rings parallel to the Cu(111) substrate. This tilting reduces the molecules symmetry with regard to the substrate from C_{5v} to C_s (a simple mirror plane). This symmetry reduction bypasses the unfavorable fivefold symmetry and allows the molecule to assemble in a hexagonal lattice. Me_5COR lacks the ability to tilt in the same way as COR, due to the bulky sidegroups. The molecule is forced to expose its fivefold symmetry to the substrate and the neighboring molecules. According to the dense packing regimes for pentagons the molecules are driven by self-assembly forces into dense arrays [81], mimicking the antiparallel rows found for macroscopic pentagons.

The three structures found for COR and Me_5COR are summarized in Figure 3.9 together with an overlay of pentagons to illustrate the orientation of individual molecules. As described earlier, in the COR (4x4) monolayer all molecules are oriented in the same direction (and tilted in the same direction as well).
The Me_5COR molecules are arranged in row-like fashion with 180 ° alternating orientation, over large areas, only interrupted by defect rich areas, that are in fact small islands of the rotator phase. Larger areas of the rotator phase can be found as well.

Another possible reason for COR and Me_5COR not adapting the same packing regimes can be found in the outer shape of the molecules, as they present themselves to their neighbors. The shape of a COR molecule is in first approximation rather a circle than a pentagon , see Figure 3.10. The shape of a Me_5COR molecules is less roundish and shows clear similarity to a true pentagon, the bulky methyl groups however indicate, that perfect pentagon tiling might be disrupted for this molecule. Pentachloro-corannulene (Cl_5COR) on the other hand exhibits a well defined pentagon shape, due to the less bulky substituents.
Despite the imperfect pentagon shape of Me_5COR, it does assemble in the known dense packing regimes, although there are indications, that the molecule is not perfectly suited for this sort of packing, due to the large number of defects. This

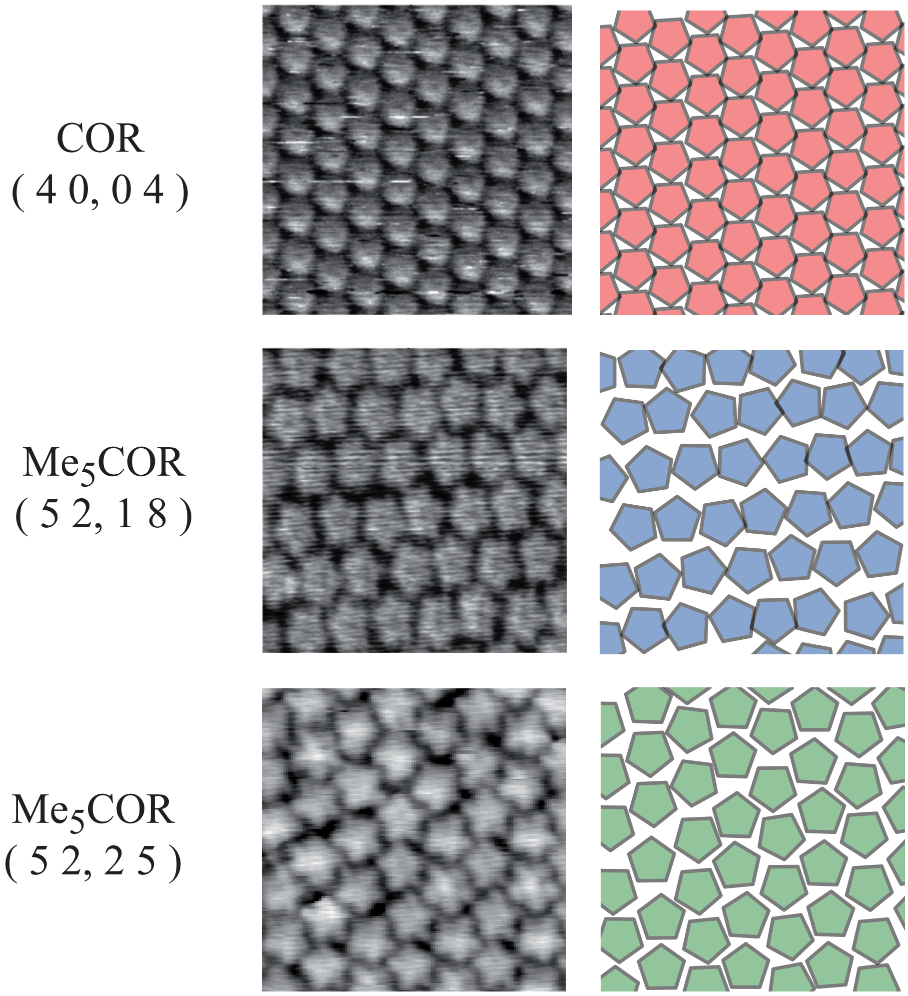

Fig. 3.9 8 nm x 8 nm high resolution STM images of corannulene and Me$_5$COR and their schematic pentagon representations. The COR (4x4) is a perfect hexagonal lattice, the Me$_5$COR rotator phase (middle) is quasi-hexagonal with a lot of defects and the Me$_5$COR stripes phase (bottom) is row-like arranged.

might be due to the deviation from a perfect pentagon or by a mismatch of molecular lateral packing and the availability of certain substrate binding sites.
Cl$_5$COR, for example, self-assembles into a striped pentagon packing with very little defects on a stepped Au(111) substrate [82], see appendix for STM image. The adaption of the row-like phase for Cl$_5$COR might be due to the more pentagon like form as well as a good fit to the substrate lattice on Au(111).

In summary, self-assembly of fivefold symmetric molecules is dominated by strategies to reduce or change the unfavorable symmetry in order to correspond better to the symmetry of the substrate. A similar finding was published by a different group, reporting another corannulene derivative forming trimers in order to fit the Cu(111) substrate [83]. If fivefold symmetry is imposed, the molecules arrange in the same packing regimes found for hard pentagons.

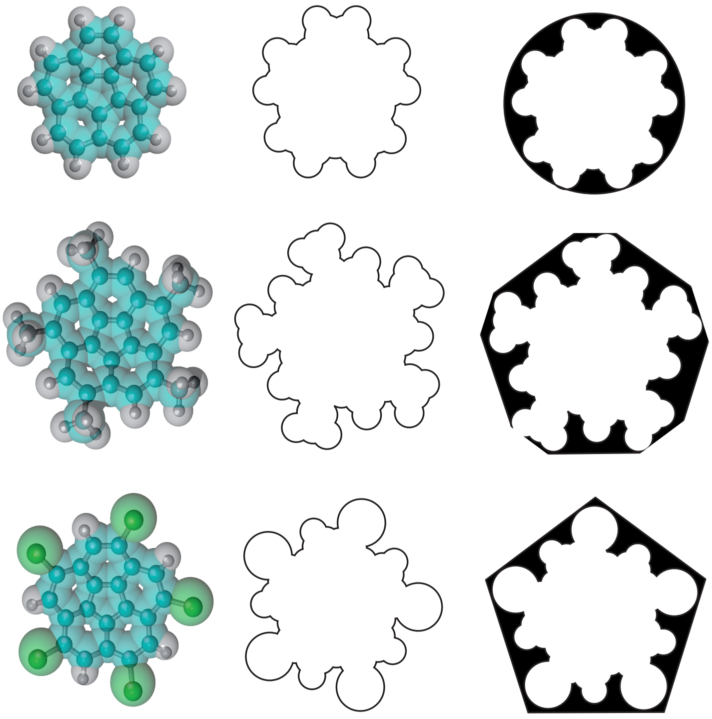

Fig. 3.10 Illustration of molecular shape. Of the three molecules corannulene (top), Me_5COR (middle) and Cl_5COR (bottom) only Cl_5COR comes close to the shape of a pentagon. Corannulene has a circular shape in first approximation, Me_5COR shows a mixture of both shapes.

The presented results provide a reverse modeling situation, implying that mechanical packing rules apply to molecular self-assembly. This means that computational hard-object-modeling can be a valid approach to mimic lattice structures [82].

3.2 Low Density Phase

This structure appears at a coverage of approximately 75 % of a monolayer, in coexistence with the high density phase.
The LEED pattern (Figure 3.11) leaves no doubt about the structure, but STM images of this phase could not be obtained. With beginning STM measurement on a new sample of a $\left(\begin{smallmatrix} 6 & 3 \\ -3 & 3 \end{smallmatrix}\right)$ adlayer, no molecular resolution could be achieved, due to high mobility of the molecules on the surface. Upon scanning for some time the high density structure formed on the surface, possibly because the STM tip pushes together the molecules on terraces, where they stabilize in the high density phase.

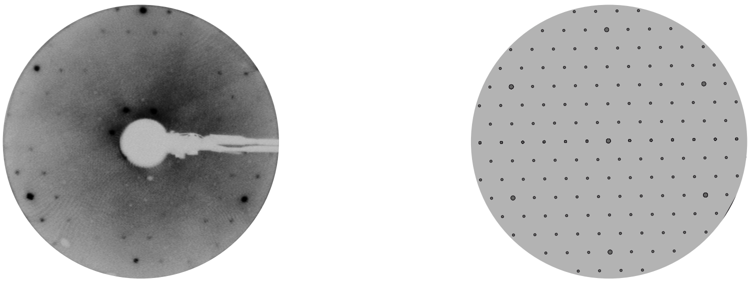

Fig. 3.11 left: LEED pattern of the $\left(\begin{smallmatrix} 6 & 3 \\ -3 & 3 \end{smallmatrix}\right)$ structure, measured at 56 eV. right: LEEDPat simulation of the same structure.

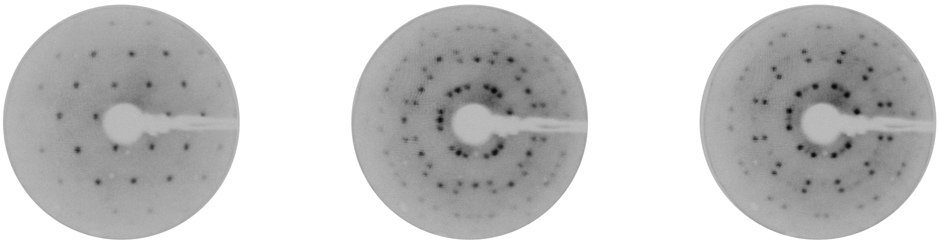

Fig. 3.12 LEED pattern of the $\left(\begin{smallmatrix} 6 & 3 \\ -3 & 3 \end{smallmatrix}\right)$ structure (left), the superposition of the $\left(\begin{smallmatrix} 6 & 3 \\ -3 & 3 \end{smallmatrix}\right)$ and the $\left(\begin{smallmatrix} 10 & 3 \\ -3 & 7 \end{smallmatrix}\right)$ high density phase (center) and the pure $\left(\begin{smallmatrix} 10 & 3 \\ -3 & 7 \end{smallmatrix}\right)$ phase (right). All measured at 14 eV.

Upon deposition of about 85 % of a monolayer, the two phases $\left(\begin{smallmatrix} 10 & 3 \\ -3 & 7 \end{smallmatrix}\right)$ and $\left(\begin{smallmatrix} 6 & 3 \\ -3 & 3 \end{smallmatrix}\right)$ coexist on the substrate. Since both structures are stable under the electron beam at low energy, the coexistence can be captured in a superposition of the two LEED patterns, see Figure 3.12.

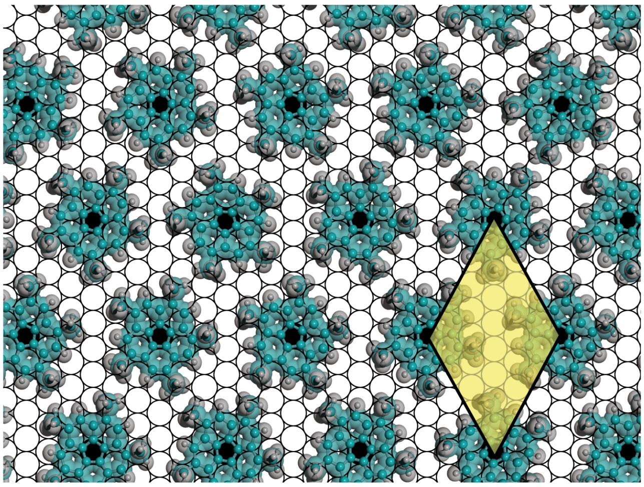

Fig. 3.13 Structure model for the $\begin{pmatrix} 6 & 3 \\ -3 & 3 \end{pmatrix}$ lattice.

A tentative model of the $\begin{pmatrix} 6 & 3 \\ -3 & 3 \end{pmatrix}$ structure is shown in Figure 3.13. The density of this structure is significantly lower than the high density phase. This is a strong indication, that the azimuthal orientation of the molecules is most probably random as well, just like the rotator phase.

3.3 Other phases

By heating a sample with the above described $\begin{pmatrix} 10 & 3 \\ -3 & 7 \end{pmatrix}$ room temperature structure to approximately 380 K followed by a rapid cool down to 50 K, parts of the original structure disappear and reveal a structure with the matrix $\begin{pmatrix} 10 & 5 \\ -5 & 5 \end{pmatrix}$. Figure 3.14 displays STM images of the structure, we also refer to as the "hole phase". The dark entities clearly visible define the rather large unit cells. The shadows are interpreted as blank copper. In a gedanken experiment the phase may be formed from the room temperature structure by squeezing one of four molecules out of the monolayer. The additional space leads to a relaxation in the layer, deforming the just created hole to a triangular form, see Figure 3.15.

A tentative structure model is presented in Figure 3.16. When heated to room temperature, the structure disappears, leading to the high density room temperature structure. The density of the "hole phase" was calculated to be 0.04 molecules per copper atom. The density of the ordinary room temperature structure is 0.05 molecules per copper atom. The molecules that supposedly were squeezed out of the monolayer return to refill the room temperature structure. A possible explanation might be, that the molecules gather at phase boundaries, terrace edges or are just

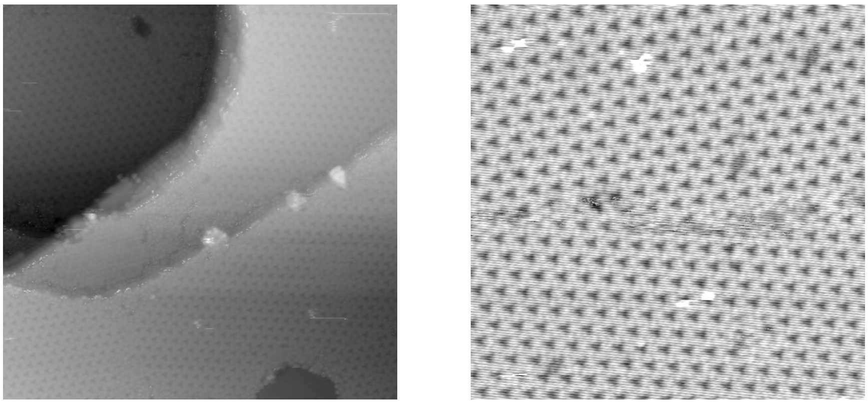

Fig. 3.14 Left: STM image 80 nm x 80 nm, −1.235 V, 455 pA. Right: STM image 37 nm x 37 nm, −1.210 V, 285 pA. Both display the same $\begin{pmatrix} 10 & 5 \\ -5 & 5 \end{pmatrix}$ structure, referred to as the "hole phase".

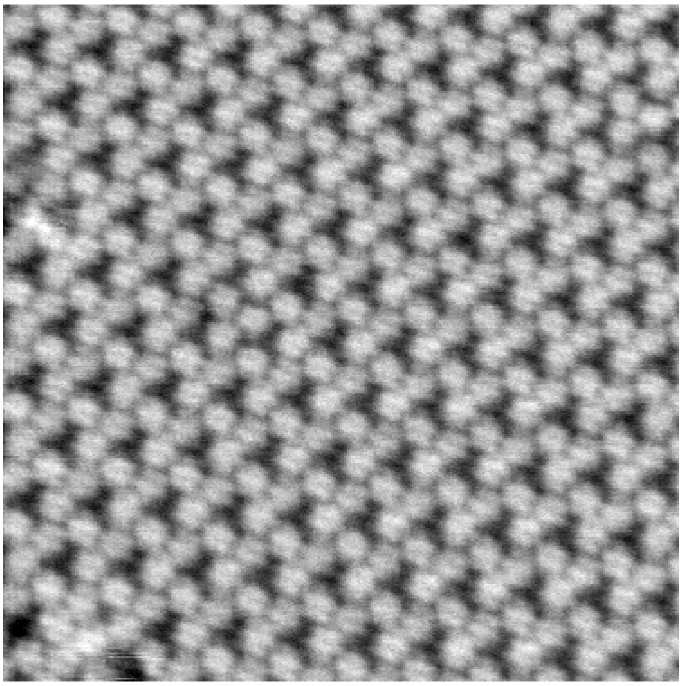

Fig. 3.15 STM image 20 nm x 20 nm, −1.235 V, 455 pA.

mobile in the second layer. Another possible explanation is that the molecules hop out of the monolayer and form a bowl-in-bowl stacking on one of their neighboring molecules.

Independent of the whereabouts of the missing molecule, the phase transition can be interpreted as vibration induced. At elevated temperature the entropy in vibration increases, together with the strain within the monolayer. This results in some molecules being squeezed from the first layer. This process is similar to the phase transition of COR from the stabilized phase II to phase I when reheating to room temperature, see section 4.1.

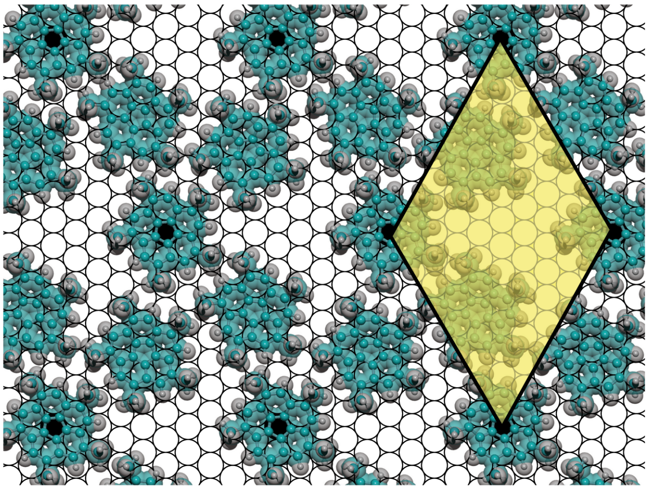

Fig. 3.16 Structural model of the $\begin{pmatrix} 10 & 5 \\ -5 & 5 \end{pmatrix}$ "hole phase" structure. The empty areas in this model correspond to the dark areas in the STM image 3.15

Figure 3.17 displays a self-correlation processed STM image and a low-pass filtered image of the hole phase. Both methods underline the fact, that in each unit cell one of the three molecules is significantly elevated compared to its neighbors. Line-scans on the STM images could only support this hypothesis in approximately 80% of the molecules. An artefact due to the scanning direction would be unlikely, since measurements with different scanning directions were conducted.

Although the stacking theory is intriguing, the reason why one in three molecules appears elevated is still unclear. Possible explanations might be a different adsorption site on the substrate, an elevation induced by its neighboring molecules lifting it from the surface or a bowl-in-bowl stacking of two molecules. Fact is, that if four (three in the first layer, one in the second) molecules instead of three are present in the unit cell, the density of the structure $\begin{pmatrix} 10 & 5 \\ -5 & 5 \end{pmatrix}$ becomes 0.053, a deviation of only 6 % from the room temperature structure $\begin{pmatrix} 10 & 3 \\ -3 & 7 \end{pmatrix}$.

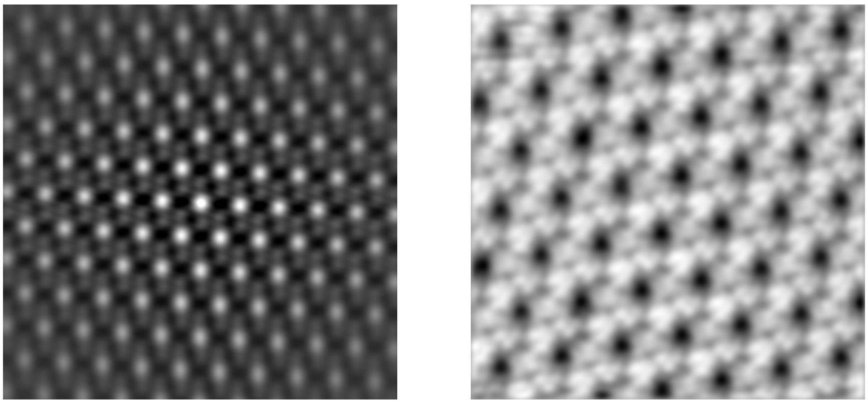

Fig. 3.17 Left: self-correlation image of the STM image in 3.15. Right: STM image 14 nm x 14 nm, low-pass filtered, −1.028 V, 494 pA.

3.3.1 High Temperature 4x4 Phase

Pentamethyl-corannulene was deposited to one monolayer coverage on the copper substrate held at approximately 660 K[b]. TPD measurements for 1 ML Me_5COR showed the release of hydrogen in Figure 3.2, so hydrogen release is expected under this preparation condition. The goal of this experiment was to modify the surface with Me_5COR such that concave side would point towards the surface due to covalent bonds formed between the methyl groups and the surface.

A new structure proved to be extremely stable under the STM tip, unlike corannulene or Me_5COR deposited at room temperature. From the STM images the unit cell of the structure was identified as a (4x4) superstructure just like corannulene and C_{60} at room temperature on Cu(111). Tentative models with Me_5COR strongly indicate, that Me_5COR is too big in order to assemble in a (4x4) unit cell. The steric hinderance of the methyl groups prohibits dense packing of a (4x4) structure. Also vacancies in the monolayer as seen in the STM image in Figure 3.18 were very stable and did change little over time. Individual hopping of vacancies could be monitored. No vacancies could usually be imaged in a room temperature COR (4x4) monolayer, most probably because the molecules have too high mobility to be imaged in low density areas.

Measurements at different temperatures were conducted to check wether the structure undergoes any phase transition, as would be expected for a pure COR adlayer. No transitions were observed. This strongly indicates, that the imaged molecules are in fact not COR.

---

[b] Temperature measurement on the manipulator was not directly at the sample, but on the manipulator close to the sample holder. The value is accurate within ±20 K.

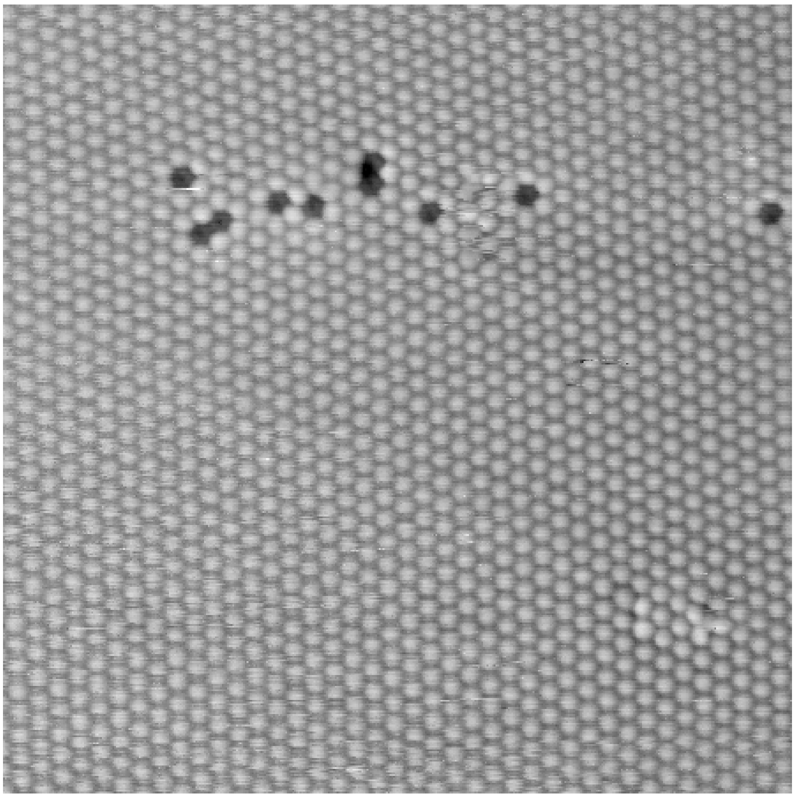

Fig. 3.18 STM image 35 nm x 35 nm, −1.235 V, 336 pA, RT. It shows the Me$_5$COR (4x4) structure with vacancies.

The close up in Figure 3.19 shows the topographic appearance of the molecules under STM. Rather than showing the tilted doughnut shape like corannulene on Cu(111), they present themselves in a circular form.

For further analysis STM images were low-pass filtered. The high resolution image left in Figure 3.20 shows submolecular features, that differ from the 4x4 structure from corannulene on Cu(111). The molecule is not tilted to one side, but looks symmetric around its central axis, with an indentation in the center. A very similar sub-molecular structure was found by K. Motai and coworkers in 1993 with C_{60} on Cu(111) [17], although at a different bias voltage. They imaged C_{60} at different biases and were able to resolve sub-molecular features on the buckyball. Their image in Figure 3.20 shows the curved surfaces of buckyballs with their central five-membered rings. Disregarding the rest of C_{60}, they imaged basically the topography of corannulene with its bowl-opening pointing towards the substrate.

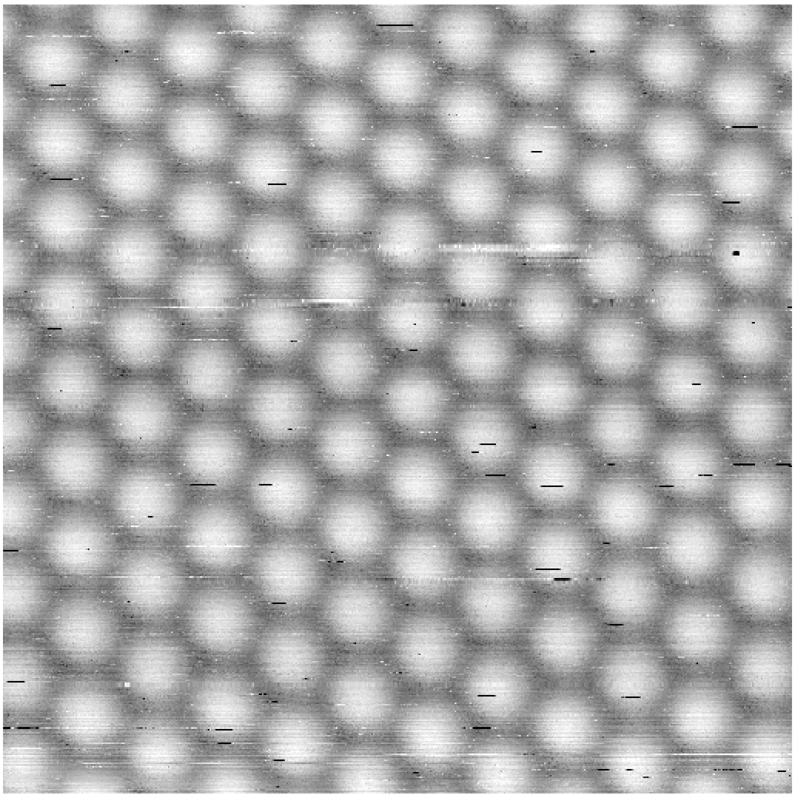

Fig. 3.19 Me_5COR 4x4 lattice on Cu(111). STM image 10 nm x 10 nm, room temperature. The individual molecule looks similar to images from the $\left(\begin{smallmatrix}10 & 3\\ -3 & 7\end{smallmatrix}\right)$ high density Me_5COR structure.

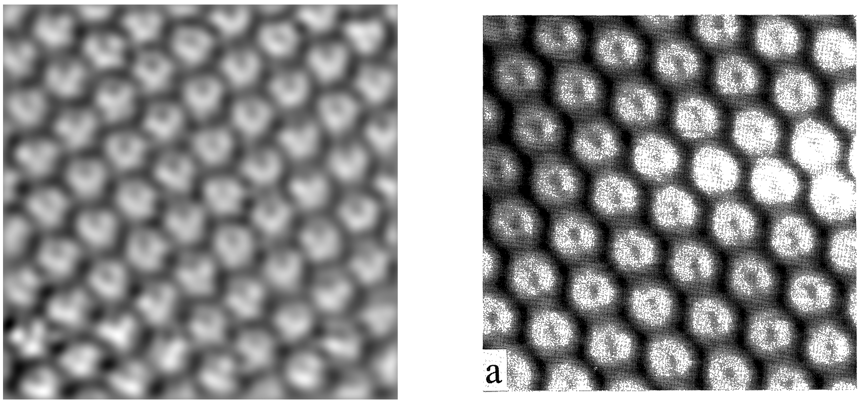

Fig. 3.20 Me_5COR 4x4 lattice on Cu(111). Left: STM image 7.7 nm x 7.7 nm, RT, low-pass filtered, −0.685 V, 581 pA. The indentation in the center of the molecule is clearly visible. Right: High resolution STM images of a C_{60} monolayer on Cu(111) taken at bias voltage −2.0 V. Size: 6.4 nm x 6.4 nm. Reprinted figure with permission from [17]. Copyright (1993) by Japan Society of Applied Physics.

From the measurements, simulations and models of fullerenes on Cu(111) from [17, 84] and others, it is one possibility to interpret our findings as a Me$_5$COR molecule with its concave side pointing towards the surface.
The following list denominates indications, that support this hypothesis.

- The molecules form a lattice, that is unprecedented and too small for the intact molecule with five methyl groups on the rim.
- The 4x4 monolayer is extremely stable under the STM tip. The molecular mobility on the copper substrate is clearly diminished compared to the adlayers of COR and Me$_5$COR that were deposited at room temperature.
- The sub-molecular features found with high resolution STM resemble the features of C$_{60}$ on Cu(111), indicating that the molecule is not tilted and the molecular bowl opening is pointing towards the surface, a conformation that was not found for corannulene or any derivative in physisorbed layers.

There are however other explanations on how this structure occurs. Otero and coworkers published in 2008 the synthesis of C$_{60}$ from precursor molecules on a Pt(111) surface [85]. Surface supported synthesis of C$_{60}$ from Me$_5$COR on our Cu(111) substrate is a possible explanation to the formation of the observed 4x4 structure, although the relatively low temperature and the lack of highly reactive sidegroups are indications, that another explanation is more likely.
Another possibility is the formation of carbon single bonds (C-C) between the corannulene bowls. The methyl groups and possibly part of the native hydrogens on the corannulene rim are released and the dangling bonds of neighboring molecules form a molecular network on the basis of the COR 4x4 adlayer lattice. In this case the concave side of the molecules would still point away from the surface, tilting however would be frustrated. This possibility, however, is unlikely due to the described mobility of the vacancies.

3.3.2 2nd layer growth at low temperature

By depositing additional molecules on top of a monolayer at temperatures around 50 K, the formation of a second layer could be imaged with STM. Also at this low temperature the second layer proved to be highly mobile as can be seen from the STM images in Figure 3.21. The second layer is bowl-in-bowl stacked on top of the first layer molecules, assembled in the same $\left(\begin{smallmatrix}10 & 3\\ -3 & 7\end{smallmatrix}\right)$ structure. Due to the high mobility, the azimuthal orientation of individual molecules could not be determined. The rotation around the molecular central axis gives the molecules a roundish appearance much like the monolayer at room temperature.

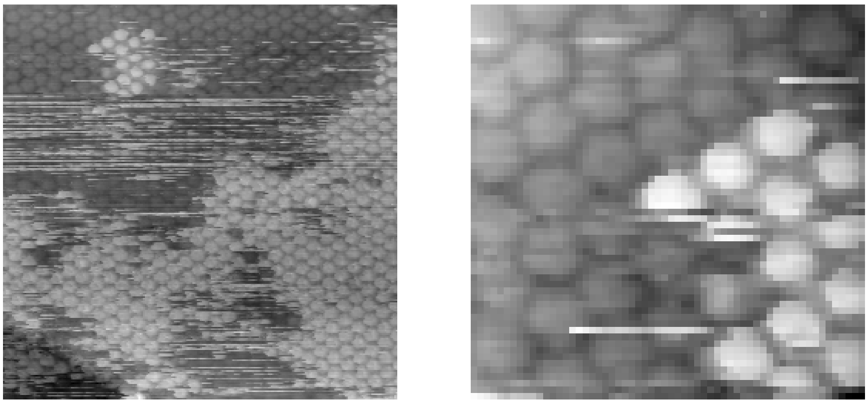

Fig. 3.21 Left: STM image of second layer formation on top of the regular $\left(\begin{smallmatrix}10 & 3\\ -3 & 7\end{smallmatrix}\right)$ at 50 K. 30 nm x 30 nm, −1.608 V, 83 pA. Right: Same at 7 nm x 7 nm, −1.608 V, 83 pA.

3.4 Conclusions

Fivefold symmetry in molecular geometry is unfavorable in two-dimensional self-assembly, same as it is in macroscopic packing. Tessellations of the plane are impossible without overlap or gaps between the molecules. Self-assembly experiments with corannulene and its derivatives demonstrate that the packing problem is the same in molecular dimensions as it is for macroscopic rigid pentagons.

Different mechanisms are exploited in molecular self-assembly to bypass fivefold symmetry in order to achieve a more favorable geometry, which enables the layer to arrange in a quasi-hexagonal or other long range supporting order. The mechanisms include molecular tilting. Due to the tilting, the molecular symmetry as perceived by its neighbors changes and the molecules assemble in a quasi-hexagonal lattice.

Substituents on the rim of a corannulene molecule provide steric hinderance that avoids tilting of the bowl. Therefore pentamethyl- and pentachloro-corannulene can not bypass the fivefold molecular symmetry and assemble according to pentagon dense packing motifs as found by shaking table experiments and Monte-Carlo simulations with macroscopic rigid pentagons. Two phases with different densities are formed for Me_5COR: the less dense rotator phase and the denser striped phase, also observed for Cl_5COR. From analogy between the pentagon packing problem and molecular self-assembly can be deduced that rigid tiles ordering can be a valid approximation for molecular self-assembly.

Chapter 4

Self-Assembly of Corannulene

The self-assembly behavior of corannulene was previously analyzed with STM on the Cu(110) [46] and Cu(111) [50, 86] surfaces in our group before the begin of this project. In the course of this thesis, additional studies have been performed on the system of COR/Cu(111). XPS and TPD measurements were conducted for further characterization of COR on Cu(111) and LEED measurements were conducted to scrutinize previous findings with different methods.

The growth of the COR monolayer was monitored using work function change measurement by UPS at room temperature and XPS was used to determine the absolute coverage of the COR / Cu(111) system, for comparison to our earlier data based on calibrations made for C_{60} on Cu(111) via the comparison of the C 1s and Cu 3s peak area.

One monolayer of COR on Cu(111) results in a C 1s to Cu 3s ratio of 0.243. This corresponds perfectly to the value of the C 1s to Cu 3s ratio for C_{60} of 0.672. One molecule of corannulene has one third of the carbon atoms of a C_{60} molecule. Since they both self-assemble in a 4x4 superstructure on the Cu(111) substrate, the C 1s to Cu 3s ratio of C_{60} can be simply divided by three. The comparison of the C_{60} ratio divided by three and the COR ratio leads to a ratio of 1 : 1.08. The excess of 8 % is thought to be due to mobile second layer molecules or small three-dimensional islands of corannulene.

Temperature programmed desorption (TPD) measurements were conducted to investigate the desorption of multilayers of corannulene from the substrate and also the decomposition of the molecule. Figure 4.1 shows the thermally induced desorption of the COR multilayers and the second layer. The three spectra shown in the graph correspond to 2 ML, 2.3 ML and 3 ML by XPS measurement on the C 1s and

Cu 2p peaks. The areas of the desorption peaks correspond to 1 ML, 1, 5 ML and 2, 1 ML in very good agreement to the photoemission measurements, considering that the first layer is not desorbing without decomposition and only the second and third layer are contributing to the peak areas. The two distinct peaks that can be seen for coverages above two monolayer show that the multilayer desorbs approximately 25 K (302 K absolute) before the second layer at 328 K.
As observed for COR on Cu(110) [46], the first layer does not desorb, but decomposes at 570 K, visible in the desorption peak of hydrogen (Figure 4.2).

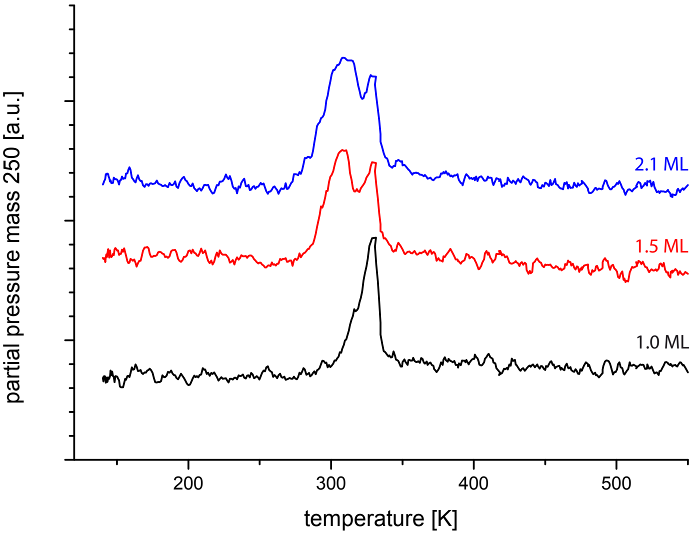

Fig. 4.1 Temperature programmed desorption measurement of corannulene at mass 250. Black: 1 monolayer, red: 1.5 monolayer, blue: 2.1 monolayer. This data is also backed up by XPS, which gives the coverages as 2 ML (red), 2.5 ML (blue) and 3 ML (black), which also counts for the first layer, that does not show up in TPD at mass 250.

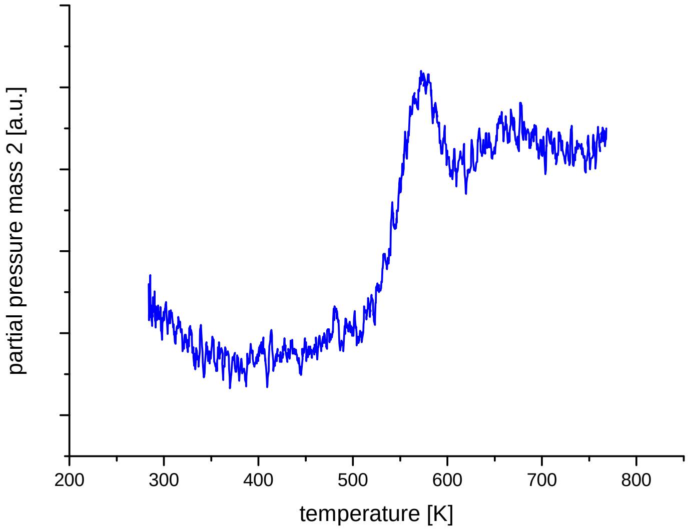

Fig. 4.2 TPD measurement on the decomposition of 1 ML corannulene at mass 2.

4.0.1 LEED

The COR / Cu(111) phases found by STM were confirmed with LEED. This procedure was of importance in order to characterize this system with this method for additional experiments only using LEED.

Figures 4.3 shows the LEED pattern for the room temperature phase I of COR / Cu(111). The structure is a (4x4) superstructure. The adlayer is not very stable under the electron beam at energies needed to see the copper reflexes.

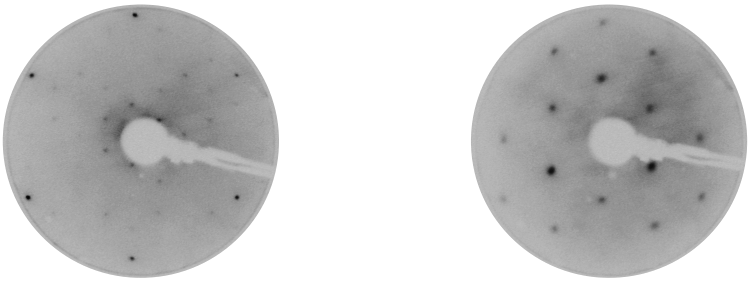

Fig. 4.3 LEED pattern of the $\begin{pmatrix}4 & 0\\0 & 4\end{pmatrix}$ room temperature COR phase taken at 58 eV (left) and 15 eV (right).

Due to the tilt angle of the molecules in the 4x4 structure, there are three rotational domains.

Figure 4.4 shows a LEED pattern of phase II together with the LEEDPat simulation of all the sub-domains of the structure $\left(\begin{smallmatrix}4&0\\3&7\end{smallmatrix}\right)$. Three rotational domains for both mirror alignments are superimposed. All sub-domains were found with STM as well.
The characteristic feature of the LEED pattern at 15 eV is six quadruplets surrounding the zero-order reflex arranged along the copper directions, see Figure 4.4 (bottom). This feature especially helps to distinguish phase II from phase III.

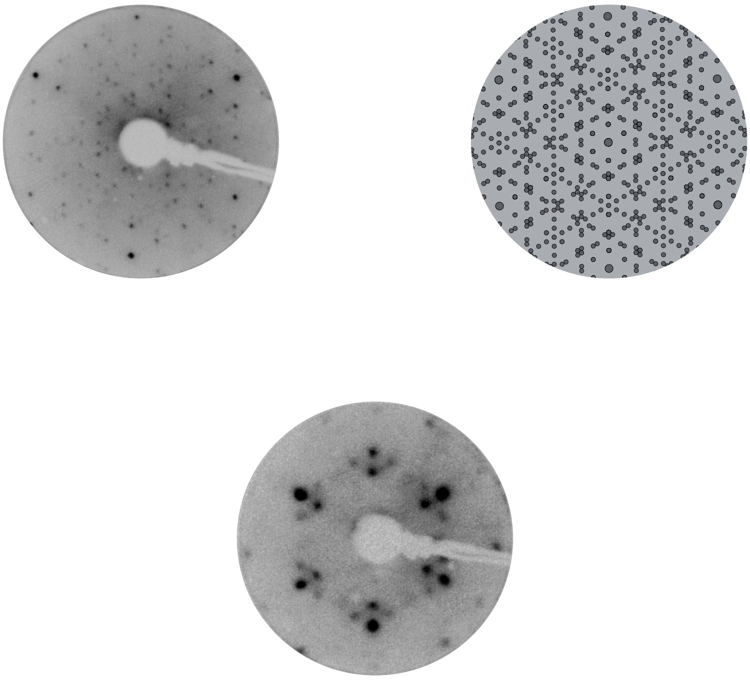

Fig. 4.4 Top: LEED pattern of the $\left(\begin{smallmatrix}4&0\\3&7\end{smallmatrix}\right)$ Phase II structure taken at 75 eV and 250 K with its LEEDPat simulation. Bottom: Same structure taken at 14 eV and 250 K, with the characteristic quadruplets.

Figure 4.5 shows the LEED pattern for the 100 K $\left(\begin{smallmatrix}4&2\\0&7\end{smallmatrix}\right)$ structure (phase III) with the corresponding LEEDPat simulation. This structure also consists of six domains: three rotational domains each with its corresponding mirror domain.
The characteristic feature of this structure at 15 eV is six triplets around the zero order reflex between the copper directions. A sample showing the characteristic triplets is shown in Figure 4.5 (bottom).

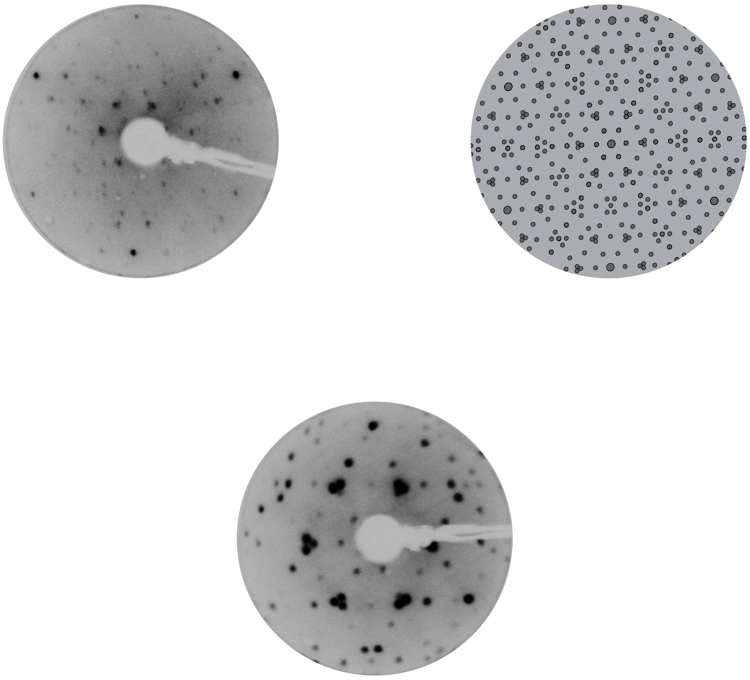

Fig. 4.5 Top: LEED pattern of the COR $\begin{pmatrix}4&2\\0&7\end{pmatrix}$ stripes structure (Phase III) taken at 75 eV and liquid nitrogen temperature (LNT) and the corresponding LEEDPat simulation. Bottom: LEED pattern of the same structure taken at 14 eV and LNT, showing the characteristic triplets.

To summarize the three main phases of corannulene the following table 4.1 gives an overview on the matrices, the STM images with the unit cells and the LEED patterns.

Table 4.1 Overview on the three main COR phases.

Phase	Temperature	Structure	STM (5 x 5 nm)	LEED (14 eV)
I	room temperature	$\begin{pmatrix} 4 & 0 \\ 0 & 4 \end{pmatrix}$	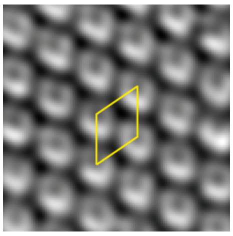	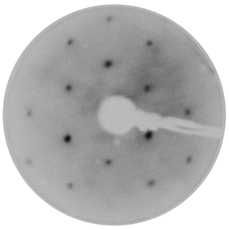
II	200 – 250 K	$\begin{pmatrix} 4 & 0 \\ 3 & 7 \end{pmatrix}$	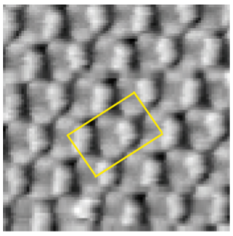	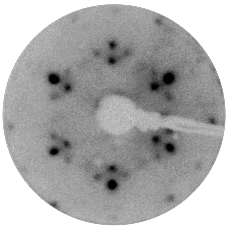
III	below 200 K	$\begin{pmatrix} 4 & 2 \\ 0 & 7 \end{pmatrix}$	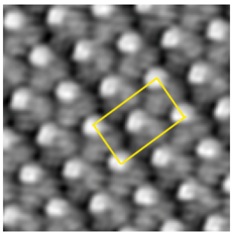	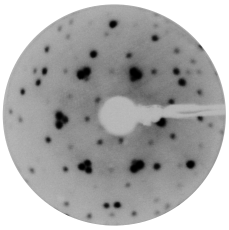

4.0.2 2nd layer growth at low temperature

By depositing corannulene on top of a close packed monolayer at low temperature, second layer growth is induced. The molecules of the second layer were found to be very mobile. Molecules at the edge of second layer islands constantly detach and attach. The islands themselves were stable and did not change their size over several hours. Figure 4.6 shows STM images of the second layer islands at 50 K. It also shows that the second layer molecules sit on top of the first layer molecules, forming the same $\begin{pmatrix} 4 & 2 \\ 0 & 7 \end{pmatrix}$ structure as the first layer. Since the first layer molecules are substantially tilted to one side, this might indicate that the second layer is tilted as well in order to maintain the same structure. However, this could not be confirmed with STM, due to limited resolution in this agile layer. Hence, we do not exclude the possibility of a rearrangement of the first layer due to second layer adsorption. A bowl-in-bowl stacking seems then to be a reasonable structure motif.

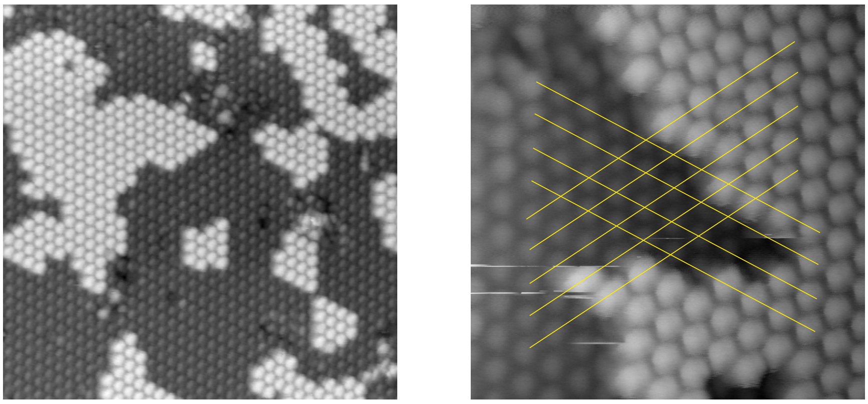

Fig. 4.6 Partial double layer of COR at low temperature. Left: STM image 28 nm x 28 nm, −1.744 V, 24 pA. Right: STM image 10 nm x 10 nm, −1.744 V, 24 pA. The lines indicate the directions of densest packing in the first layer. The second layer molecules sit on top of the first layer molecules, not in a bridge position or threefold hollow site.

4.1 Selecting a Polymorph

We recall that the high-temperature phase transition is accompanied by a contraction of the lattice and formation of low-density areas. Deposition of additional molecules within the stable temperature range of phase II leads to growth of phase II at the expense of the 2D gas (a highly disordered area, accompanying phases II and III) until the whole surface is covered with that phase. Since the two phases exist at a dynamic equilibrium, an increase in the overall density of molecules on the substrate favors the denser phase. If the 14 % contraction of the phase transition is compensated by depositing another 14 %, the whole substrate is covered with a continuous layer of phase II. Upon cooling, the normal phase transition from phase II to III does not occur and phase II is stabilized. [86]

Subsequent heating of the stabilized phase II eventually leads to the formation of the room temperature phase I and to desorption of excess molecules. The cycle is restored and can be restarted (see Figure 4.7). However the confinement of molecules in phase II not only leads to a stabilization at lower temperatures. Substantial superheating is required too to create phase I again.

To deposit exactly 14 % of a monolayer onto a crystal held within a temperature range where multiple phases do exist can be difficult due to the hysteresis in transitions. If not enough molecules are deposited to fill the whole area of the 2D gas, some areas of the crystal will undergo the phase transition when cooled, while others are stabilized. This leads to coexistence of phase II and III at low temperatures, see Figure 4.8.

The same happens if due to slight supercooling before the additional deposition nuclei of phase III were formed. On any terrace that is "infected" with phase III, the low temperature phase will dominate in the end. Phase II can only be stabilized if the domain is pure.

These observations lead to the following interpretations based on the qualitative thermodynamic diagram in Figure 4.9. The enthalpically favored phase III is formed under normal conditions after slight supercooling of phase II. The supercooling is necessary due to the kinetic barrier of the transition. The enthalpy difference is thought to be small due to the equal density of the phases [87]. Due to entropic contributions resulting from low-frequency bowl vibrations the Gibbs enthalpy curves of phase II and III cross at T_{eq2-3}, indicating the equilibrium temperature between the phases II and III. As mentioned earlier the transitions need slight supercooling and -heating to occur. This is visible in the hysteresis range between T_{t2-3} and T_{t3-2}. Since the step from the enthalpy curve of II to III is corresponding to the kinetic barrier, this means that an increase in the kinetic barrier will shift the transition temperature to lower temperatures, i.e. the meta-stable phase II can be selected at a given temperature.

The kinetic barrier is controllable through the low-density areas on the crystal. Since phases II and III have identical densities, they need additional space to move in the layer. Without the extra space, the rearrangement would cause molecules to overlap during the transition.

There is another interpretation of the microscopic mechanism. Due to the equilibrium of phase II and the 2D gas, the growth of the new phase III is thought to nucleate at the dynamic interface of phase II and 2D gas. Without the low density area present, there is no favorable nucleation site and the transition is inhibited.

The selection of phase II at lower temperatures is not depending on the growth of a completely covering phase II layer. As experiments with other molecules showed, the mere filling of the low density area or 2D gas provides a kinetic barrier high enough to stabilize phase II. We successfully stabilized phase II with additional deposition of the following molecules.

- Corannulene
- Pentamethyl-corannulene[a]
- [7]-Helicene, enantiopure and racemic mixture[a]
- tartaric acid, enantiopure and racemic mixture

The variety of these molecules with different functional groups and especially their different sizes shows, that the stabilization of a corannulene phase is only based on the solidification of the 2D gas. Be it to crystalize to an already existing phase II domain with additional corannulene, or to a solid solution of corannulene with larger (Me_5COR, Helicene) or smaller (tartaric acid) molecules. The immobilization of the 2D gas is the key to select a polymorph.

The selection of a polymorph does not only work in one direction. The detailed explanation of the stabilization of phase II into the stable temperature region of phase III is a nice example to explain the process. The stabilization of phase III to

---

[a] LEED patterns of the [7]-Helicene- and Me_5COR-stabilized corannulene phase II can be found in the appendix.

higher temperatures works as well, due to the same reason of increasing the kinetic barrier by filling the 2D gas areas. However, the stabilization is only into the stable temperature range of phase II. As soon as phase I is being formed, the excess molecules are pushed from the layer and probably desorbed.

A similar effect on glycine crystals on nano-pores has been reported in [88]. Depending on the size of the nano-pores the phase transition to the more stable α phase could be suppressed.

The described example for two-dimensional polymorph selection can therefore be a starting point for future studies of three-dimensional crystallization.

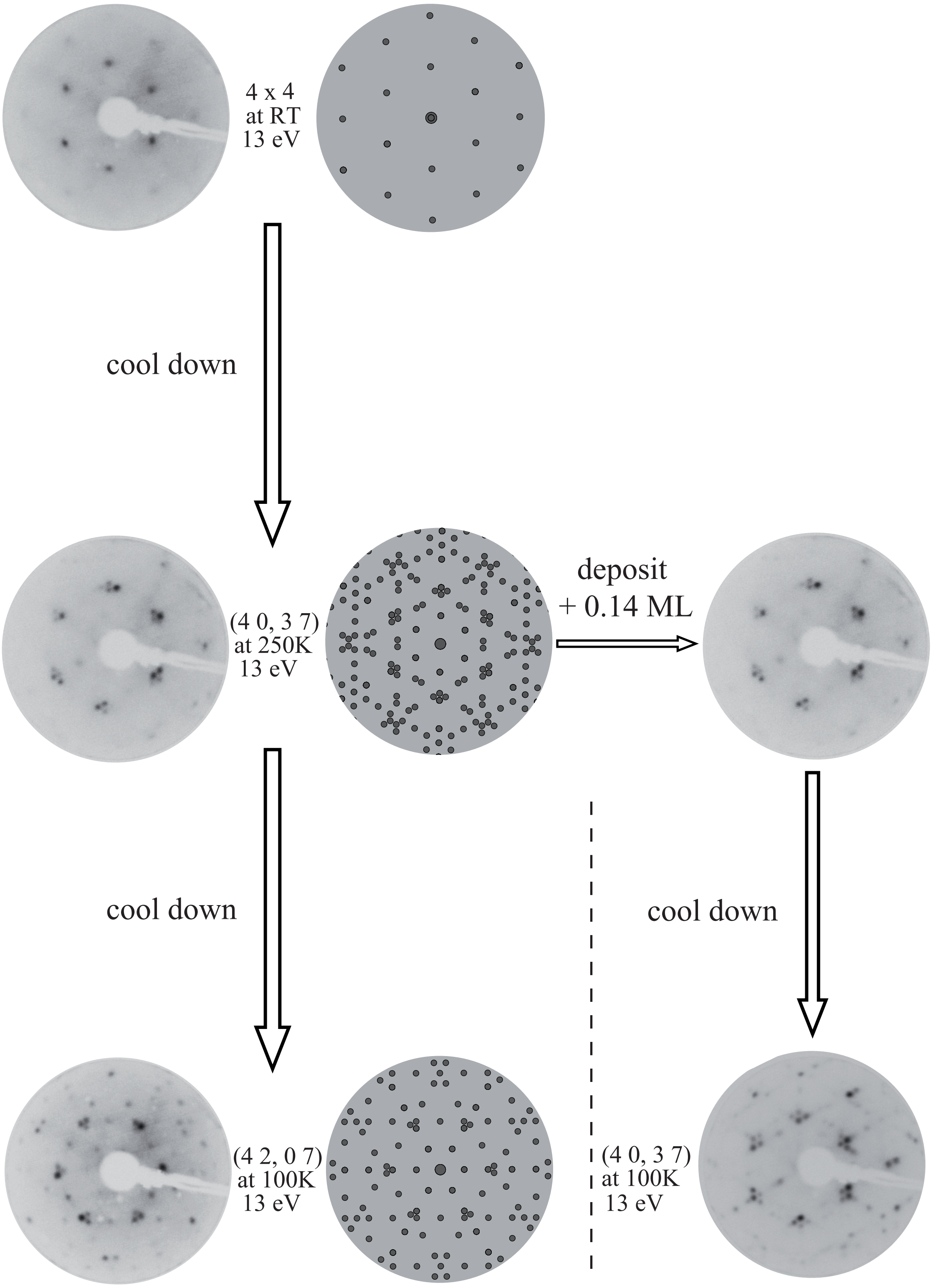

Fig. 4.7 The process of selecting a polymorph for corannulene. At room temperature corannulene orders in a 4x4 structure (phase I). When cooled down to under 250 K the 14.3 % denser phase II $\left(\begin{smallmatrix}4&0\\3&7\end{smallmatrix}\right)$ is formed. Upon further cooling under 210 K, the low temperature phase $\left(\begin{smallmatrix}4&2\\0&7\end{smallmatrix}\right)$, phase III, stabilizes. Confining phase II, by additional deposition of molecules, prevents the formation of phase III, resulting in a stabilized phase II at 90 K.

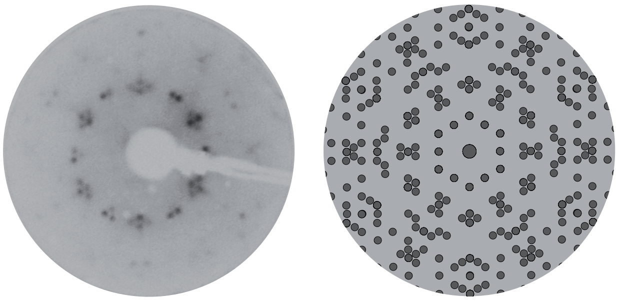

Fig. 4.8 LEED pattern of the coexistence of phase II, $\left(\begin{smallmatrix}4&0\\3&7\end{smallmatrix}\right)$, and phase III, $\left(\begin{smallmatrix}4&2\\0&7\end{smallmatrix}\right)$. If phase II is only partially stabilized, e.g. the disordered space apart from phase II is not fully covered by additionally deposited molecules, some domains undergo the phase transition and both phases coexist on the substrate.

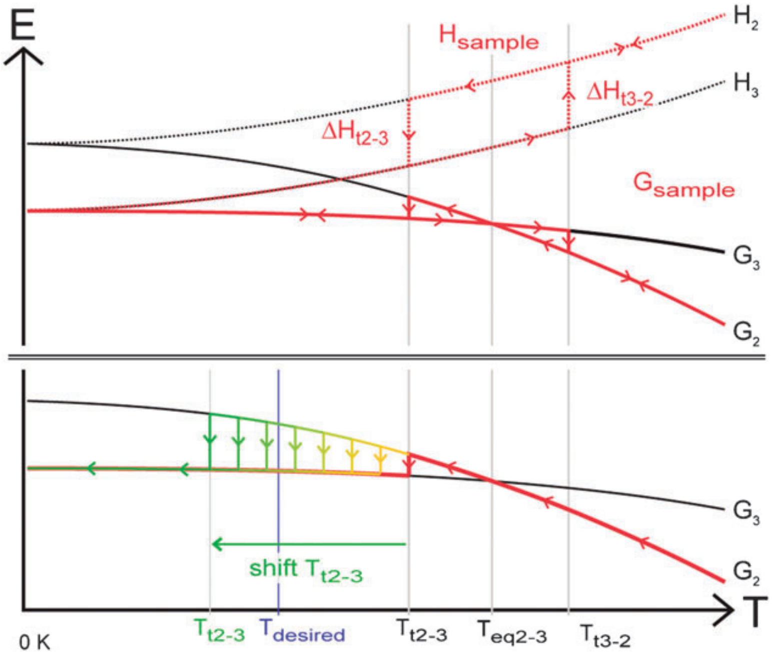

Fig. 4.9 Qualitative energy-temperature diagram for the transition between phase II and III (top). The transitions show a hysteresis in temperature due to a kinetic transition barrier. In order to select phase II at the desired temperature (blue line), the kinetic energy barrier has to be increased, causing a shift of T_{t2-3} (orange to green) below $T_{desired}$. By selectively switching the additional barrier on or off, the polymorph at $T_{desired}$ can be selected to be either II or III. Reprinted with permission of The Royal Society of Chemistry from [86].

4.2 Suppression of Mirror Domains

In the course of trying to stabilize polymorph II of the corannulene system with different molecules, doping experiments with tartaric acid have been performed as well. The hypothesis was, that if the $\left(\begin{smallmatrix}4&0\\0&4\end{smallmatrix}\right)$ room temperature phase was seeded with a small amount of a chiral molecule, the transition from phase I to phase II would favor three rotational domains over their three mirror domains. The experiments were conducted using enantiopure and racemic [7]-Helicene and enantiopure and racemic tartaric acid. The doping with Helicenes showed no effect besides the stabilization described in the previous section. The results from the experiments with tartaric acid are shown in this section.

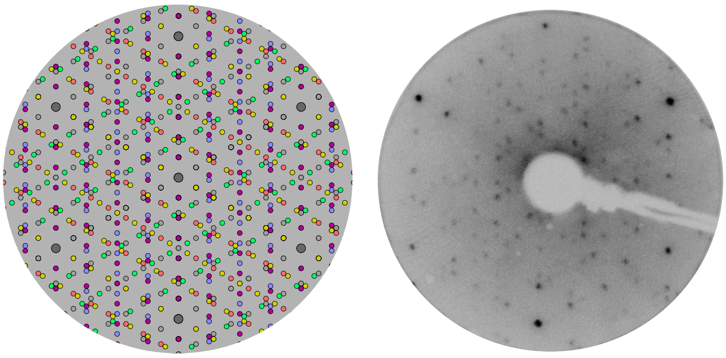

Fig. 4.10 left: LEEDPat simulation of the $\left(\begin{smallmatrix}4&0\\3&7\end{smallmatrix}\right)$ phase, every one of the six subdomains in a different color. right: LEED pattern of pure corannulene $\left(\begin{smallmatrix}4&0\\3&7\end{smallmatrix}\right)$ phase, taken at 75 eV.

Figure 4.10 shows the unmodified $\left(\begin{smallmatrix}4&0\\3&7\end{smallmatrix}\right)$ phase II of corannulene. The LEED pattern we see is a superposition of six independent sub-domains included in the $\left(\begin{smallmatrix}4&0\\3&7\end{smallmatrix}\right)$ master matrix. Three of the sub-domains are theoretically created by rotating the $\left(\begin{smallmatrix}4&0\\3&7\end{smallmatrix}\right)$ domain by 120°. The other three domains result from the mirror projection of the three rotational domains at one of the dense packed copper directions.
The seeding with racemic tartaric acid (TA) showed no effect at all, except for the stabilization of phase II when cooled down. This is not entirely surprising, since the two enantiomers D-TA and L-TA are included in the racemic mixture 1 : 1. Their individual effects on the corannulene monolayer might cancel each other out, or they might be adsorbed as heterochiral pairs and do not impose any chiral influence on the COR lattice.

When doped with approximately 0.05 ML[b] of enantiopure D-TA or L-TA three mirror domains in the $\left(\begin{smallmatrix}4&0\\3&7\end{smallmatrix}\right)$ phase were suppressed and the remaining three could be stabilized to low temperatures. The suppression and stabilization was measured with LEED and the domain size was found to be large enough to measure single domains. Figure 4.11 shows the L-TA doped single domain $\left(\begin{smallmatrix}4&0\\3&7\end{smallmatrix}\right)$, which is the mirror domain of the D-TA doped $\left(\begin{smallmatrix}4&0\\4&7\end{smallmatrix}\right)$ domain, shown in Figure 4.12. These two LEED patterns represent the two mirror groups of each three rotational domains.

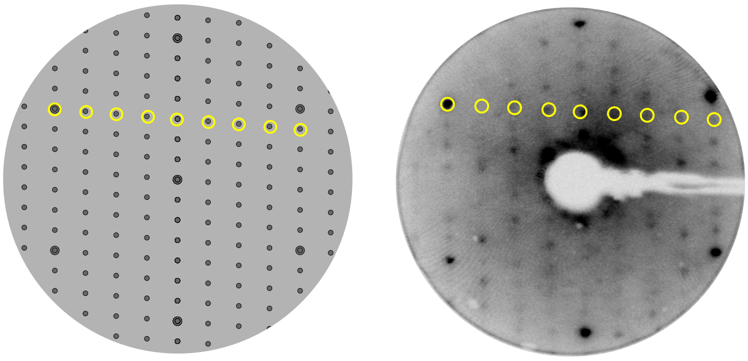

Fig. 4.11 left: LEEDPat simulation of the $\left(\begin{smallmatrix}4&0\\3&7\end{smallmatrix}\right)$ domain of the $\left(\begin{smallmatrix}4&0\\3&7\end{smallmatrix}\right)$ phase. right: LEED pattern of the L-TA doted and stabilized $\left(\begin{smallmatrix}4&0\\3&7\end{smallmatrix}\right)$ phase of corannulene, resulting in a suppression of all domains except one.

Unfortunately there are no high resolution STM images showing where the TA molecules adsorb beside the corannulene covered substrate. Figure 4.13 shows an STM image of the stabilized $\left(\begin{smallmatrix}4&0\\3&7\end{smallmatrix}\right)$ phase at 56 K. The phase looks no different than all other measurements on the pure phase taken between 200 and 250 K. There is no indication, where the TA molecules might be incorporated in the layer.

There are basically two possibilities on the position of the TA molecules in the COR adlayer. Either the molecules are adsorbed at a copper step edge and modify the step edge in a way that favors one of the mirror domains during the phase transition, or the molecules adsorb into the corannulene monolayer at the onset of the phase transition, where they impose the chiral bias at domain boundaries.

---

[b] This is a very rough estimate. The shutter for the evaporation cell was opened for only 10 s.

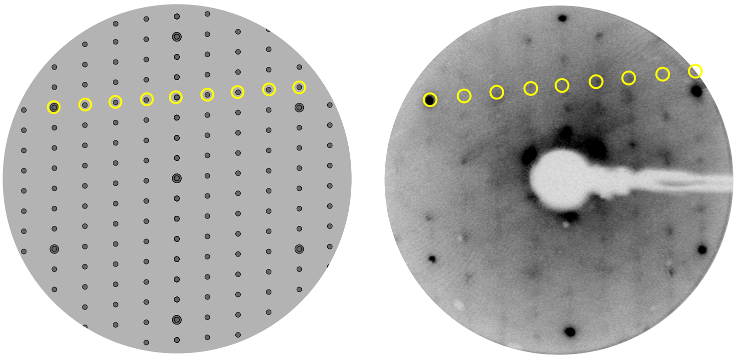

Fig. 4.12 left: LEEDPat simulation of the $\left(\begin{smallmatrix}4&0\\4&7\end{smallmatrix}\right)$ domain of the $\left(\begin{smallmatrix}4&0\\3&7\end{smallmatrix}\right)$ phase. right: LEED pattern of the D-TA doted and stabilized $\left(\begin{smallmatrix}4&0\\3&7\end{smallmatrix}\right)$ phase of corannulene, resulting in a suppression of all domains except one.

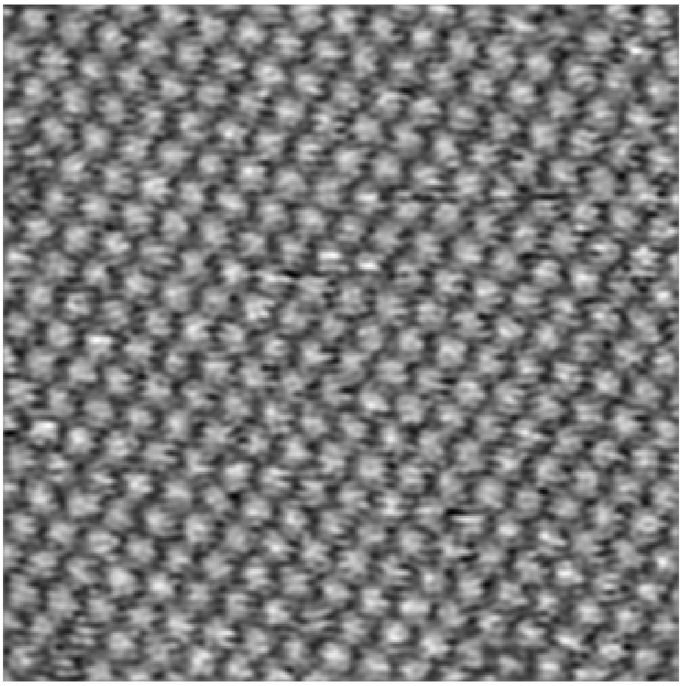

Fig. 4.13 STM image of the D-TA stabilized COR phase II on Cu(111) taken at 56 K in the supercooled state. 25 x 25 nm, −1.452 V, 233 pA, filtered.

4.3 Tartaric Acid / Cu(111)

Our doping experiments suggested to study the pure TA system. Either in order to exclude that any observation were exclusively due to TA structures or just for curiosity if TA forms a 2D conglomerate like on Cu(110). A series of experiments to characterize the tartaric acid / Cu(111) system, including both enantiomorphs and the racemic mixture was conducted[c] to compare with results from the stabilization experiments in 4.2.

The tartaric acid system on Cu(110) is one of the most investigated systems in chiral surface science [89–94]. The interested reader is referred to the reviews of C. J. Baddeley and M. Studer [95, 96].

The first question for this system is whether the molecule is bound with both carboxylic groups or — due to lateral interaction — with only one carboxylic group (Fig. 4.14). To exactly pin down the structure it is important to determine the coverage accurately.

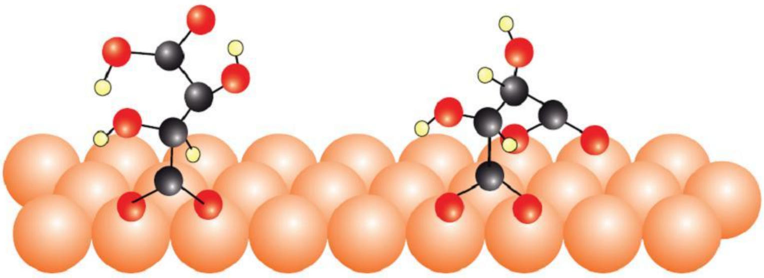

Fig. 4.14 Two binding modes of tartaric acid on Cu(111). With monotartrate (left) only one carboxyl group is deprotonated, having four distinguishable carbon atoms, while bitartrate (right) has both groups bound to the surface, leading to a pair of identical carbon atoms. The surface science nomenclature introduced by Barlow and Raval [97] for tartaric acid contradicts the common usage of bi- for monosubstituted divalent acids (e.g. sodium bicarbonate, $NaHCO_3$).

Tartaric acid was deposited by sublimation in UHV onto a Cu(111) crystal and investigated by XPS and LEED. All structures presented in this part were deposited until saturation of the layer was achieved and confirmed by XPS via the intensities of the C 1s, O 1s and Cu 2p peaks (Figure 4.15).

[c] The experiments on the self-assembly of tartaric acid on Cu(111) were conducted by Cedric Sax, a master student, under supervision of the author.

The saturated coverage θ for L-tartaric acid and racemic tartaric acid were both found to be 0.33 (being the ratio of the C 1s and Cu 2p peaks, corrected by the atomic sensitivity factor). D-tartaric acid was not measured with the same precision in XPS, but directly investigated with LEED, relying on the XPS data for L-tartaric acid.

The ratio of the C 1s and O 1s peaks was monitored as well to ensure that molecules covering the substrate truly were tartaric acid. The expected values for the C 1s / O 1s ratio was 0.67 for any coverage. This value were calculated from six oxygen atoms and four carbon atoms per molecule. The overall statistics for all XPS measurements on tartaric acid provided a mean value of 0.61 and a standard deviation of 0.1.

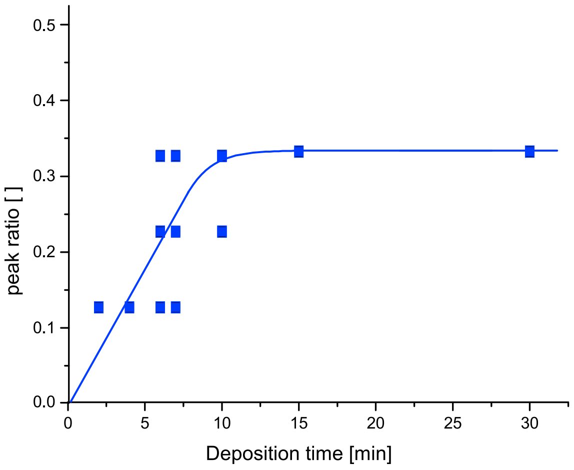

Fig. 4.15 Deposition of racemic tartaric acid on Cu(111) measured by XPS. Ratio for C 1s peak over Cu 2p peak against deposition time.

Tartaric acid on Cu(111) was investigated before in aqueous solution [98]. The paper reported both enantiomers forming a (4 x 4) structure, built-up by heterochiral dimers. Similar structures are expected to form under UHV conditions.

To achieve chemisorbed binding of tartaric acid to the copper substrate in UHV an annealing step is often necessary [89, 93, 94]. After deposition at room temperature no LEED pattern was detected. After annealing the D- and L-tartaric acid saturated monolayers at 80 °C for at least 10 minutes, ordered and very stable superstructures were found, see Figure 4.16 and 4.17. The two structures were identified as $\left(\begin{smallmatrix}10 & 3\\ -3 & 7\end{smallmatrix}\right)$ for L-tartaric acid and $\left(\begin{smallmatrix}7 & -3\\ 3 & 10\end{smallmatrix}\right)$ for D-tartaric acid, being a mirror domain of the $\left(\begin{smallmatrix}10 & 3\\ -3 & 7\end{smallmatrix}\right)$ structure. We conclude, that the chirality of the enantiomer has been transferred into the long-range ordered two-dimensional crystal.

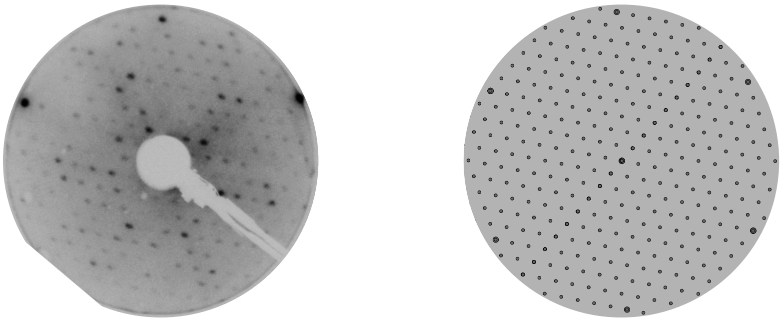

Fig. 4.16 LEED pattern (left) of the $\left(\begin{smallmatrix}7 & -3\\ 3 & 10\end{smallmatrix}\right)$ structure found for D-tartaric acid on Cu(111) and a simulated LEED pattern (right) of the same structure.

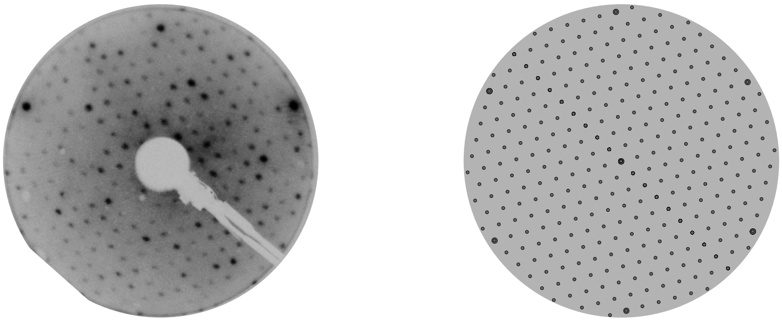

Fig. 4.17 LEED pattern (left) of the $\left(\begin{smallmatrix}10 & 3\\ -3 & 7\end{smallmatrix}\right)$ structure found for L-tartaric acid on Cu(111) and a simulated LEED pattern (right) of the same structure.

Tentative models for the two mirror structures $\left(\begin{smallmatrix}10 & 3\\ -3 & 7\end{smallmatrix}\right)$ and $\left(\begin{smallmatrix}7 & -3\\ 3 & 10\end{smallmatrix}\right)$ are given in Figure 4.18. The models are based on the assumption that the enantiopure molecules assemble in dimers in the large unit cells. Each cell contains eight molecules in four dimers. The orientation of the dimers is purely arbitrary and it is clear that there have to be three rotational sub-domains, with orientations of the dimers that are rotated 120 °. Based on comparison with XPS data for TA on Cu(110) and the

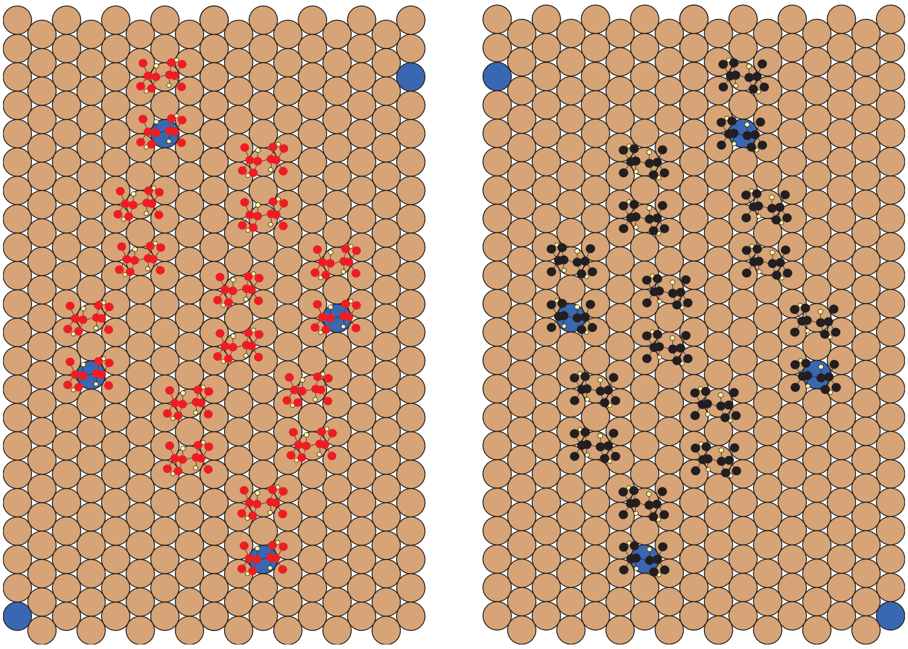

Fig. 4.18 Tentative models for D-TA (red) on Cu(111) forming the $\begin{pmatrix} 7 & -3 \\ 3 & 10 \end{pmatrix}$ structure (left) and L-TA (black) on Cu(111) forming the $\begin{pmatrix} 10 & 3 \\ -3 & 7 \end{pmatrix}$ structure.

calibration of the number of molecules per unit cell in the TA-c(2x4)/Cu(110), the number of TA molecules per unit cell of these structures here was determined.

For racemic tartaric acid on Cu(111) one can either expect a superposition of the two diffraction patterns $\begin{pmatrix} 10 & 3 \\ -3 & 7 \end{pmatrix}$ and $\begin{pmatrix} 7 & -3 \\ 3 & 10 \end{pmatrix}$. This would be a strong indication for separation of the two enantiomers into two homochiral domains, i.e., formation of a 2D conglomerate. If a completely different structure is observed, heterochiral building blocks of the two enantiomers in a racemate crystal might be present.
The racemic mixture crystallizes on the Cu(111) crystal into two domains $\begin{pmatrix} 9 & 0 \\ 0 & 3 \end{pmatrix}$ and $\begin{pmatrix} 3 & 0 \\ 0 & 9 \end{pmatrix}$.
Clearly, the LEED pattern found for racemic TA can not be interpreted as a superposition of the $\begin{pmatrix} 10 & 3 \\ -3 & 7 \end{pmatrix}$ and $\begin{pmatrix} 7 & -3 \\ 3 & 10 \end{pmatrix}$ domains observed for the enantiomers, but represents a superposition of two different mirror domain structures. In cases where a superposition of two mirror domains are observed in LEED, it can be difficult to identify the pattern of the single components. This reflects the situation in which the domains sizes are smaller than the diameter of the probing electron beam. However we managed to prepare samples where the domain size was sufficiently large, i.e. in the range of hundreds of micrometers, in order to separately obtain diffraction patterns of single domains (Figure 4.19).
As mentioned above the different structures suggest, that the racemic mixture forms

heterochiral dimers, which form the two domains as building blocks, aligned into two mirror-like configurations. A similar observation has been made recently for TA on Ag(111) [99,100].

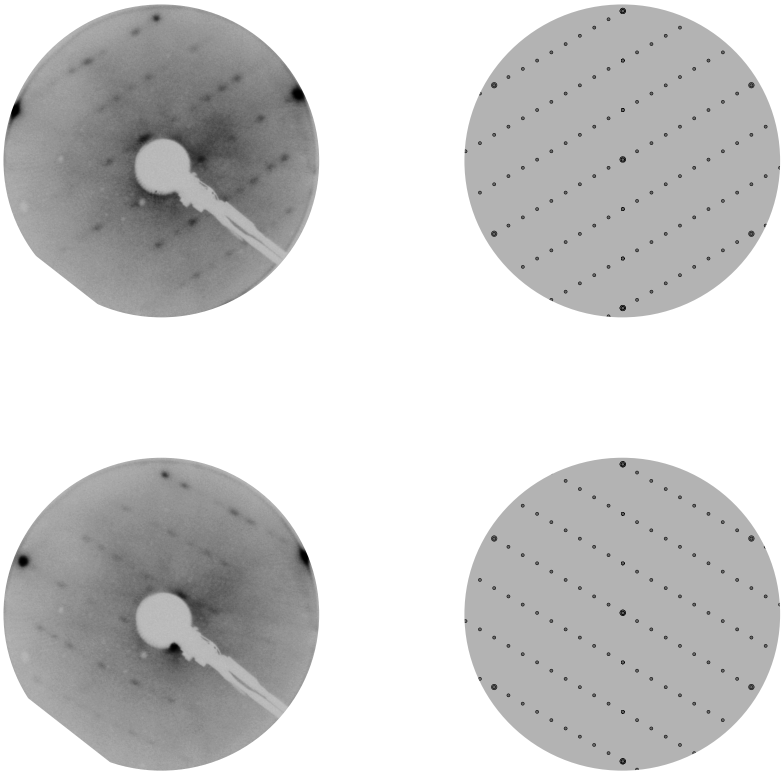

Fig. 4.19 LEED patterns of the $\left(\begin{smallmatrix}9&0\\0&3\end{smallmatrix}\right)$(top left) and $\left(\begin{smallmatrix}3&0\\0&9\end{smallmatrix}\right)$(bottom left) domains found for racemic tartaric acid on Cu(111) with their simulated patterns on the right. The domain sizes were larger than the probing electron beam.

Tentative models for the two mirror structures $\left(\begin{smallmatrix}9&0\\0&3\end{smallmatrix}\right)$ and $\left(\begin{smallmatrix}3&0\\0&9\end{smallmatrix}\right)$ of racemic TA on Cu(111) are given in Figure 4.20. L-TA (black) and D-TA (red) form heterochiral dimers and assemble in two mirror domains sharing the same lattice anchor points. Due to the sixfold symmetry of the substrate it is to be expected, that there will exist three rotational depending sub-domains for each mirror, that coincide with the domains depicted in Figure 4.20. Based on comparison with XPS data for the c(2x4) structure of racemic TA on Cu(110), the number of molecules per unit cell was roughly estimated to be four.

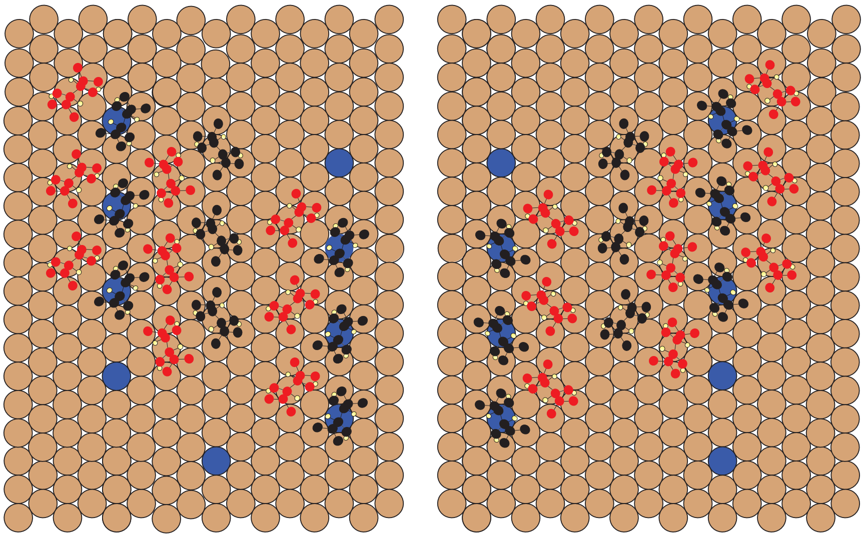

Fig. 4.20 Tentative models for racemic TA on Cu(111) forming two mirror domains, $\left(\begin{smallmatrix}9&0\\0&3\end{smallmatrix}\right)$ left and $\left(\begin{smallmatrix}3&0\\0&9\end{smallmatrix}\right)$ right. Heterochiral dimers are the building blocks of the unit cell.

4.4 Conclusions

The enantiotropic phase transition of the two-dimensional COR/Cu(111) phases was studied with STM and LEED and details on the molecular movement and rearrangement conditions from one phase to the other were identified [50]. This insight in two dimensions can be a starting point for further studies on the driving forces of phase transitions, which are still fairly unknown.

One of the key elements for the investigated phase transitions was a low density phase in close proximity to the densely packed adlayer to provide extra space needed for the rearrangement of the molecules. Eliminating the low density secondary phase by additional deposition of molecules leads to an increased kinetic barrier that stabilizes one phase in the parameter space of another phase. Thereby it is not important whether the low density phase is filled with molecules of the same type (homo-stabilization) or of a completely different species (hetero-stabilization). A qualitative thermodynamic model is proposed.

Deposition of phase I with intrinsically chiral molecules like tartaric acid on top of phase I (COR (4x4)) suppresses the formation of mirror domains in phase II during the phase transition, and if the amount is sufficient, blocks the phase transition to phase III. The proposed mechanisms for the suppression of mirror domains is the decoration of COR domain edges by TA during formation, making certain mirror alignments more favorable. The decoration of tartaric acid at the copper step edges, from which the enantiomorphous growth of the domains are biased is another scenario, but based on the same principle. Finally, we cannot exclude that TA is incorporated in the phase two.

Enantiopure tartaric acid was found to assemble in two mirror structures, $\left(\begin{smallmatrix} 10 & 3 \\ -3 & 7 \end{smallmatrix}\right)$ (L-TA) and $\left(\begin{smallmatrix} 7 & -3 \\ 3 & 10 \end{smallmatrix}\right)$ (D-TA). Racemic tartaric acid does not assemble in this way. The LEED pattern shows the presence of two mirror structures $\left(\begin{smallmatrix} 9 & 0 \\ 0 & 3 \end{smallmatrix}\right)$ and $\left(\begin{smallmatrix} 3 & 0 \\ 0 & 9 \end{smallmatrix}\right)$. This indicates that no spontaneous separation of the two enantiomers occurs and that the L-TA and D-TA have strong lateral heterochiral interactions.

Chapter 5

Electronic Properties

5.1 Electronic Structure of the Adsorbate: COR and Me_5COR

5.1.1 UPS of Corannulene

Figure 5.1 shows UPS data of 1 ML COR on Cu(111), a clean Cu(111) surface and molecular orbitals of the free molecule calculated on the MP2 level of theory, see also the appendix. Similar to the COR monolayer on Cu(110) [46] the lower energy orbitals are clearly visible in the monolayer spectrum. The HOMO - HOMO-3 however are broadened and overlap with the Cu *d* band. This implies a interaction of the corannulene orbitals with the Cu 3*d* and 4*sp* bands.

Figure 5.2 shows UPS spectra of different COR coverage on Cu(111). As was stated above there are no multilayers of corannulene observed at room temperature, therefore no spectrum could be recorded. As for the growth of the monolayer, the vanishing of the copper surface state right under the Fermi level can be clearly seen as well as the diminishing of the Cu *d* band. The HOMO - HOMO-3 can be seen as they broaden together with the Cu *d* band. The vertical lines on the characteristic peaks around the HOMO - HOMO-3, the HOMO-4 - HOMO-7 and emission C and D demonstrate that there are no peak shifts visible for either of them. As expected from the low electron affinity [101], there is no indication for a charge transfer from the copper to the corannulene molecule in the valence band spectra. Charge transfer would reveal itself as new states growing close to the Fermi level. The lack of charge transfer is a major difference to C_{60}.

In Figure 5.3 the UPS spectra for COR deposition at 100 K are displayed, including a multilayer spectrum. The broadening of the HOMO - HOMO-3 and the reduction of the Cu features are the same as seen in the spectra at room temperature deposition. The additional deposition of molecules on top of the monolayer brings changes to the spectrum due to less effective screening of the photo-hole by the valence electrons of copper. The MO's, except for the HOMO - HOMO-3, are downshifted 0.3 eV. The fact that emission A is not shifting can be interpreted that these orbitals are participating in the substrate binding, supporting the hypothesis of a possible hybridization of the COR HOMO with the Cu *d* band. In any case the HOMO appears to be involved in the surface binding.
The shoulder appearing next to emission B around 6 eV binding energy in the multilayer spectrum can not be directly associated with a molecular orbital. A possible explanation is the broadening of the HOMO-6, a centro-symmetrical orbital with symmetry A1, see the appendix. At low temperature deposition some molecules may adsorb without the COR typical tilting, having the five-membered central ring parallel to the surface. This may imply a participation of the HOMO-6 in the substrate binding, resulting in the broadening of the orbital together with the copper feature around 4.5 eV.
Deposition of COR at 220 K into phase II was measured as well, the photoemission data proved to show no significant difference to the 100 K data.

UPS spectra were measured at different emission angles. For work function measurements the emission angle was 15 ° off normal, for spectra showing the molecular orbitals the emission angle was 55 ° off normal. Other angles were measured as well, but the bands show no dispersion.

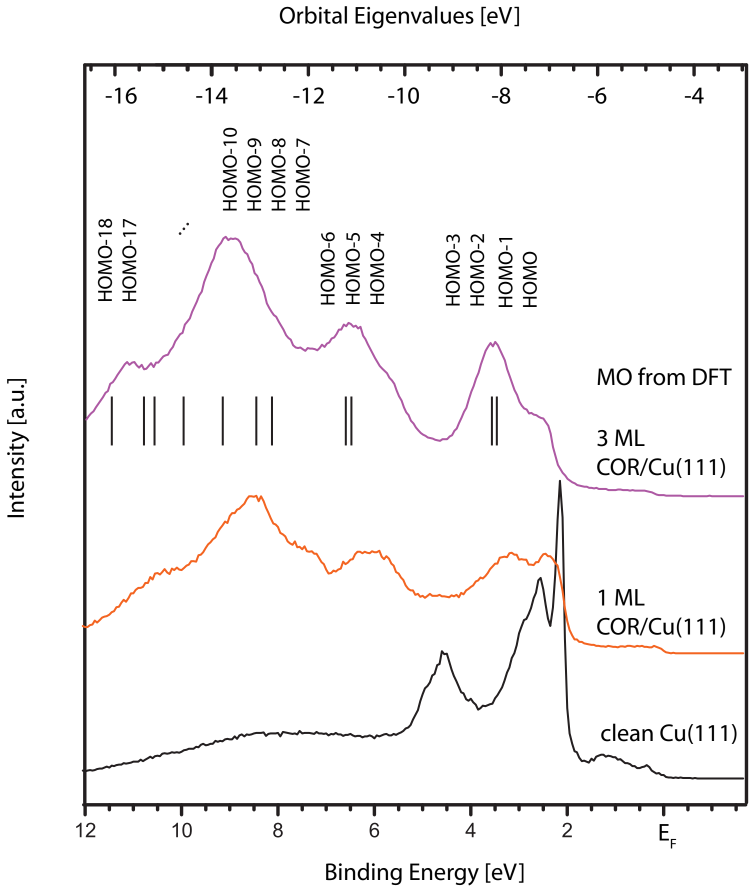

Fig. 5.1 Overlay of a clean Cu(111) UPS spectrum, 1 ML COR on Cu(111), a multilayer of COR/Cu(111) and the molecular orbitals (MO) from DFT calculations. The calculated MO were aligned with the UPS spectra on the HOMO peak. The bottom axis shows the binding energy, the top axis the orbital eigenvalues.

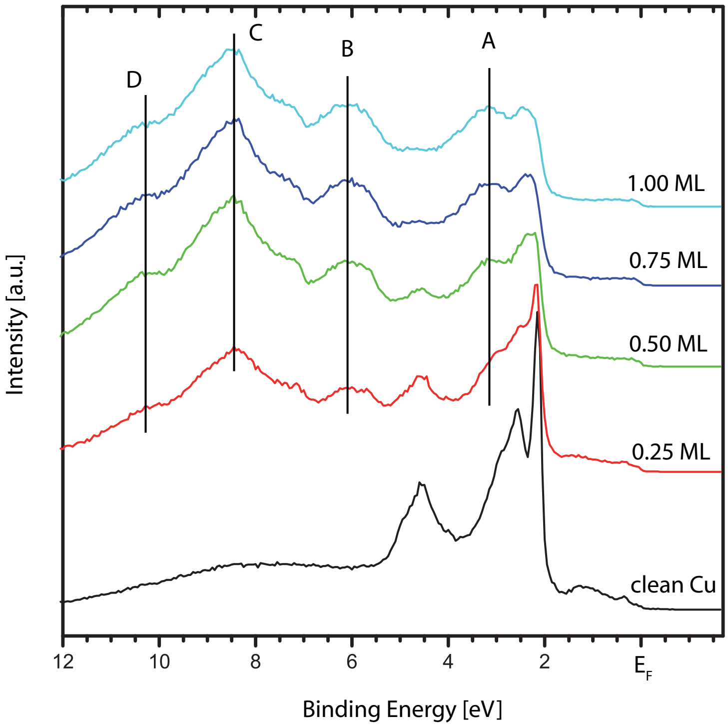

Fig. 5.2 Coverage dependence of 55° off normal emission UPS spectra of COR on Cu(111) deposited at room temperature. Due to second layer desorption no multilayer spectra can be recorded at room temperature. The vertical lines mark the peak position corresponding to the HOMO - HOMO-3 (A), HOMO-4 - HOMO-7 (B), HOMO-8 - HOMO-14 (C) and HOMO-15/HOMO-18 (D) states.

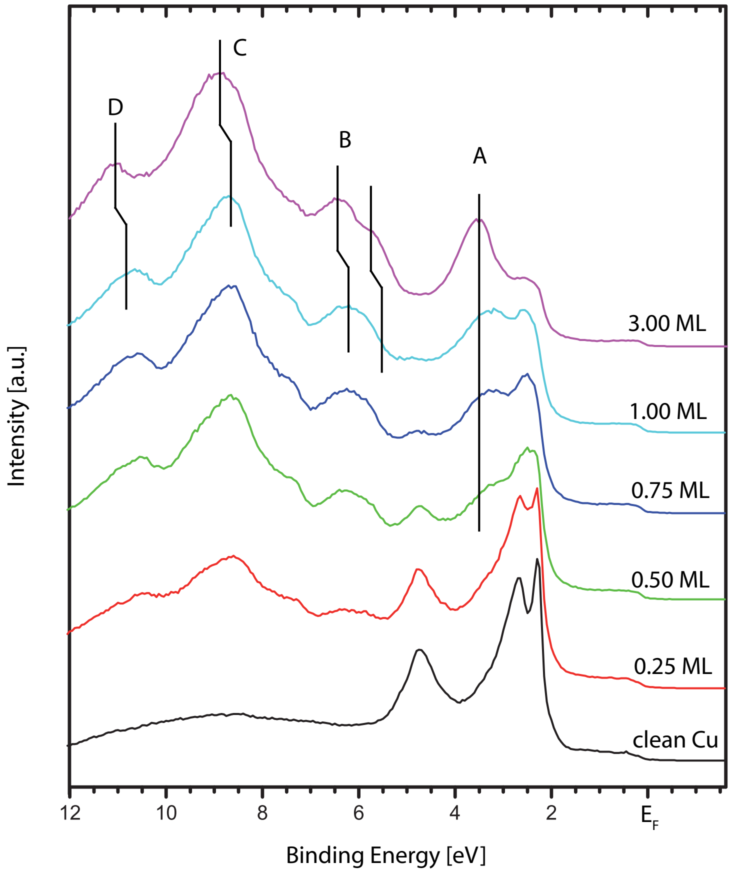

Fig. 5.3 Coverage dependence of 55° off normal emission UPS spectra of COR on Cu(111) deposited at 100 K including multilayer spectra. All of the molecular orbitals shift by 0.3 eV in the multilayer as expected. The HOMO emission shows no shift, due to their participation in the bonding to the copper substrate. The shoulder off emission B may be associated with the HOMO-6 broadening. Deposition of COR into phase II at 220 K showed identical results.

5.1.2 UPS of Me_5COR

55 ° off angle emission UPS spectra of a clean Cu(111) substrate exposed to Me_5COR deposition are shown in Figure 5.4. The characteristic emissions B and C start to grow at 5.75 eV and 8.25 eV as well as the HOMO - HOMO-3 emission A partly within the Cu *d* band at 3.25 eV. The diminishing of the copper features around the *d* band as well as the disappearance of the copper surface state close to the Fermi level can be seen as well. Upon completion of the monolayer, the HOMO - HOMO-3 feature is already fairly broadened, same as for the COR/Cu(111) monolayer.
The deposition of additional layers on top of the monolayer leads to a different effect in the spectra compared to the COR/Cu(111) system. Most of the bands shift approximately 0.3 eV to higher binding energy identical with COR. Where emission A was pinned and unshifted due to participation in the surface binding with COR, here the HOMO band shifts the same 0.3 eV and is therefore interpreted as not being part of the surface binding. Only one band appears not to be shifting to higher binding energy: one of the two peaks in emission B at 5.5 eV. The HOMO pinning in COR can be explained with the tilting of the molecule on the Cu(111) surface. One of the six-membered rings of the rim lies flat on the substrate over a threefold hollow site [50,51]. The HOMO - HOMO-3 orbitals are not centro-symmetrical, but asymmetric over the COR-rim. Tilting might favor participation of these orbitals in the substrate binding. Since the Me_5COR molecule can not tilt to one side in order to align a six-membered ring with the substrate due to the bulky methyl groups on the rim, it is forced to expose the center five-membered ring to the copper. For Me_5COR the HOMO-4 is situated at around 6 eV binding energy and is located on the center fivefold ring (see calculations in the appendix), similar to the HOMO-6 of COR (appendix). The binding of Me_5COR to the substrate may be interpreted as a participation of the HOMO-4 on the center five-membered ring due to the inability to tilt, leading to the broadening of the molecular orbital together with the copper feature around 4.5 eV in the multilayer spectrum in Figure 5.4.

Angle resolved UPS was measured as well, but same as for COR, the bands show no dispersion.

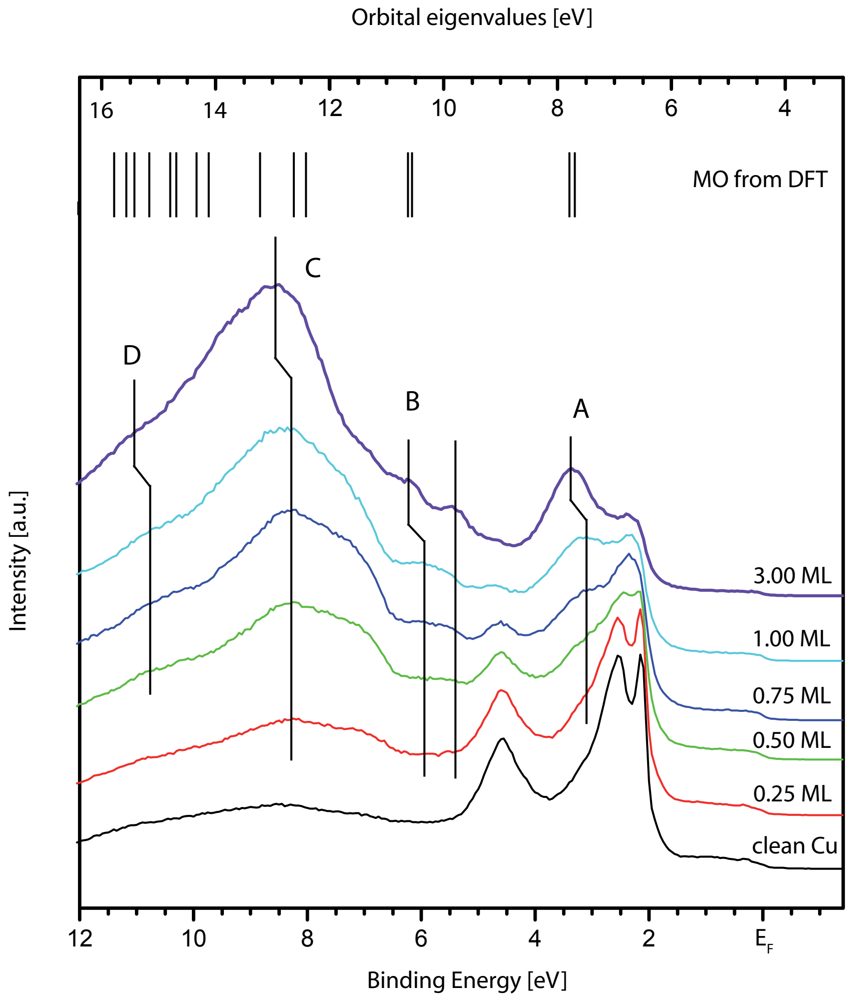

Fig. 5.4 Coverage dependence of 55 ° off normal emission UPS spectra of Me_5COR on Cu(111) deposited at 100 K including a multilayer spectrum and molecular orbitals calculated on the MP2 level of theory. The MO are hand-aligned with the HOMO mission in the spectra. All of the molecular orbitals shift by 0.3 eV, including the HOMO emission. This indicates that these orbitals are no longer participating in the substrate binding, due to no effective alinement of a sixfold ring with the copper substrate. The HOMO-4 peak as part of emission B broadens together with the copper feature around 4.5 eV, indicating a possible participation of the HOMO-3 in the surface binding.

5.2 Interface Dipole Moment

In collaboration with theoreticians from the University of Zurich the interfacial dipole moment and the resulting work function change of the COR/Cu(111) system was investigated. The intrinsic dipole moment of corannulene is 2.1 D, as measured by exploiting the Stark effect in Fourier transform microwave spectroscopy [61]. From this it is clear that corannulene is an exceptionally polar molecule, although it can be guessed due to the bowl shape and the dominant π system, that the molecular dipole has to be significant. As will be shown further down, the interfacial dipole moment of COR/Cu(111) is opposite to the molecular dipole moment and even larger due to the electronic properties of the molecule - substrate interaction.

The magnitude of the surface work function is of particular interest with corannulene, regarding its possible application in field emission devices or photovoltaics. The interfacial dipole moment together with the intrinsic dipole moment is closely connected to the surface work function and therefore included in the investigation.

The work function change ($\Delta\phi$) and the system interface dipole are related via the Helmholtz formula:

$$\Delta\phi = \frac{\Delta\mu}{\epsilon_0 A} \tag{5.1}$$

where $\Delta\mu$ is the interface dipole (including the intrinsic molecular dipole), ϵ_0 the permittivity of vacuum and A the substrate area per molecule. The area per molecule A is becoming smaller with increasing coverage. This formula predicts a linear change of the work function with increasing coverage until the monolayer is full. Since this would be only the case when the molecular dipoles do not affect each other even in close packing, the Helmholtz formula is only accurate for small coverage, where the work function change is linear. By fitting the formula to the linear $\Delta\phi$ at low coverage the interfacial dipole moment of the system can be estimated. It is however not suited to make predictions on the nearly full or full monolayer.

The Topping model [102] takes depolarization effects into account and may therefore be used for a curve fit to determine the system dipole moment and the polarizability of the adsorbate-substrate complex. The following equation 5.2 is an adaptation of the original formula by Topping as used in [103] and [104].

$$\Delta\phi = \pm \frac{p_0}{\epsilon_0} \frac{\theta b}{d^2} \left(1 + \frac{\alpha \xi}{4\pi\epsilon_0} \frac{\theta^n \left(\theta b\right)^{3/2}}{d^2} \right)^{-1} \tag{5.2}$$

with p_0 being the interfacial dipole moment, ϵ_0 the permittivity of vacuum, θ the coverage in monolayers ($0 < \theta < 1$), b a lattice dependant correction factor ($= 2/\sqrt{3}$ for triangular lattice), d the nearest neighbor distance in the monolayer and α the polarizability of the molecule on the surface. ξ is a constant describing the dipole-dipole interaction in the full monolayer. It is lattice dependent and $= 11.034$ for a triangular lattice. The exponent n is a correction constant for the molecular mobility in the sub-monolayer coverage ($0 > n > -0.5$, with $n = 0$ for ordered low density structure and $n = -0.5$ for disorder).
As a starting point for fitting a measured curve with the Topping model, p_0 was calculated as μ from the Helmholtz equation 5.1.

All UPS spectra for work function measurements were conducted at 15 ° off normal emission angle for maximum secondary electron yield. The absolute work function of the clean Cu(111) surface was determined to be 4.9 eV, in agreement with the literature value of 4.94 eV [105]. The absolute work function of Cu(111) was also taken into account to determine the cleanliness of the substrate before deposition.

5.2.1 $\Delta\phi$ of the COR/Cu(111) system

A classic curve shape for deposition of organic molecules on a metal surface shows a characteristic drop in work function on the onset of deposition followed by gradual leveling off, completed at one monolayer coverage. This is for molecules that reduce the work function of a system. The same principle applies for systems that increase the work function. In some case the work function change shows a minimum at one monolayer coverage, followed by a small relaxation induced by the second layer. This relaxation is due to the screening effect of the second layer, which reduces the effect of the first layer. In any case the work function levels off and is not changing upon further deposition. The interface between the solid (i.e. the deposited molecules or the clean metal) and the vacuum is influencing the work function of the system and as soon as the whole relevant interface is covered with molecules, the work function will not change anymore (with the exception of second layer screening). This is the reason why the work function change measurement is sometimes used to determine the completion of a molecular monolayer.

Figure 5.5 (top) shows the change in work function measured from the secondary electron cut-off with UPS (black) for room temperature deposition of corannulene on Cu(111). The red curve is a fit with the adapted equation of Topping. The three fit parameters interfacial dipole moment (p_0), polarizability (α) and the correction constant for the molecular mobility (n) were hand fitted with first priority on p_0. The values for the deposition of COR at room temperature are $p_0 = 8.8\,\mathrm{D}$, $\alpha = 12\,\text{Å}^3 = 1.33 \cdot 10^{-39}\,\mathrm{Cm^2V^{-1}}$ and $n = 0$. The correction constant $n = 0$ indicates that the molecular adlayer grows in ordered islands, as was expected and is in agreement with the continuous decrease in work function.

The interfacial dipole moment of 8.8 D is tremendously large but is in good agreement with the result by the Helmholtz equation for very low coverage ($\sim 0.1\,\mathrm{ML}$) of 8.6 D. The polarizability of $12\,\text{Å}^3$ is lower than the polarizability of the free molecule of $36\,\text{Å}^3$, since it is in contact with the metal surface. The deviation can be explained by the charge redistribution in the molecule-substrate interface. A detailed insight into the charge redistribution of COR/Cu(111) is published by our coworkers in [51].

Figure 5.5 (bottom) shows the work function change curve for corannulene on Cu(111) deposited at 220 K. The total work function change at 1 ML coverage for phase II is lower at 1.35 eV than for phase I at room temperature (1.55 eV). The curve is again fitted with equation 5.2. The fitted curve gives the polarizability of corannulene again as $\alpha = 12\,\text{Å}^3 = 1.33 \cdot 10^{-39}\,\mathrm{Cm^2V^{-1}}$ for phase II, equal to the room temperature phase as expected.

For phase II the interfacial dipole moment is around 8.0 D with very low coverage. The decrease in work function change as well as in the interfacial dipole moment compared to phase I can be explained with the increased density of molecules, i.e. dipolar units, on the substrate. The meta-stable phase II at 220 K has a 14.3 % higher density of molecules on the surface compared to the room temperature phase I. The decrease in $\Delta\phi$ for phase II compared to phase I is 0.2 eV or 13 %, which lies within the expected precision of the measurement.

The work function change was also measured for the deposition into phase III at 90 K. The results show basically the same trend as for phase II. The key values are given in table 5.1 together with the other phases.

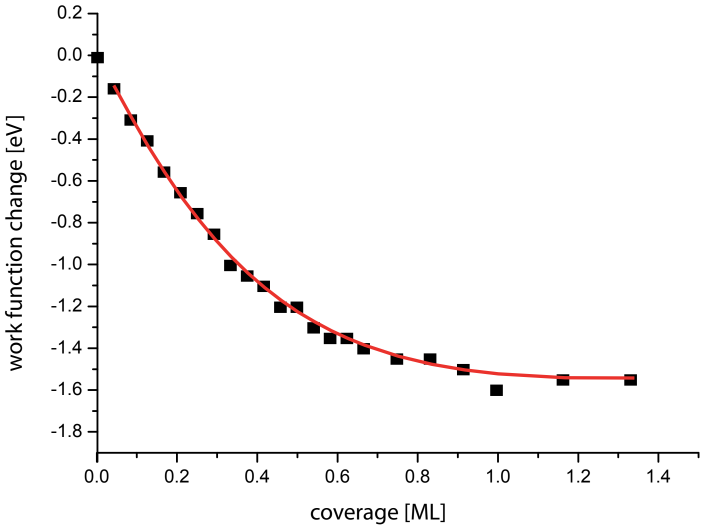

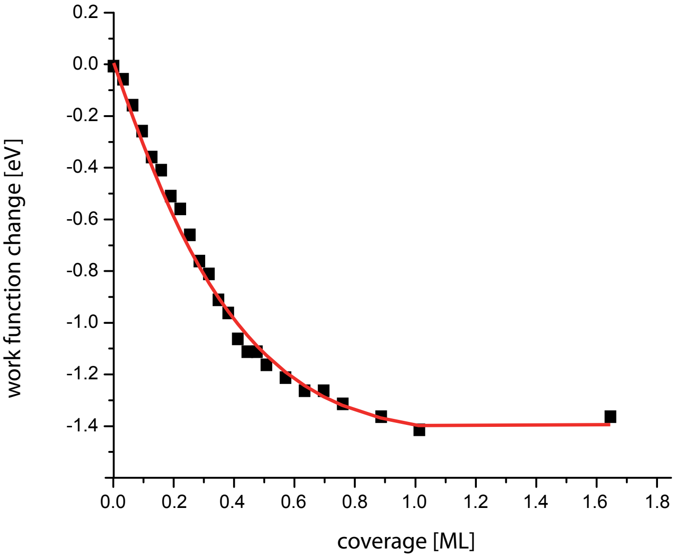

Fig. 5.5 Work function change measurement for COR on Cu(111) deposited at room temperature into phase I (top) and at 220 K into phase II. The measured data was fitted with the Topping model. Fitting parameters phase I: $p_0 = 8.8\,\mathrm{D}$, $\alpha = 12\,\text{Å}^3$. Phase II: $p_0 = 8.0\,\mathrm{D}$, $\alpha = 12\,\text{Å}^3$. The correction constant for the molecular mobility for both phases was n = 0, indicating that the molecules are not randomly distributed on the substrate at small coverage.

5.2.2 $\Delta\phi$ of the $Me_5COR/Cu(111)$ system

In Figure 5.6 the work function change is plotted against coverage. The total work function change for a full monolayer of Me_5COR on Cu(111) is 1.6 eV. The same fit (red) from equation 5.2 as with COR was used to check the molecular dipole moment in comparison to corannulene. The fitted interfacial dipole moment is 8.0 D, the resulting polarizability of Me_5COR is 12 $Å^3$. The theoretic value for the polarizability of Me_5COR, calculated on the free molecule in gas phase, is 45.5 $Å^3$. As with COR/Cu(111) the reduced polarizability upon adsorption is due to the charge redistribution at the molecule - substrate interface.

The interfacial dipole moment of Me_5COR/Cu(111) shows the same behavior as for COR/Cu(111).

Surprisingly the interfacial dipole moment for 1 ML COR and for 1 ML Me_5COR appear to be the same, although the dipole density per unit area is different in the two systems. A possible explanation is, that the effect of the lesser density of Me_5COR (one molecule per 1.52 nm^2) compared to COR (one molecule per 0.90 nm^2) is compensated by the molecular orientation on the surface. We recall that COR is substantially tilted, while no such tilt could be observed for Me_5COR.

The effect of the individual intrinsic dipole on the interfacial dipole is depending on the angle of the dipolar axis towards the surface normal. The effect of the individual dipole and therefore of the sum of all surface dipoles is greatest when the dipolar axis is normal to the surface. There are less dipoles per unit area in the Me_5COR monolayer, but the individual molecular dipole is "better" aligned and contributes more to the interfacial dipole moment.

Table 5.1 gives an overview on the interfacial dipole moment calculated with the Helmholtz and Topping formula and the absolute change in work function for a full monolayer of all three COR phases and for Me_5COR.

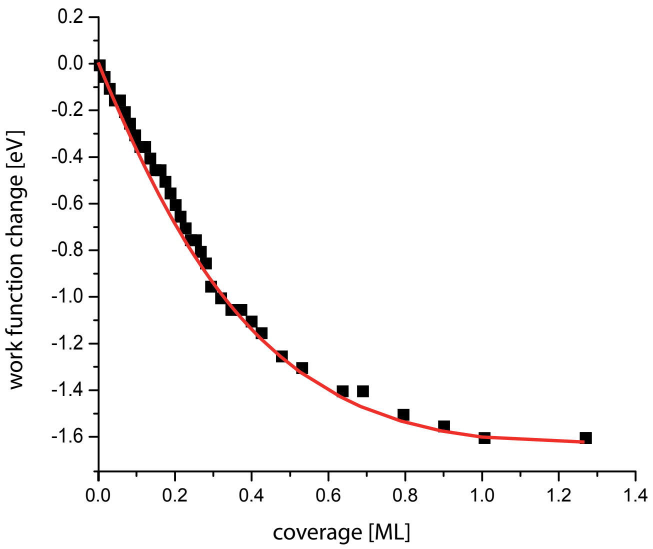

Fig. 5.6 Work function change measurement for Me_5COR on Cu(111) deposited at room temperature. The measured data was fitted with the Topping model, resulting in a interfacial dipole moment for small coverage of 8.0 D, a Me_5COR/Cu(111) polarizability of 12 Å^3 and a correction constant for the molecular mobility of n = 0.0.

	interfacial dipole moment by Helmholtz [D]	interfacial dipole moment by Topping [D]	$\Delta\phi_{max}$ [eV]
COR - phase I	8.6	8.8	-1.5
COR - phase II	6.4	8.0	-1.35
COR - phase III	6.5	7.5	-1.3
Me_5COR	9.0	8.0	-1.6

Table 5.1 Overview on the interfacial dipole moments and maximal work function changes of COR and Me_5COR phases.

5.3 Conclusions

Coverage dependent UP spectra of COR/Cu(111) show the growth of the characteristic emissions for corannulene as deducted from theory and gas phase photoelectron spectroscopy. Unlike the C_{60}/Cu(111) system, which features the HOMO between the Cu *d* band and the Fermi level, the corannulene HOMO overlaps with the Cu *d* band. Until completion of the monolayer, the molecular bands do not shift but grow steadily. The deposition of multilayers on top of the monolayer causes a shift of all molecular bands of 0.3 eV to higher binding energy except for the HOMO associated band, which does not shift at all. This pinning is an indication of the participation of the HOMO in the binding to the copper substrate. The tilting of the COR bowl leads to an overlap of the HOMO with the copper *d* band. There is no indication for a charge transfer upon COR deposition.
As for the coverage dependent UP spectra on Me_5COR/Cu(111), a very similar result was observed. All molecular emissions shift to 0.3 eV higher binding energy, including the HOMO, except for a small band associated with the HOMO-4 located at the center five-membered ring, which shows no relaxation shift. Due to the large substituents on the COR rim, the molecule is unable to tilt in a way to align a six-membered ring with the substrate and is therefore stuck with the center ring alinement. Therefore surface bonding might be established by the HOMO-4, not the HOMO.
UPS measurements indicate that there is no significant charge transfer occurring. ARUPS measurements were conducted on all three phases of COR and on Me_5COR. None of the samples displayed significant angle dependence.

Work function change measurement for COR/Cu(111) showed a decrease of 1.5 eV for the room temperature phase and 1.35 eV for the low temperature phases II and III. The difference in the work function change for the two phases is based on the different molecule density in the two phases. Phase II at 250 K shows 14 % higher density than the room temperature phase I. The increased density in the adlayer leads to a decrease in the adsorption induced interface dipole due to the depolarizing field created by neighboring molecules. The increased density in phase II is also decreasing the total work function change for one monolayer coverage. Due to the fact, that at low deposition temperature corannulene directly assembles into the thermodynamically stable phase, the substrate is covered with growing islands of the high density structure. The work function change therefore never reaches the value of phase I. Deposition of one monolayer of Me_5COR leads to a work func-

tion decrease of about 1.6 eV like corannulene despite the lesser molecule density in the adlayer. The orientation of the molecular dipole is normal to the surface with Me_5COR due to the inability to tilt. This hinders the depolarization effect of the molecules on their neighbors and balances the effect of lesser dipole density.
For COR and Me_5COR the interfacial dipole moment was calculated to be around 8.0 eV. This value is surprisingly high and thought to be due to significant charge redistribution at the interface.

Chapter 6

Alkali Metal Doping of COR and Me_5COR

Neither corannulene nor pentamethyl-corannulene show a significant charge transfer from the metal substrate when adsorbed on the Cu(111) surface. The low ionization potential of alkali metals make this group of metals well suited to induce charge transfer to the molecules. This may induce metallic behavior in the organic films due to partially filled molecular orbitals. Alkali metals are known to decrease the work function of transition metals [106].

6.1 Cesium doped COR and Me_5COR

Corannulene and Me_5COR were both investigated with UPS on Cu(111) and on thick films of metallic Cesium, deposited on Cu(111). The metallic Cs films were deposited at 80 K on the Cu(111) crystal until characteristic metal features could be identified in the UPS spectra. Depositing the molecules onto a metallic-like Cs film allowed to obtain the spectroscopic fingerprint of the highest doping level. Both, the molecule covered metallic Cs and the Cs exposed molecular monolayers, were heated up to determine the evolution of the doped layers.

Figure 6.1 displays a series of UPS spectra of a thick film of metallic Cs exposed to corannulene deposition at 100 K. The spectrum of the metallic Cs film (black) features the characteristic 5 $p_{1/2}$ and 5 $p_{3/2}$ peaks of Cesium at 12 and 13.8 eV binding energy as well as a very weak Fermi edge emission and the characteristic valence auger edge at 9.5 eV. The 5 $p_{1/2}$ is split into a very sharp doublet. The Cs film is thick enough to extinct any Cu feature, the 5 $p_{1/2}$ peak splitting and the

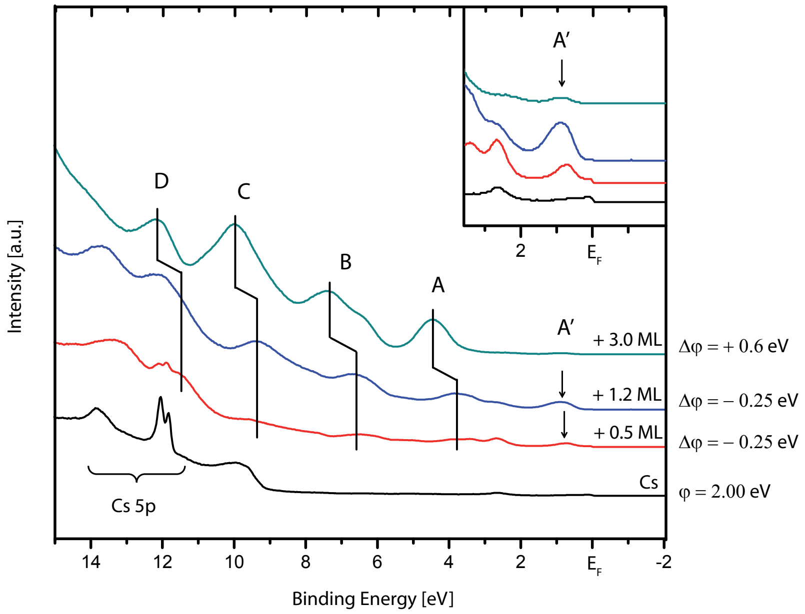

Fig. 6.1 UPS spectra of a metallic Cesium film, exposed to COR deposition at 100 K.

valence auger edge however occur only in metallic Cs films.
The 5 p peaks disappear upon gradual deposition of COR and are completely quenched in the 3 ML spectrum. Another indication of layer-by-layer growth.
With increasing deposition of COR, a new feature A' at -0.8 eV appears, besides the expected features belonging to the main emissions A to D. This feature can be associated with the corannulene LUMO being occupied on formation of a charge transfer complex and the LUMO appears in the spectrum as emission A'. This gives reason to believe that the nature of the COR-Cs bonding is ionic, due to the donation of filled metal states to the π^* LUMO of COR. The work function of the Cs doped COR film are extremely low at values around 1.75 eV. The topmost spectrum in Figure 6.1 with 3 ML COR refers already to the undoped multilayer of corannulene, as can also be seen in the increased work function.

UP spectra of the gradual adsorption of Me$_5$COR onto a metallic Cs is presented in Figure 6.2. The Cs film was not quite as thick as the one used for COR deposition as can be seen in the small copper *d* band features that are still visible. However, the Cs 5 $p_{1/2}$ and 5 $p_{3/2}$ peaks are visible and they also displays the characteristic splitting of a metallic Cs film, together with the valence auger edge. At a film thickness of about 7 ML the distinct features of the Me$_5$COR orbitals are clearly

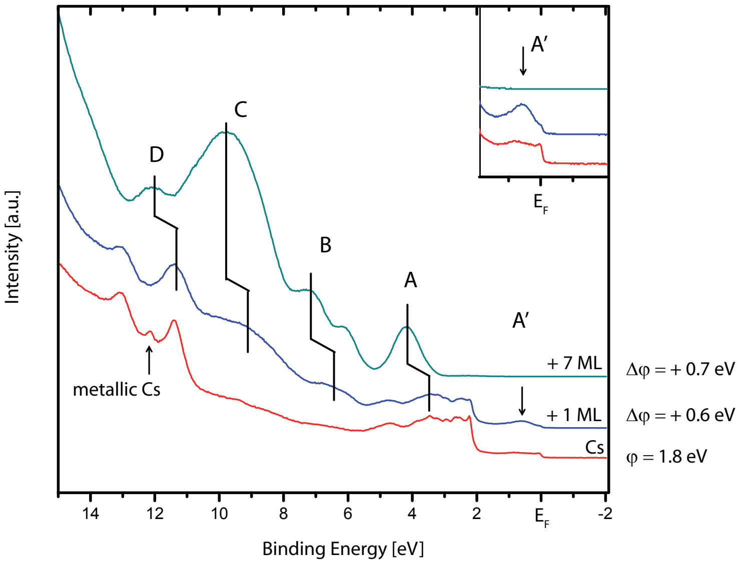

Fig. 6.2 UPS spectra of a metallic Cesium film exposed to Me_5COR deposition at 100 K.

visible. This spectrum is already associated with the undoped multilayer.

On deposition of approximately 1 ML of Me_5COR the change in the spectrum is dominated by the reduction of the Cs 5 p peak areas. The disappearance of the sharp 5 p peaks is followed by replacement of broader features with about 0.5 eV higher binding energy, associated with the 5 p features of Cs dispersed in the organic overlayer. The 5 p peaks can still be identified in the 7 ML spectrum in the broad shoulder around 14 eV and the too dominant D emission at 11 eV. The Cs obviously diffuses into the organic overlayer as was expected from the Cs doped COR spectra in Figure 6.1.

Apart from the changes in the Cs features, the growing emissions associated with bands A to C can be observed around 1 ML coverage at 3.2 eV, 4.7 eV and 6.2 eV, and 9 eV. Additionally a peak appears around 0.7 eV binding energy. This is the important finding for these spectra, that once again the filling of the Me_5COR LUMO becomes visible in emission A'. Both COR and Me_5COR experience a charge transfer from the Cesium.

Both for COR and Me_5COR on a thick Cs film no significant angle dependence of the emissions A to D of either molecule can be observed. Due to the bowl-shape of the two molecules there exists no conformation where all the six-remembered rings are equally oriented on the substrate, regardless of a possible tilting of the molecule.

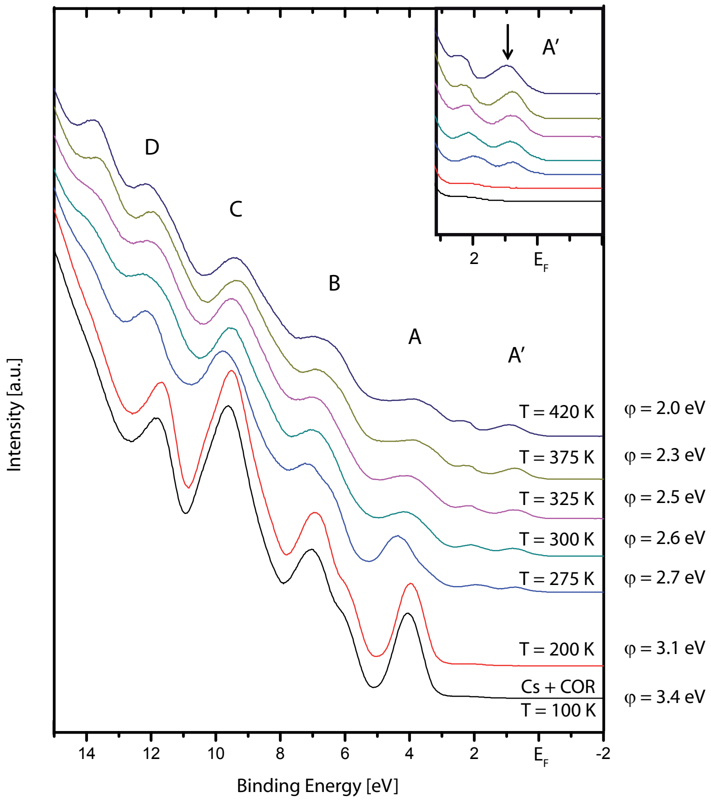

Fig. 6.3 Temperature evolution of a fully Cs doped corannulene film on Cu(111).

The molecular multilayers on the metallic Cs films were deposited at 100 K, since Cs will desorb from the metal substrate at room temperature. Upon completion of the molecular deposition, the Cs-molecule film was gradually heated to determine the behavior of the emission features and the stability of the complex. In Figures 6.3 and 6.4 UP spectra documenting the gradual heating of thick films of corannulene and Me$_5$COR on metallic Cs are depicted. As TPD experiments both with COR and Me$_5$COR showed (see chapters 4 and 3), the multilayer desorbs from the thick film at around 300 K for COR and 350 K for Me$_5$COR. This was also confirmed with UPS measurements showing the disappearance of the multilayer emissions for both molecules together with the reappearance of the copper features, mainly the *d* band.

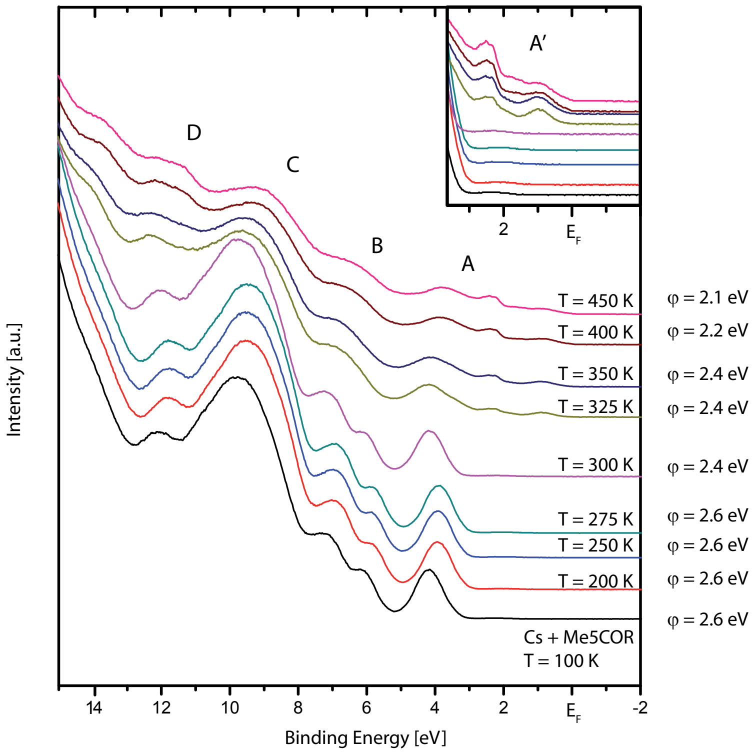

Fig. 6.4 Temperature evolution of a Cs doped Me_5COR film on Cu(111).

Figure 6.3 on COR shows a slight shift to lower binding energy in the emission spectrum at 200 K. Between 200 K and 275 K the spectra change drastically. On one hand the molecular features decrease and broaden, on the other hand the occupied LUMO and a second peak that may be associated with the destabilized HOMO suddenly appear. There is also a shift to higher binding energies, that gradually diminishes on further heating up to 420 K. The rest of the spectra show no significant change, apart from the slight shift in energy over the whole spectra. Also at 420 K, the Cs doped COR emissions are still very pronounced and show no sign of decomposition. Also there is no sign of increased intensity around the Cu *d* band or the fermi level indicating that desorption is not an issue and decomposition is not present. The close-up shows the situation in the binding energy range between the HOMO and the Fermi level. Starting from 275 K the LUMO is clearly visible around 1.0 eV. This indicates that at increased temperatures the Cs becomes mobile in the COR matrix and is diffusing in the film resulting in a change in the local density of Cs atoms per molecule. The appearance of the LUMO can be interpreted as the Cs increasingly dispersing in the COR film and doping all the molecular layers, that were undoped in the thick film before. The doping states that were previously buried under molecules, now reappear.

The absolute work function is shown beside each spectrum. The minimum work function for the maximum temperature was determined to be 2.0 eV, an extremely low value. Although the spectra from 300 to 420 K only show slight shifts, gradual decrease and broadening in the emissions, the work function of the film changes substantially from 2.5 to 2.0 eV. This indicates, that the inter-diffusion of Cs in the COR film is still happening, as can also be seen in the gradual increase in the two peaks in emission A'.

A similar picture is shown in the case of Me_5COR in Figure 6.4. The original spectrum from 100 K looks undoped and is based on a thick layer of molecules on top of a metallic Cs film. It is stable and shows no sign of change up to 300 K, where a slight shift to higher binding energy can be observed, followed by a gradual shift to lower binding energy. From 325 K on the dominant band at 9 to 10 eV is drastically reduced, although still present and dominant. The apparent reduction of emission C is based on the increase of the emission around 12 eV binding energy. It is associated with the reappearance of the broadened Cs 5 p peaks, which show up due to increased diffusion of Cs in the molecular film. At the same temperature the features between the HOMO and the Fermi level reappear same as with corannulene. The spectra starting from 325 K show the Cs doped Me_5COR, whereas the spectra up to 300 K basically show the pure molecule in a thick film.

The absolute work function of the doped thick film was determined to be 2.1 eV. This value is larger than the value for the Cs doped COR film, but still very low. The difference might come from different amounts of Cs in the molecular film. As from the work function can be seen, nothing is happening to the film until 275 K. However the biggest change in work function only happens above 350 K, where there is only little change in the emissions A to D. The change in the emission A' shows that the diffusion is still taking place and the maximum doping is only reached at 450 K, in agreement with the work function change.

Preliminary NEXAFS studies were conducted on the COR and Me_5COR monolayer on a Cu(111) substrate as well as on a single doping step of 4 minutes Cs deposition on each of the adlayers. Spectra were taken at different incident and emission angles and proved to show no significant difference from which to derive statements on orientational symmetries. All spectra presented were normalized and submitted to division by a spectrum of a clean Cu(111) sample. The curves were smoothed afterwards.

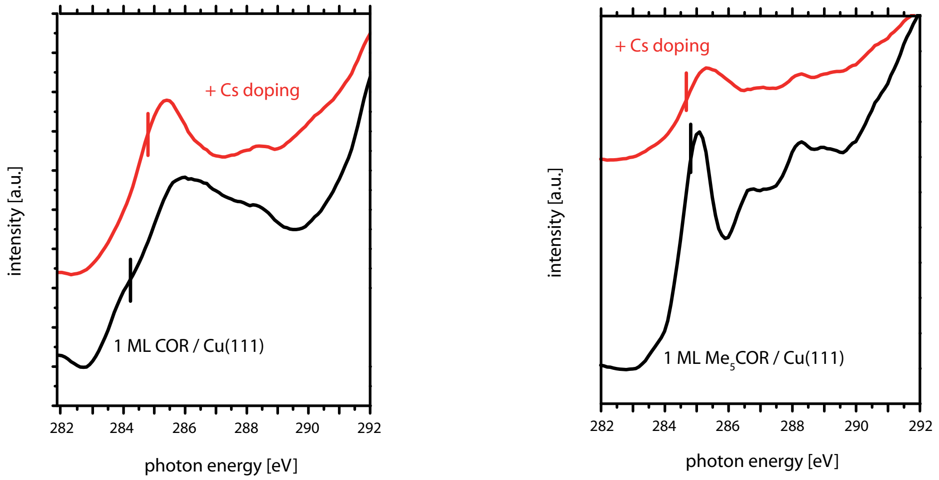

Fig. 6.5 C 1s NEXAFS spectra of 1 ML COR on Cu(111) (black) and the same adlayer doped with Cs (red) with normal incident light. The vertical bars indicate the binding energy of the C 1s level. The spectra are corrected as stated in the text. The peak around 285 eV is associated with the π^* LUMO of corannulene and appears to be narrower, indicating a partial population of the LUMO.

The two NEXAFS spectra in Figure 6.5 show the C 1s transitions for 1 ML COR / Cu(111) and Me$_5$COR/Cu(111) and the Cs doped adlayer of each in red. Although these are preliminary results, there is one major contribution to the hypothesis of charge transfer from the Cesium to corannulene and Me$_5$COR. The C 1s to π^* transition that is dominant in the spectra loses intensity with the doped monolayer compared to the undoped. With the LUMO being partially occupied, there are less allowed transitions to the LUMO from core states and the intensity in the spectrum goes down.

These preliminary results with NEXAFS do not allow for a determination of the amount of charge that is transferred to one molecule. From the temperature evolution experiment (described in Figure 6.3) a crude estimation of the amount of Cesium that is participating in charge transfer complex formation per corannulene molecule can be done. XPS measurements (Figure 6.6) of the stable COR-Cs thick film were conducted and the peak areas of the C 1s and the Cs 3$d_{5/2}$ were weighted according to the atomic sensitivity factor. The resulting ratio is 5.1 : 1 C 1s to Cs 3 $d_{5/2}$. This is equivalent to 20 carbon atoms or 1 COR per 3.9 Cs atoms. Almost four Cs atoms coordinate with one COR, each contributing one electron to the charge transfer complex, resulting in charge transfer of roughly 4 e$^-$ per molecule. This suggests that the LUMO and the LUMO+1 are filled.

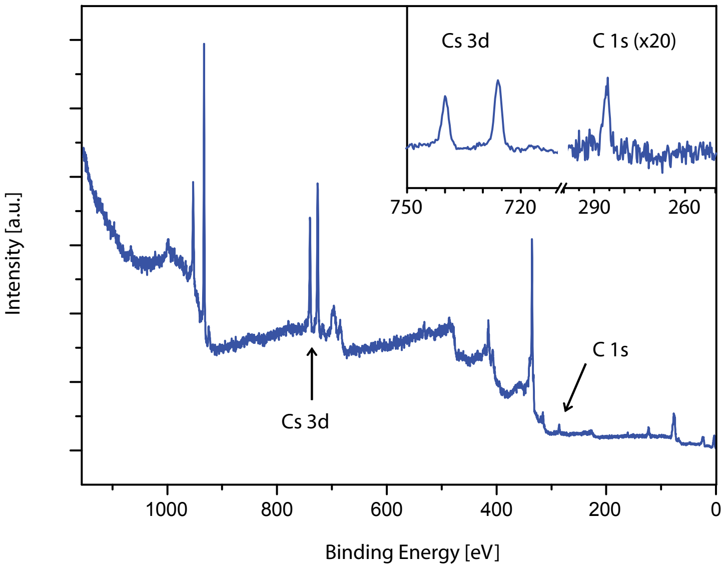

Fig. 6.6 XPS of the annealed COR / Cu(111) film, after the temperature evolution experiment. The inset shows the Cs 3d and C 1s peaks used to estimate the number of Cs atoms that coordinate to one COR molecule.

As was first shown by Ayalon et al. in 1992, corannulene is able to coordinate four alkali atoms by accepting four electrons and obtaining a stable closed-shell tetraanion configuration [107]. This extraordinary supercharging of the molecule is only possible due to the fact that the LUMO of COR is doubly degenerate and lies below the anti-bonding energy level. The tetraanion was proposed to build a stacked conformation of dimers in solid state, sandwiching half of the coordinated alkali atoms between two bowl-in-bowl stacked corannulenes [108–110]. The extra charge in the molecules is thought to be distributed in two concentric closed ring systems, an anion-within-anion complex, similar to the proposed conformation of the polarized form of COR in the introduction in Figure 1.1.

Theoretic calculations state a slightly more favorable position for alkali atoms on the convex side of COR, for transition metal atoms a strongly favorable position on the convex side [27]. However the energy difference is small for alkali metals and the literature proposed sandwich structure seems reasonable.

The different reduction steps of COR with Lithium have been studied by hydrogen nuclear magnetic resonance (H^1 NMR) in reference [111], showing dianions and trianions existing as stable diamagnetic species. They also found that the reduction steps to the trianion and the tetraanion were only possible with Lithium with their samples dried from solution in tetrahydrofuran (THF). It was proposed that Potassium ions were to large to stabilize the corannulene anion from the convex side in the preferred dimer form.

The analogy to organometallic complex chemistry in the Cesium doping of COR and Me_5COR under the measured conditions seems reasonable under the postulation of charge transfer complexes both at the molecule - alkali substrate interface and the interdiffused thick film. The ionic character of the complex formation is supported by the high temperature stability of the thick film far beyond the desorption temperature of either of the participating components. The occupation of the LUMO as shown with UPS measurements supports the ionic character of the binding as well.

6.2 Conclusions

Alkali metal doping experiments were conducted on Cesium with corannulene and with Me_5COR. As with other aromats a charge transfer from Cs to the molecules is observed. The occupation of the LUMO is clearly observed in UPS.
The interdiffusion of Cs and COR multilayers is observed by the stabilization of the thick film to high temperatures far above the desorption temperature of pure Cs or COR on Cu(111). The coordination of four Cs atoms per corannulene molecule was estimated using XPS.
Cs doping of corannulene and Me_5COR leads to another work function reduction of $1.4\,\text{eV}$. This results in an immense total work function change of $-2.9\,\text{eV}$.

Chapter 7

Summary and Conclusion

Looking back on the aim of the thesis as stated in the introduction. The four questions posed in the beginning may be answered as follows:

- COR and Me_5COR show no charge transfer on Cu(111) in contrast to C_{60}. Also in contrast to C_{60} they invoke a large work function change of $-1.5\,\mathrm{eV}$. This results in an unusually high interfacial dipole moment of over $8\,\mathrm{D}$, which is based on the polarization effects at the interface. Alkali doping experiments showed, that up to four Cs atoms coordinate to one COR molecule, occupying the LUMO and LUMO+1. In summary COR and Me_5COR show potential for possible electronic applications, especially regarding the unusual high work function change, together with the charge redistribution at the metal-organic interface.

- The fivefold symmetry of corannulenes was shown to be only influencing the self-assembly behavior, if the C_5 symmetry can not be reduced on the substrate. It was shown, that Me_5COR adapts packing motifs known from hard pentagon tilings due to the inability to tilt. The similarity to a pentagon of the molecular shape on the substrate seems to be of importance, too. This shape is strongly influenced by the size and shape of the substituents.

- The enantiotropic phase transition of COR can be influenced by elimination of free space around the dense phases. This constriction leads to a kinetic barrier, that stabilizes a phase beyond its stable temperature region. Chiral doping of the room temperature phase was shown to frustrate mirror domain formation in the next phase during phase transition.

Chapter 8

Outlook

Although some answers to the questions for this thesis have been provided, there are still open questions.

Regarding the fivefold packing problem, a question that has not been addressed in detail is the influence of the substrate. The substrate might play an important role regarding the adsorption site it provides. COR and Me_5COR on Au(111) and Ag(111) might give insight into the importance of this factor.

The influence of the size of substituents on the COR rim has been demonstrated on a small scale. Investigations on pentaphenyl- (Ph_5COR), pentaethinylphenyl- ($(Ph\text{-}C{\equiv}C)_5COR$) and even pentacora-corannulene (COR_5COR) might reveal answers on the self-assembly behavior of molecules that feature rather big substituents that probably also allow distinction of the two enantiomers on the surface by STM. Some of these molecules are under investigation right now in a follow-up project to this thesis.

The results found on the charge transfer complex formation of corannulene with Cs are still very crude apart from the UPS data. Inverse Photoelectron Spectroscopy can be the right tool to probe the unoccupied states of a molecule and follow the LUMO filling during the doping procedure. Apart from more measurements probing the LUMO there is dire need for theoretical calculations on the charge transfer. Especially the amount of Cs atoms that coordinate to one corannulene molecule needs confirmation, both from a theoretic point of view and with additional measurements. Since the doping effect was similar, not to say even more pronounced for Me_5COR additional investigations on this molecule should be considered as well.

Experiments on the high temperature (4x4) phase of Me_5COR on Cu(111) with infrared spectroscopy should provide information on the state of the molecule, regarding the binding to the copper and the possible absence of the methyl groups.

Bibliography

[1] H. Shirakawa, E. J. Louis, A. G. MacDiarmid, C. K. Chiang, and A. J. Heeger. Synthesis of electrically conducting organic polymers: halogen derivatives of polyacetylene, $(CH)_x$. *J. Chem. Soc., Chem. Commun.*, 16:578–580, 1977.

[2] J. R. Heath. Molecular electronics. *Annual Review of Materials Research*, 39(1):1–23, 2009.

[3] W. R. Salaneck, R. H. Friend, and J. L. Brédas. Electronic structure of conjugated polymers: consequences of electron-lattice coupling. *Physics Reports*, 319(6):231 – 251, 1999.

[4] J. H. Burroughes, D. D. C. Bradley, A. R. Brown, R. N. Marks, K. Mackay, R. H. Friend, P. L. Burns, and A. B. Holmes. Light-emitting diodes based on conjugated polymers. *Nature*, 347(6293):539–541, October 1990.

[5] M. Berggren, O. Inganas, G. Gustafsson, J. Rasmusson, M. R. Andersson, T. Hjertberg, and O. Wennerstrom. Light-emitting diodes with variable colours from polymer blends. *Nature*, 372(6505):444–446, December 1994.

[6] J. Thompson, R. I. R. Blyth, M. Mazzeo, M. Anni, G. Gigli, and R. Cingolani. White light emission from blends of blue-emitting organic molecules: A general route to the white organic light-emitting diode? *Applied Physics Letters*, 79(5):560–562, 2001.

[7] J. Shinar. *Organic Light-Emitting Devices*. Springer, 2004.

[8] M. Muccini. A bright future for organic field-effect transistors. *Nature Materials*, 5(8):605–613, 2006.

[9] H. Hoppe and N. Sariciftci. Polymer solar cells. In S. Marder and K.-S. Lee, editors, *Photoresponsive Polymers II*, volume 214 of *Advances in Polymer Science*, pages 1–86. Springer Berlin / Heidelberg, 2008.

[10] A. P. Cracknell. Tables of the irreducible representations of the 17 two-dimensional space groups and their relevance to quantum mechanical eigenstates for surfaces and thin films. *Thin Solid Films*, 21(1):107 – 127, 1974.

[11] W. E. Barth. Dibenzo[ghi,mno]fluoranthene. *J. Am. Chem. Soc.*, 88(2):380, 1966.

[12] G. J. Gleicher. Calculations on the corannulene system. *Tetrahedron*, 23(11):4257 – 4263, 1967.

[13] J. C. Hanson and C. E. Nordman. The crystal and molecular structure of corannulene, $C_{20}H_{10}$. *Acta Crystallographica Section B*, 32(4):1147–1153, Apr 1976.

[14] J. D. Roberts, A. Streitwieser, and C. M. Regan. Small-Ring Compounds. X. Molecular Orbital Calculations of Properties of Some Small-Ring Hydrocarbons and Free Radicals. *J. Am. Chem. Soc.*, 74(18):4579–4582, 1952.

[15] A. Hirsch, Z. Chen, and H. Jiao. Spherical aromaticity in I_{h} symmetrical fullerenes: The $2(n+1)^2$ rule. *Angew. Chem. Int. Ed.*, 39(21):3915–3917, 2000.

[16] H. W. Kroto, J. R. Heath, S. C. O'Brien, R. F. Curl, and R. E. Smalley. C_{60}: Buckminsterfullerene. *Nature*, 318(6042):162–163, November 1985.

[17] K. Motai, T. Hashizume, H. Shinohara, Y. Saito, H. W. Pickering, Y. Nishina, and T. Sakurai. C_{60} grown on the Cu(111) 1x1 surface. *Japanese Journal of Applied Physics*, 32(Part 2, No. 3B):L450–L453, 1993.

[18] T. Hashizume, K. Motai, X. D. Wang, H. Shinohara, Y. Saito, Y. Maruyama, K. Ohno, Y. Kawazoe, Y. Nishina, H. W. Pickering, Y. Kuk, and T. Sakurai. Intramolecular structures of C_{60} molecules adsorbed on the Cu(111)-(1x1) surface. *Phys. Rev. Lett.*, 71(18):2959–2962, Nov 1993.

[19] J. A. Larsson, S. D. Elliott, J. C. Greer, J. Repp, G. Meyer, and R. Allenspach. Orientation of individual C_{60} molecules adsorbed on Cu(111): Low-temperature scanning tunneling microscopy and density functional calculations. *Phys. Rev. B*, 77(11):115434, Mar 2008.

[20] M. Xi, M. X. Yang, S. K. Jo, B. E. Bent, and P. Stevens. Benzene adsorption on Cu(111): Formation of a stable bilayer. *The Journal of Chemical Physics*, 101(10):9122–9131, 1994.

[21] K.-D. Tsuei, J.-Y. Yuh, C.-T. Tzeng, R.-Y. Chu, S.-C. Chung, and K.-L. Tsang. Photoemission and photoabsorption study of C_{60} adsorption on Cu(111) surfaces. *Phys. Rev. B*, 56(23):15412–15420, Dec 1997.

[22] A. Tamai, A. P. Seitsonen, F. Baumberger, M. Hengsberger, Z.-X. Shen, T. Greber, and J. Osterwalder. Electronic structure at the C_{60}/metal interface: An angle-resolved photoemission and first-principles study. *Phys. Rev. B*, 77(7):075134, Feb 2008.

[23] W. W. Pai, H. T. Jeng, C.-M. Cheng, C.-H. Lin, X. Xiao, A. Zhao, Xieqiu Zhang, Geng Xu, X. Q. Shi, M. A. Van Hove, C.-S. Hsue, and K.-D. Tsuei. Optimal electron doping of a C_{60} monolayer on Cu(111) via interface reconstruction. *Phys. Rev. Lett.*, 104(3):036103, Jan 2010.

[24] J. Schiessling, A. Grigoriev, M. Stener, L. Kjeldgaard, T. Balasubramanian, P. Decleva, R. Ahuja, J. Nordgren, and P. A. Brühwiler. The role of charge-charge correlations and covalent bonding in the electronic structure of adsorbed C_{60}: C_{60}/Al. in print (DOI:10.1021/jp104090d).

[25] R. C. Haddon, A. F. Hebard, M. J. Rosseinsky, D. W. Murphy, S. J. Duclos, K. B. Lyons, B. Miller, J. M. Rosamilia, R. M. Fleming, A. R. Kortan, S. H. Glarum, A. V. Makhija, A. J. Muller, R. H. Eick, S. M. Zahurak, R. Tycko, G. Dabbagh, and F. A. Thiel. Conducting films of C_{60} and C_{70} by alkali-metal doping. *Nature*, 350:320–322, 1991.

[26] R. C. Haddon. Electronic structure, conductivity and superconductivity of alkali metal doped C_{60}. *Acc. Chem. Res.*, 25(3):127133, Aug 1992.

[27] R. C. Dunbar. Binding of transition-metal ions to curved π surfaces: Corannulene and coronene. *The Journal of Physical Chemistry A*, 106(42):9809–9819, 2002.

[28] A. F. Hebard, M. J. Rosseinsky, R. C. Haddon, D. W. Murphy, S. H. Glarum, T. T. M. Palstra, A. P. Ramirez, and A. R. Kortanand. Superconductivity at 18 K in potassium-doped C_{60}. *Nature*, 350:600–601, 1991.

[29] K. Tanigaki, T. W. Ebbesen, S. Saito, J. Mizuki, J. S. Tsai, Y. Kubo, and S. Kuroshima. Superconductivity at 33 K in CsxRbyC_{60}. *Nature*, 352(6332):222–223, July 1991.

[30] M. M. Hashemi D. T. Meyer H. B. Warren L. T. Scott. Corannulene - a convenient new synthesis. *J. Am. Chem. Soc.*, 113:7082–7084, 1991.

[31] L. T. Scott, M. M. Hashemi, and M. S. Bratcher. Corannulene bowl-to-bowl inversion is rapid at room temperature. *J. Am. Chem. Soc.*, 114:1920–1921, 1992.

[32] L. T. Scott, H. E. Bronstein, D. V. Preda, R. B. M. Ansems, M. S. Bratcher, and S. Hagen. Geodesic polyarenes with exposed concave surfaces. *Pure & Appl. Chem.*, 71(2):209–219, 1999.

[33] A. Sygula and P. W. Rabideau. Non-pyrolytic syntheses of buckybowls: Corannulene, cyclopentacorannulene, and a semibuckminsterfullerene. *J. Am. Chem. Soc.*, 34(121):7800–7803, 1999. DOI: 10.1021/ja991169j.

[34] A. Sygula and P. W. Rabideau. A practical and large scale synthesis of the corannulene system. *J. Am. Chem. Soc.*, 122(26):6323–6324, 2000. DOI: 10.1021/ja0011461.

[35] A. Butterfield. Manuscript in preparation. 2011.

[36] T. J. Seiders, E. L. Elliott, G. H. Grube, , and J. S. Siegel. Synthesis of corannulene and alkyl derivatives of corannulene. *J. Am. Chem. Soc.*, 121:7804–7813, 1999.

[37] Y. T. Wu and J. S. Siegel. Aromatic molecular-bowl hydrocarbons: Synthetic derivatives and their structures and and physical properties. *Chemical Review*, 106:4843–4867, 2006.

[38] R. Lück. Dürer-Kepler-Penrose, the development of pentagon tilings. *Materials Science and Engineering A*, 294-296:263 – 267, 2000.

[39] I. Hargittai. *Fivefold Symmetry.* World Scientific, Singapore, 1992.

[40] A. J. Matzger K. E. Plass, A. L. Grzesiak. Molecular packing and symmetry of two-dimensional crystals. *Accounts of Chemical Research*, 40(4):287–293, 2007.

[41] J. V. Barth. Molecular architectonic on metal surfaces. *Annual Review of Physical Chemistry*, 58(1):375–407, 2007.

[42] S. Sachdev and D. R. Nelson. Statistical mechanics of pentagonal and icosahedral order in dense liquids. *Phys. Rev. B*, 32(3):1480–1502, Aug 1985.

[43] J. P. Troadec Y. L. Duparcmeur, A. Gervois. Crystallization of pentagon packings. *Journal of Physics: Condensed Matter*, 7(18):3421, 1995.

[44] T. Schilling, S. Pronk, B. Mulder, and D. Frenkel. Monte carlo study of hard pentagons. *Phys. Rev. E*, 71(3):036138, Mar 2005.

[45] T. J. Seiders, K. Baldridge, G. H. Grub, and J. S. Siegel. Structure/energy correlation of bowl depth and inversion barrier in corannulene derivatives: Combined experimental and quantum mechanical analysis. *J. Am. Chem. Soc.*, 123(4):517–525, 2001.

[46] M. Parschau, R. Fasel, K.-H. Ernst, O. Gröning, L. Brandenberger, R. Schillinger, T. Greber, A. Seitsonen, Y.-T. Wu, and J. Siegel. Buckybowls on metal surfaces: Symmetry mismatch and enantiomorphism of corannulene on Cu(110). *Angew. Chem. Int. Ed.*, 46(43):8258–8261, 2007.

[47] W. Xiao, D. Passerone, P. Ruffieux, K. At-Mansour, O. Gröning, E. Tosatti, J. S. Siegel, and R. Fasel. C_{60}/Corannulene on Cu(110): A Surface-Supported Bistable Buckybowl-Buckyball Host-Guest System. *J. Am. Chem. Soc.*, 130(14):4767–4771, 2008.

[48] H. Becker, G. Javahery, S. Petrie, P. C. Cheng, H. Schwarz, L. T. Scott, and D. K. Bohme. Gas-phase ion/molecule reactions of corannulene, a fullerene subunit. *J. Am. Chem. Soc.*, 115(24):11636–11637, 1993.

[49] A. Sygula, F. R. Fronczek, R. Sygula, P. W. Rabideau, and M. M. Olmstead. A double concave hydrocarbon buckycatcher. *J. Am. Chem. Soc.*, 129:3842, 2007. doi: 10.1021/ja070616p.

[50] L. Merz, M. Parschau, L. Zoppi, K. Baldridge, J. S. Siegel, and K.-H. Ernst. Reversible phase transitions in a buckybowl monolayer. *Angew. Chem. Int. Ed.*, 48(11):1966–1969, 2009.

[51] L. Zoppi, A. Garcia, and K. Baldridge. Theoretical investigation of the binding process of corannulene on a Cu(111) surface. *The Journal of Physical Chemistry A*, 114(33):8864–8872, 2010.

[52] L. Merz, M. Parschau, J. S. Siegel, and K.-H. Ernst. Condensation of fivefold-symmetric molecules in two dimensions. *Chimia International Journal for Chemistry*, 63:214–216(3), 2009.

[53] M. A. Petrukhina, Y. Sevryugina, A. Y. Rogachev, E. A. Jackson, and L. T. Scott. Corannulene hub carbon coordination by $[Ru_2\{O_2C(3,5-CF_3)_2C_6H_3\}_2(CO)_5]$. *Angew. Chem. Int. Ed.*, 45(43):7208–7210, 2006.

[54] A. Y. Rogachev, Y. Sevryugina, A. S. Filatov, and M. A. Petrukhina. Corannulene vs. C_{60}-fullerene in metal binding reactions: A direct DFT and x-ray structural comparison. *Dalton Trans.*, 35:3871–3873, 2007.

[55] J. S. Siegel, K. Baldridge, A. Linden, and R. Dorta. d^8 Rhodium and Iridium Complexes of Corannulene. *J. Am. Chem. Soc.*, 128(33):10644–10645, 2006.

[56] M. A. Petrukhina and L. T. Scott. Coordination chemistry of buckybowls: from corannulene to a hemifullerene. *Dalton Trans.*, 18:2969–2975, 2005.

[57] B. D. Steinberg, E. A. Jackson, A. S. Filatov, A. Wakamiya, M. A. Petrukhina, and L. T. Scott. Aromatic p-systems more curved than C_{60}. The complete family of all indenocorannulenes synthesized by iterative microwave-assisted intramolecular arylations. *J. Am. Chem. Soc.*, 131(30):10537–10545, 2009.

[58] Z. Ge, J. C. Duchamp, T. Cai, H. W. Gibson, and H. C. Dorn. Purification of endohedral trimetallic nitride fullerenes in a single, facile step. *Journal of the American Chemical Society*, 127(46):16292–16298, 2005.

[59] M. Saunders, H. A. Jimenez-Vazquez, R. J. Cross, S. Mroczkowski, M. L. Gross, D. E. Giblin, and R. J. Poreda. Incorporation of helium, neon, argon, krypton, and xenon into fullerenes using high pressure. *Journal of the American Chemical Society*, 116(5):2193–2194, 1994.

[60] P. Thaddeus. The prebiotic molecules observed in the interstellar gas. *Philosophical Transactions of the Royal Society B: Biological Sciences*, 361(1474):1681–1687, 2006.

[61] F. J. Lovas, R. J. McMahon, J.-U. Grabow, M. Schnell, J. Mack, L. T. Scott, and R. L. Kuczkowski. Interstellar Chemistry: A Strategy for Detecting Polycyclic Aromatic Hydrocarbons in Space. *J. Am. Chem. Soc.*, 127(12):4345–4349, 2005. PMID: 15783216.

[62] G. Rouillé, C. Jäger, M. Steglich, F. Huisken, T. Henning, G. Theumer, I. Bauer, and H.-J. Knölker. IR, Raman, and UV/Vis spectra of corannulene for use in possible interstellar identification. *Chem. Phys. Chem.*, 9(14):2085–2091, 2008.

[63] J. Mack, P. Vogel, D. Jones, N. Kaval, and A. Sutton. The development of corannulene-based blue emitters. *Org. Biomol. Chem.*, 5(15):2448–2452, 2007.

[64] M. Briggs and M. P. Seah, editors. *Practical Surface Analysis - Auger and X-ray photoelectron spectroscopy.* John Wiley & Sons and Inc., 1990 (2nd. edition).

[65] C. D . Wagner, W. M. Riggs, L. E. Davis, , and J. F. Moulder. *Handbook of X-ray Photoelectron Spectroscopy 1st ed.* Perkin-Elmer Corporation (Physical Electronics), 1979 (1st edition).

[66] J. F. Moulder, W. F. Stickle, P. E. Sobol, and K. Bomben. *Handbook of X-ray Photoelectron Spectroscopy 2nd ed.* Perkin-Elmer Corporation (Physical Electronics), 1992 (2nd edition).

[67] J. Stöhr. *NEXAFS Spectroscopy.* Springer-Verlag, Berlin, 1992.

[68] D. Koningsberger. *X-Ray Absorption.* Wiley, New York, 1988.

[69] J. Pendry. *Low Energy Electron Diffraction.* Acacemic Press, London, 1974.

[70] M. E. Van Hove. *Low-Energy Electron Diffraction.* Springer, Berlin, 1986.

[71] K. Oura. *Surface Science.* Springer, Berlin, 2003.

[72] G. Binnig, H. Rohrer, C. Gerber, and E. Weibel. Tunneling through a controllable vacuum gap. *Applied Physics Letters*, 40(2):178–180, 1982. DOI: 10.1063/1.92999.

[73] G. Binnig, H. Rohrer, C. Gerber, and E. Weibel. Surface studies by scanning tunneling microscopy. *Phys. Rev. Lett.*, 49(1):57–61, Jul 1982.

[74] G. Binnig, H. Rohrer, C. Gerber, and E. Weibel. 7x7 reconstruction on Si(111) resolved in real space. *Phys. Rev. Lett.*, 50(2):120–123, Jan 1983.

[75] G. Binnig and H. Rohrer. Scanning tunneling microscopy—from birth to adolescence. *Rev. Mod. Phys.*, 59(3):615–625, Jul 1987.

[76] J. A. Kubby and J. J. Boland. Scanning tunneling microscopy of semiconductor surfaces. *Surface Science Reports*, 26(3-6):61 – 204, 1996.

[77] C. Chen. *Introduction to Scanning Tunneling Microscopy.* Oxford University Press, Oxford Oxfordshire, 2008.

[78] R. Wiesendanger. *Scanning Probe Microscopy and Spectroscopy.* Cambridge University Press, Cambridge, 1994.

[79] I. Horcas, R. Fernández, J. M. Gómez-Rodríguez, J. Colchero, J. Gómez-Herrero, and A. M. Baro. WSxM: A software for scanning probe microscopy and a tool for nanotechnology. *Review of Scientific Instruments*, 78(1):013705, 2007.

[80] T. Hahn. *International Tables for Crystallography Vol. A*. Kluwer Academic Publishers, Boston, 2002.

[81] A. I. Kitaigorodskii. The principle of close packing and the condition of thermodynamic stability of organic crystals. *Acta Crystallographica*, 18(4):585–590, Apr 1965.

[82] T. Bauert, L. Merz, D. Bandera, M. Parschau, J. S. Siegel, and K.-H. Ernst. Building 2d crystals from 5-fold-symmetric molecules. *J. Am. Chem. Soc.*, 131(10):3460–3461, 2009.

[83] O. Guillermet, E. Niemi, S. Nagarajan, X. Bouju, D. Martrou, A. Gourdon, and S. Gauthier. Self-assembly of fivefold-symmetric molecules on a threefold-symmetric surface. *Angew. Chem. Int. Ed.*, 48(11):1970–1973, 2009.

[84] T. Sakurai, X. D. Wang, T. Hashizume, V. Yurov, H. Shinohara, and H. W. Pickering. Adsorption of fullerenes on Cu(111) and Ag(111) surfaces. *Applied Surface Science*, 87-88:405 – 413, 1995. Proceedings of the 41st International Field Emission Symposium.

[85] G. Otero, G. Biddau, C. Sanchez-Sanchez, R. Caillard, M. F. Lopez, C. Rogero, F. J. Palomares, N. Cabello, M. A. Basanta, J. Ortega, J. Mendez, A. M. Echavarren, R. Perez, B. Gomez-Lor, and J. A. Martin-Gago. Fullerenes from aromatic precursors by surface-catalysed cyclodehydrogenation. *Nature*, 454(7206):865–868, 2008.

[86] L. Merz, T. Bauert, M. Parschau, G. Koller, J. S. Siegel, and K.-H. Ernst. Polymorph selection in 2D crystals by phase transition blocking. *Chemical Communications*, 39:5871–5873, 2009.

[87] J. Bernstein. *Polymorphism in Molecular Crystals*. Oxford University Press, Oxford Oxfordshire, 2002.

[88] B. D. Hamilton, M. A. Hillmyer, and M. D. Ward. Glycine polymorphism in nanoscale crystallization chambers. *Crystal Growth and Design*, 8(9):3368–3375, 2008.

[89] M. O. Lorenzo, S. Haq, T. Bertrams, P. Murray, R. Raval, and C. J. Baddeley. Creating chiral surfaces for enantioselective heterogeneous catalysis: R,R-tartaric acid on Cu(110). *The Journal of Physical Chemistry B*, 103(48):10661–10669, 1999.

[90] M. O. Lorenzo, C. J. Baddeley, C. Muryn, and R. Raval. Extended surface chirality from supramolecular assemblies of adsorbed chiral molecules. *Nature*, 404(6776):376–379, March 2000.

[91] V. Humblot, M. O. Lorenzo, C. J. Baddeley, S. Haq, and R. Raval. Local and global chirality at surfaces: Succinic acid versus tartaric acid on Cu(110). *Journal of the American Chemical Society*, 126(20):6460–6469, 2004. PMID: 15149243.

[92] C. G. M. Hermse, A. P. van Bavel, A. P. J. Jansen, L. A. M. M. Barbosa, P. Sautet, and R. A. van Santen. Formation of chiral domains for tartaric acid on Cu(110): A combined DFT and kinetic monte carlo study. *The Journal of Physical Chemistry B*, 108(30):11035–11043, 2004.

[93] M. Parschau, B. Behzadi, S. Romer, and K.-H. Ernst. Stereoisomeric influence on 2D lattice structure: achiral meso-tartaric acid versus chiral tartaric acid. *Surface and Interface Analysis*, 38(12-13):1607–1610, 2006.

[94] B. Behzadi-Arab. *Fundamental aspects of chirally modified metal surface.* PhD thesis, Eidgenössische Technische Hochschule ETH, Zürich, Switzerland, 2006.

[95] C. J. Baddeley. Fundamental investigations of enantioselective heterogeneous catalysis: Reflections on heterogeneous asymmetric catalysis. *Topics in Catalysis*, 25:17–28, 2003.

[96] M. Studer, H.-U. Blaser, and C. Exner. Enantioselective hydrogenation using heterogeneous modified catalysts: An update. *Advanced Synthesis & Catalysis*, 345(1-2):45–65, 2003.

[97] S. M. Barlow and R. Raval. Complex organic molecules at metal surfaces: bonding, organisation and chirality. *Surface Science Reports*, 50(6-8):201 – 341, 2003.

[98] H.-J. Yan, D. Wang, M.-J. Han, L.-J. Wan, and C.-L. Bai. Adsorption and coordination of tartaric acid enantiomers on Cu(111) in aqueous solution. *Langmuir*, 20(18):7360–7364, 2004.

[99] N. M. Santagata, A. M. Lakhani, D. J. DeWitt, P. Luo, and T. P. Pearl. Probing molecular-level organizational structure and electronic decoupling of tartaric acid domains supported on Ag(111). *Journal of Physics: Conference Series*, 100(5):052066, 2008.

[100] N. M. Santagata, A. M. Lakhani, B. F. Davis, P. Luo, M. Buongiorno Nardelli, and T. P. Pearl. Chiral steering of molecular organization in the limit of weak adsorbate-substrate interactions: Enantiopure and racemic tartaric acid domains on Ag(111). *The Journal of Physical Chemistry C*, 114(19):8917–8925, 2010.

[101] G. Chen, R. G. Cooks, E. Corpuz, and L. T. Scott. Estimation of the electron affinities of C_{60}, corannulene, and coronene by using the kinetic method. *Journal of the American Society for Mass Spectrometry*, 7(7):619 – 627, 1996.

[102] J. Topping. On the Mutual Potential Energy of a Plane Network of Doublets. *Proceedings of the Royal Society of London. Series A*, 114(766):67–72, 1927.

[103] M. Pivetta, F. Patthey, W.-D. Schneider, and B. Delley. Surface distribution of cu adatoms deduced from work function measurements. *Phys. Rev. B*, 65(4):045417, Jan 2002.

[104] H. Fukagawa, H. Yamane, S. Kera, K. K. Okudaira, and N. Ueno. Experimental estimation of the electric dipole moment and polarizability of titanyl phthalocyanine using ultraviolet photoelectron spectroscopy. *Phys. Rev. B*, 73(4):041302, Jan 2006.

[105] D. Lide. *CRC Handbook of Chemistry and Physics*. CRC Press, Boca Raton, 2001.

[106] A. Kiejna. *Metal Surface Electron Physics*. Pergamon, Amsterdam, 1996.

[107] A. Ayalon, M. Rabinovitz, P.-C. Cheng, and L. T. Scott. Corannulene tetraanion: A novel species with concentric anionic rings. *Angew. Chem. Int. Ed.*, 31(12):1636–1637, 1992.

[108] A. Ayalon, A. Sygula, P.-C. Cheng, M. Rabinovitz, P. W. Rabideau, and L. T. Scott. Stable high-order molecular sandwiches: Hydrocarbon polyanion pairs with multiple lithium ions inside and out. *Science*, 265(5175):1065–1067, 1994.

[109] A. Weitz, E. Shabtai, M. Rabinovitz, M. S. Bratcher, C. C. McComas, M. D. Best, and L. T. Scott. Dianions and tetraanions of bowl-shaped fullerene fragments dibenzo[a,g]corannulene and dibenzo[a,g]cyclopenta[kl]corannulene. *Chemistry - A European Journal*, 4(2):234–239, 1998.

[110] I. Aprahamian, D. V. Preda, M. Bancu, A. P. Belanger, T. Sheradsky, L. T. Scott, and M. Rabinovitz. Reduction of bowl-shaped hydrocarbons: Dianions and tetraanions of annelated corannulenes. *J. Org. Chem.*, 71(1):290–298, 2006.

[111] M. Baumgarten, L. Gherghel, M. Wagner, A. Weitz, M. Rabinovitz, P.-C. Cheng, and L. T. Scott. Corannulene reduction: Spectroscopic detection of all anionic oxidation states. *J. Am. Chem. Soc.*, 117(23):6254–6257, 1995.

[112] L. Merz and K.-H. Ernst. Unification of the matrix notation in molecular surface science. *Surface Science*, 604(11-12):1049 – 1054, 2010.

[113] K.-D. Tsuei and P. D. Johnson. Charge transfer and a new image state of C_{60} on Cu(111) surface studied by inverse photoemission. *Solid State Communications*, 101(5):337 – 341, 1997.

[114] J. V. Barth, H. Brune, G. Ertl, and R. J. Behm. Scanning tunneling microscopy observations on the reconstructed Au(111) surface: Atomic structure, long-range superstructure, rotational domains, and surface defects. *Phys. Rev. B*, 42(15):9307–9318, Nov 1990.

[115] D. D. Chambliss, R. J. Wilson, and S. Chiang. Nucleation of ordered Ni island arrays on Au(111) by surface-lattice dislocations. *Phys. Rev. Lett.*, 66(13):1721–1724, Apr 1991.

[116] M. Böhringer, K. Morgenstern, W.-D. Schneider, and R. Berndt. Separation of a racemic mixture of Two-Dimensional molecular clusters by scanning tunneling microscopy. *Angewandte Chemie International Edition*, 38(6):821–823, 1999.

[117] S. Clair, S. Pons, H. Brune, K. Kern, and J. V. Barth. Mesoscopic metallosupramolecular texturing by hierarchic assembly. *Angew. Chem. Int. Ed.*, 44(44):7294–7297, 2005.

Appendix

Acronyms

ARPES	Angle Resolved Photoelectron Spectroscopy
ARUPS	Angle Resolved Ultraviolet Photoelectron Spectroscopy
COR	Corannulene
C_5	fivefold rotational symmetry
C_{5v}	fivefold rotational and mirror symmetry
Cl_5COR	Pentachloro-Corannulene
DDQ	2,3-Dichloro-5,6-dicyano-1,4-benzoquinone
DME	Dimethoxyethane
ESCA	Electron Spectroscopy for Chemical Analysis
EXAFS	Extended X-Ray Absorption Fine Structure
FVP	Flash Vacuum Pyrolysis
FWHM	Full-Width at Half-Maximum
HOMO	Highest Occupied Molecular Orbital
IPS	Inverse Photoelectron Spectroscopy
LEED	Low-Energy Electron Diffraction
LNT	Liquid Nitrogen Temperature
LUMO	Lowest Unoccupied Molecular Orbital
Me_5COR	Pentamethyl-Corannulene
ML	monolayer(s)
NBS	N-Bromosuccinimide
NEXAFS	Near Edge X-Ray Absorption Fine Structure
PES	Photoelectron Spectroscopy
Ph_5COR	Pentaphenyl-Corannulene
RT	room temperature
STM	Scanning Tunneling Microscope / Microscopy
TA	Tartaric Acid
THF	Tetrahydrofuran
TPD	Temperature Programmed Desorption
UHV	Ultra-High Vacuum
UPS	Ultraviolet Photoelectron Spectroscopy
X_5COR	Pentasubstituated Corannulene
XPS	X-Ray Photoelectron Spectroscopy

Matrix Notation of Molecular Monolayers

To describe the self-assembled structure of an adlayer on a crystal substrate, transformation matrices are used. Unfortunately there are different sets of rules used in different groups that allow ambiguous results. A unification of the matrix notation was proposed by Merz et al., introducing a conclusive set of rules applicable in all cases and a master matrix that identifies an adlayer structure beyond doubt, unifying mirror and rotational sub-domains [112]. All adlayer matrices in this thesis follow these rules.

Rules for defining substrate vectors $\vec{a}_s$ and $\vec{b}_s$

1. The most densely packed substrate direction is oriented parallel to the northsouth direction and $\vec{a}_s$ follows it, pointing towards south.
2. Vector $\vec{b}_s$ points to the right (with vector c pointing away from the crystal bulk), so that they form a right-handed system.
3. The angle γ_s between $\vec{a}_s$ and $\vec{b}_s$ must be $\geq 90^\circ$, but smallest possible.
4. For stepped surfaces, the wider terrace is oriented to the right.

Rules for defining overlayer matrices and vectors $\vec{a}$ and $\vec{b}$

1. The system is right-handed ($\vec{a}$ to $\vec{b}$ goes counterclockwise).
2. $|\vec{a}| \leq |\vec{b}|$
3. The angle γ between $\vec{a}$ and $\vec{b}$ must be $\geq 90^\circ$, but smallest possible.
4. $\vec{a}$ points southward and $\vec{b}$ points to the right.
5. If $\gamma = 90^\circ$, then $\vec{a}$ can point horizontally to the right.

Molecular Orbital Calculations on COR

orbital	symmetry	orbital eigenvalue [eV]
LUMO+1	E1	+1.51
LUMO	E1	+1.51
HOMO	E2	-8.05
HOMO-1	E2	-8.05
HOMO-2	E1	-8.07
HOMO-3	E1	-8.07
HOMO-4	E2	-11.08
HOMO-5	E2	-11.08
HOMO-6	A1	-11.18
HOMO-7	E2	-12.85
HOMO-8	E2	-12.85
HOMO-9	E1	-13.09
HOMO-10	E1	-13.09
HOMO-11	E1	-13.81
HOMO-12	E1	-13.81
HOMO-13	A1	-14.59
HOMO-14	E2	-15.23
HOMO-15	E2	-15.23

Table 1 Orbital eigenvalues of COR calculated on the B3LYP optimized structure using single energy point calculation on the MP2 level of theory. Courtesy of L. Zoppi / K. Baldridge, University of Zurich.

The orbital eigenvalues presented here do not match the presented values in [46], since they are calculated on different levels of theory (PBE0 vs. B3LYP/MM2). The values presented here were calculated on the same basis as the orbital eigenvalues for Me_5COR presented in the following chapter 8.

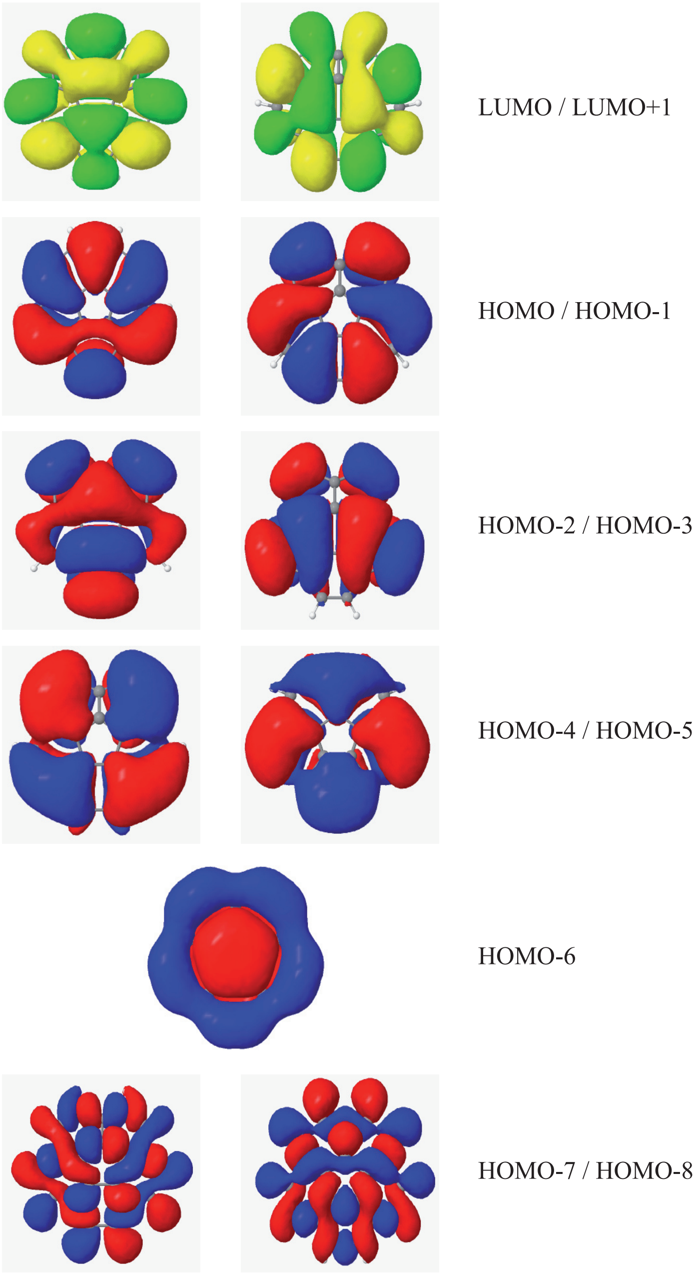

Fig. A.1 COR molecular orbitals corresponding to the eigenvalues in table 1. Courtesy of L. Zoppi / K. Baldridge, University of Zurich.

Molecular Orbital Calculations on Me_5COR

orbital	symmetry	orbital eigenvalue [eV]
LUMO+1	E1	1.72
LUMO	E1	1.72
HOMO	E1	-7.71
HOMO-1	E1	-7.71
HOMO-2	E2	-7.72
HOMO-3	E2	-7.72
HOMO-4	A	-10.58
HOMO-5	E2	-10.60
HOMO-6	E2	-10.60
HOMO-7	E2	-12.46
HOMO-8	E2	-12.46
HOMO-9	E1	-12.62
HOMO-10	E1	-12.62
HOMO-11	E1	-13.22
HOMO-12	E1	-13.22
HOMO-13	A1	-14.08
HOMO-14	E2	-14.17
HOMO-15	E2	-14.17

Table 2 Orbital eigenvalues of Me_5COR calculated on the B3LYP optimized structure using single energy point calculation on the MP2 level of theory. Courtesy of L. Zoppi / K. Baldridge, University of Zurich.

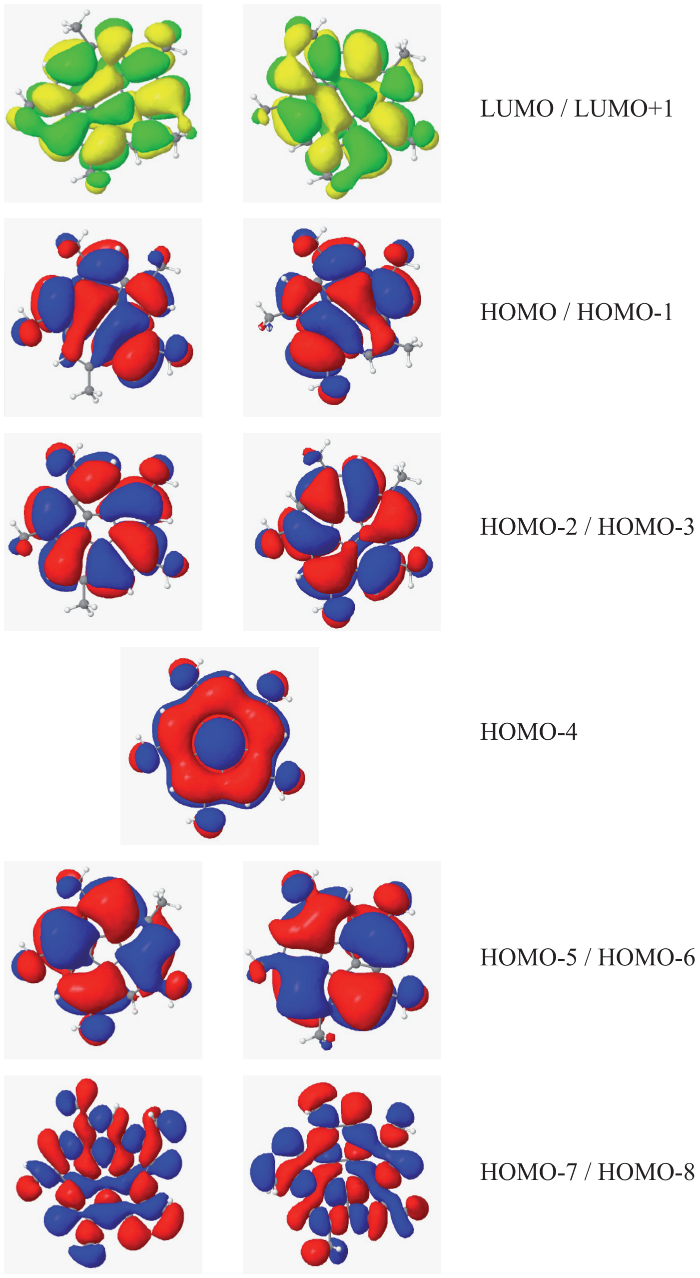

Fig. A.2 Me_5COR molecular orbitals corresponding to the eigenvalues in table 2. Courtesy of L. Zoppi / K. Baldridge, University of Zurich.

Work function changes for C_{60} on different metal substrates

The observation that the work function of a monolayer of C_{60} on metal surfaces is always around 5 eV, independent of the metal, was found to be due to the metallic character of the C_{60} adlayer. The work function measured is basically the property of the metallic C_{60} adlayer [113], only marginally related to the metal substrate underneath.

metal substrate	clean surface WF [eV]	WF of 1 ML C_{60}/metal [eV]	$\Delta\phi$
Cu(111)	4.94	4.86	-0.08
Ni(111)	5.36	4.93	-0.43
Al(110)	4.35	5.25	+0.95
Al(111)	4.25	5.15	+0.95
Au(110)	5.37	4.82	-0.45
Rh(111)	5.4	4.9	-0.5
Ta(110)	4.8	5.4	+0.6

Table 3 Work functions (WF) of clean metal surfaces and after deposition of 1 ML C_{60}, and the absolute change in work function ($\Delta\phi$) [21].

Pentachloro-Corannulene – Cl_5COR

Pentachloro-corannulene was deposited onto a stepped Au(111) substrate, although the herringbone reconstruction [114] of the Au(111) surface is known to influence molecular self-assembly [115–117]. To avoid this influence a stepped gold surface on a Au(11 12 12) crystal was used, where the surface can not form extended reconstructions. From the STM images in Figure A.3 the structure is estimated to be most likely a $\left(\begin{smallmatrix} 8 & 0 \\ 0 & 8 \end{smallmatrix}\right)$ structure with four Cl_5COR per unit cell.

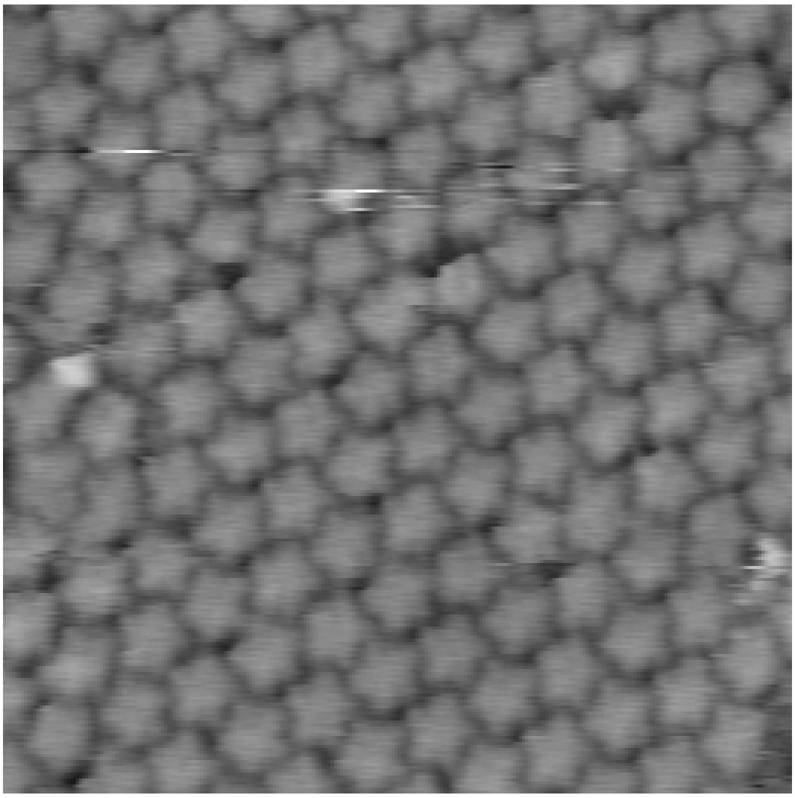

Fig. A.3 13 nm x 13 nm STM image of Cl_5COR on Au(111). Taken at 37 K. Image courtesy of M. Parschau.

The observed structure is analogue to the highest density pentagon packing found in macroscopic pentagon packing experiments and the striped phase of Me_5COR on Cu(111), see chapter 3. The individual azimuthal orientation of the molecules is more precise than for Me_5COR / Cu(111). This might be the case due to a more pentagon like shape of the molecule and / or due to a better fit on the substrate lattice.

LEED pattern of the Helicene- and $\mathrm{Me_5COR}$-stabilized corannulene phase II

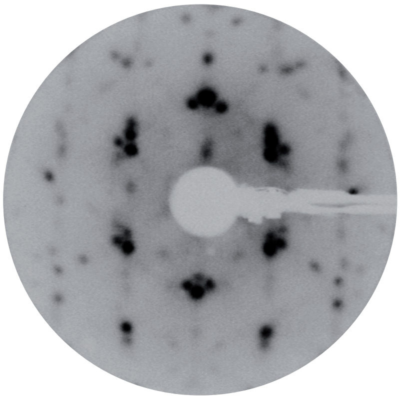

Fig. A.4 LEED pattern of the stabilized $\left(\begin{smallmatrix}4 & 0\\ 3 & 7\end{smallmatrix}\right)$ COR phase, imaged with 15 eV in the supercooled state at 90 K. The phase was stabilized with 0.14 ML of $\mathrm{Me_5COR}$, deposited at 220 K onto the COR phase.

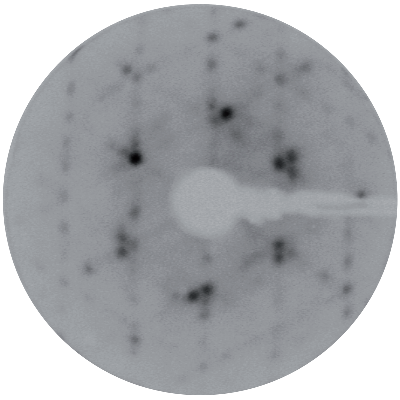

Fig. A.5 LEED pattern of the stabilized $\left(\begin{smallmatrix}4 & 0\\ 3 & 7\end{smallmatrix}\right)$ COR phase, imaged with 15 eV in the supercooled state at 90 K. The phase was stabilized with 0.14 ML of M-Helicene, deposited at 220 K onto the COR phase.

Angle resolved EDC of COR/Cu(111)

Angle resolved energy distribution curves (EDC) can directly give the band structure of a two-dimensional system, because in first approximation, $k_\perp$ plays no role. In the case of COR/Cu(111), however, the bands show no dispersion.

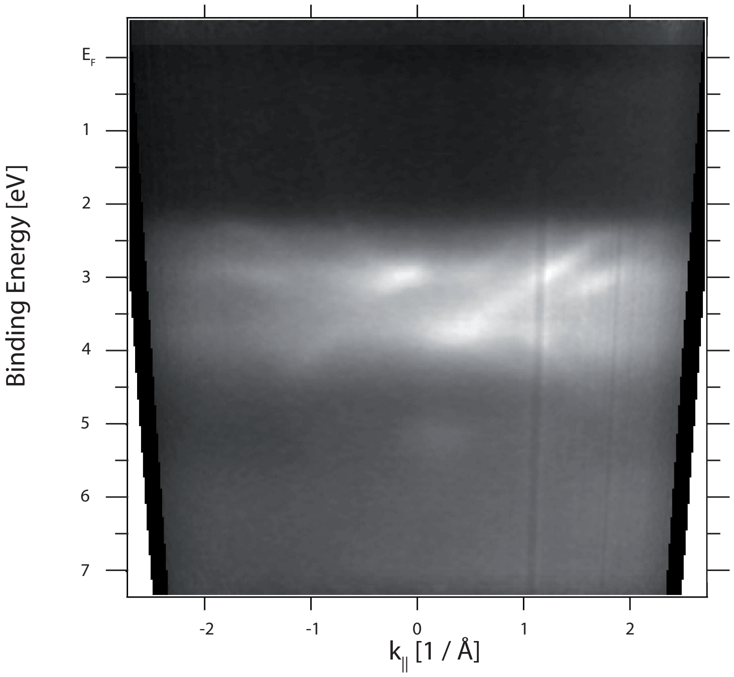

Fig. A.6 Angle resolved EDC of 1 ML COR on Cu(111), 55° off normal incident angle, $h\nu = 35\,\mathrm{eV}$. The COR bands show no dispersion, the structure seen between 2 and 4 eV are due to the Cu d band.

Publications

Directed batch assembly of three-dimensional helical nanobelts through angular winding and electroplating
D. Bell, T. E. Bauert, L. Zhang, L.-X. Dong, Y. Sun, D. Grützmacher, B. J. Nelson
Nanotechnology 18 (2007) 055304.

Multiple Transmission-Reflection Infrared Spectroscopy for High-Sensitivity Measurement of Molecular Monolayers on Silicon Surfaces
H.-B. Liu, N. V. Venkataraman, T. E. Bauert, M. Textor, S.-J. Xiao
J. Phys. Chem. A 112 (2008) 12372.

Building 2D Crystals from 5-Fold-Symmetric Molecules
T. Bauert, L. Merz, D. Bandera, M. Parschau, J. S. Siegel, K.-H. Ernst
J. Am. Chem. Soc. 131 (2009) 3460.

Polymorph selection in 2D crystals by phase transition blocking
L. Merz, T. Bauert, M. Parschau, G. Koller, J. S. Siegel, K.-H. Ernst
Chem. Comm. 39 (2009) 5871.

Electronic Properties and Interfacial Dipole Moments of Corannulenes on Cu(111)
T. Bauert, G. Koller, M. Parschau, J. S. Siegel, K.-H. Ernst
Manuscript in preparation, 2011.

Curriculum Vitae

Last and first name	Bauert Tobias Elmar
Date of birth	March 23, 1980
Citizen of	Wetzikon ZH, Switzerland

Education

1987 – 1993	Primary school in Nürensdorf, ZH
1993 – 1999	Gymnasium at Kantonsschule Rychenberg in Winterthur, ZH
2000 – 2006	Studies of Material Science at the Swiss Federal Institute of Technology Zurich - ETHZ
2004 and 2005	Two Internships on "Natural Fibre Reinforced Polymers" in the group of Dr. R. Greiner at Daimler AG Group Research & Advanced Engineering, Ulm, Germany.
2006	Diploma thesis on *"Multiple Transmission-Reflection FTIR Spectroscopy for the Investigation of Silicon Based Monolayers"* in the groups of Prof. Dr. S.-J. Xiao, Departement of Organic Chemistry, Nanjing University, China and Prof. Dr. M. Textor, Laboratory of Surface Science and Technology, Department of Material Science, Swiss Federal Institute of Technology Zurich.
2006 – 2010	PhD student in the research area of *Molecular Surface Science* in the group of Prof. Dr. K.-H. Ernst, Nanoscale Material Science, Empa - Swiss Federal Laboratories for Materials Science and Technology, Dübendorf.

Acknowledgements

A number of people contributed substantially to the success of this thesis, be it professionally or personally. I want to thank them all for their help.

First and foremost my sincere thanks go to Annina and my family for their support and understanding in times when being a PhD student was not all fun and laughs.

I want to thank my supervisor and doctoral father Karl-Heinz Ernst for giving me the opportunity for this thesis and providing the environment for professional science. I thank Jay Siegel for his unbureaucratic support, when I needed it.
I thank Manfred Parschau for his open ear to any surface science related question and his friendly way of helping with words and deeds whenever he was needed. Christian Roth, Quang Thai, Dominik Jaeger and Pablo Stickar have my thanks for sharing my adventure and having a real good time. I thank Christa Jordi for all the laughs and for taking my mind of work during breaks.
My thanks go also to the Surface Science Group at the Karl-Franzens Universität Graz in Austria, especially Falko Netzer, Georg Koller, Mike Ramsey and Eva Maria Reinisch for fantastic support during my stay for UPS measurements on their equipment. I want to thank particularly Georg Koller for his valuable input on photoemission spectroscopy.
I have to thank also various collaborators at Empa for their swift and uncomplicated collaboration, namely Daniele Passerone, Roland Hany and Cedric Sax for his semester project.
Last but not least I thank all members of Lab 125 at Empa for their support, be it great or small, and for providing a productive environment. I learned a lot from you guys.
Financial support of the Swiss National Science Foundation (SNF) is gratefully acknowledged.

Thank you all.